**Title**
Imaging Individual Chemical Bonds and Tuning Single-Molecule Charge States at Surfaces



**Author**
Wickenburg, Sebastian

**Publication Date**
2014

Peer reviewed|Thesis/dissertation

**Imaging Individual Chemical Bonds and Tuning Single-Molecule Charge States at Surfaces**

by

Sebastian Wickenburg

A dissertation submitted in partial satisfaction of the
requirements for the degree of
Doctor of Philosophy

in

Physics

in the

Graduate Division

of the

University of California, Berkeley

Committee in charge:

Professor Michael F. Crommie, Chair
Professor Steven G. Louie
Professor Rachel A. Segalman

Spring 2014

**Imaging Individual Chemical Bonds and Tuning Single-Molecule Charge States at Surfaces**

## Abstract

Imaging Individual Chemical Bonds
and Tuning Single-Molecule Charge States at Surfaces

by

Sebastian Wickenburg

Doctor of Philosophy in Physics

University of California, Berkeley

Professor Michael F. Crommie, Chair

In an effort to make advances in electronics through ever smaller devices, the field of molecular electronics has emerged as a natural step in achieving ultimate miniaturization of devices down to the size of single molecules. Progress in molecular electronics is intimately linked to understanding these devices at the atomic and molecular length scales at which they operate. As a move in this direction we have performed local probe studies in which we have nondestructively imaged the products of chemical reactions within molecular electronics elements. We have also imaged and tuned the orbitals and charge states of individual molecular electronics elements on surfaces. This dissertation, after introducing the field of nanoelectronics and the local probe techniques used in the study, reports on imaging of chemical structures of on-surface synthesized molecules and conductive polymers with individual-chemical-bond resolution and their relationship to the electronic structure. Depending on the specific molecules and surfaces used, the on-surface synthesized molecular structures formed single molecule products (monomers), chemically reacted intermediates, or conductive polymers exhibiting extended electronic structure along their backbone. This dissertation additionally demonstrates orbital gating of molecules on a back-gated graphene device. The energy alignment of molecular orbitals on graphene was tuned using an electrostatic back-gate, which resulted in molecules switching between neutral and negatively charged states. This control of charge states of single molecules on surfaces and identification of on-surface synthesized reaction products with sub-molecular resolution contributes to our understanding of molecular electronics elements at their natural length scales.

Für meine Eltern, Kathi, und Jing.

# Contents

# List of Figures

# List of Tables

## Acknowledgments

I would like to thank my advisor Prof. Mike Crommie for showing me how to be a scientist. Through a great balance between guidance and allowing me to make my own mistakes, he was able to teach me much about physics, presenting my thoughts, and leading others. Trying to emulate his way of identifying the right questions to ask and communicating the answers will be a lifelong challenge and I feel immensely grateful that he was my advisor.

I would also like to thank Prof. Steven Louie and Prof. Rachel Segalman, who served on my dissertation committee and gave me excellent advice. Thanks also to Prof. Feng Wang who chaired my qualifying exam, which was a surprisingly pleasant experience. Many thanks also to Prof. Felix Fischer and Prof. Angel Rubio who provided invaluable chemical insight.

It is difficult to overstate how important "my postdocs" Alex Riss and Jiong Lu were for my development as a scientist. Alex has a great leadership style and amazing scientific instincts. Without him, all of the work in this dissertation would have been impossible, and I am very grateful for his leadership, optimism and friendship. Jiong's scientific insight and vast knowledge of the field made our work together deeply rewarding. Both of them were a joy to work with and terrific mentors and role models who taught me a lot.

There are many people in the lab who had a positive influence on me and made my time here an amazing experience. Aaron Bradley and I took many walks to get coffee and almost invariably I came back with my thoughts in better order and a fresh set of new ideas in my head. Aaron is also the person without whom this dissertation would not have been submitted, literally. Hsin-Zon Tsai showed me how to get things done. Miguel Moreno Ugeda's incredible knowledge of instrumentation often helped me find my way out of a problem. Ivan Pechenezhskiy has been a great partner for debating about life, the Universe and everything. Victor Brar introduced me to the art of tip fixing as "the most boring computer game in the world". I am very grateful to Dimas de Oteyza and Yen-Chia Chen for letting me look at their molecules. Many thanks to Elaine Quiter for making everything so much easier. In addition, there are many more wonderful current and former members of the Crommie group to thank: Danny Haberer, Jairo Velasco Jr., Arash Omrani, Yuanbo Zhang, Sarah Burke, Régis Decker, Daniel Wegner, Melissa Panlasigui, Han Sae Jung, Ryan Johnson, Dillon Wong, Kacey Meaker, Hannes Böckmann, Chad Germany, Xiaowei Zhang, Yang Wang, Giang Nguyen, Chen Chen, Zahra Pedramrazi, Drew Edelberg, Brandon Giles, Trinity Joshi, Juwon Lee, Youngkyou Kim, Salman Kahn, Mandy Huo and Wei Ruan. All of them made this a truly rewarding experience.

My work here has been shaped by our collaboration with theorists. The Louie group has been amazing in providing physical insight, no matter how crazy our ideas were or how unintelligible the experimental results we brought to their door. Our collaboration with Liang Tan, Johannes Lischner and Cheol-Hwan Park was incredibly stimulating and fruitful, and through their patient guidance I learned a lot about Green's functions.

It is well known that the UC Berkeley physics department has the most amazing student support staff in the world. My experience with Anne Takizawa, Donna Sakima, Claudia

Trujillo, and Kathy Lee have been a testament to that fact. Anne has been relentlessly helpful throughout my stay here. Donna always knew to brighten everyone's day with incredibly inventive email subjects, and Claudia and Kathy were an absolute joy to work with. The biggest mystery I have not yet solved here is: How do they do it?

# Chapter 1

# Introduction

Since Richard Feynman's famous speech "There's Plenty of Room at the Bottom" [1], many scientists have pushed the field of nanotechnology forward. In particular, progress has been made in the area of nanoelectronics where one of the main goals is to miniaturize electronic circuits down to the scale of single polymers, molecules, or atoms. The work presented in this dissertation is aimed at taking us further in that direction. One of our main results is to demonstrate a method to identify the products and intermediates of chemical reactions on surfaces by directly imaging them with individual-chemical-bond resolution using atomic force microscopy. We have used these reactions to synthesize conductive oligomers directly on a surface from the bottom up. Part of our motivation comes from the idea of using tailored chemical precursors for bottom-up synthesis of new nanoelectronic components such as graphene nanoribbons. In addition to creating new nanoelectronic elements, we have also developed a way of controlling the energy levels and charge states of molecular elements remotely and reversibly by applying a gate voltage to graphene, and then imaging the results at the single molecule level *via* scanning tunneling microscopy. This high level of control permits study of a number of fundamental physical questions, as well as the potential development of new applications in nanoelectronics.

For decades miniaturization has been one of the driving forces for advances in electronics and data storage. To date, electronic elements with feature sizes as small as a few nanometers have been achieved. Therefore, understanding the physics that governs processes at such lengths scales is essential to continue technological progress. For electron transport through such molecular elements, quantum effects play a major role, and so devices built from single molecule elements may enable new behavior that would not be possible with today's more macroscopic devices. This could, for example, enable the use of single electron spins in the emerging field of spintronics.

Devices such as single-molecule transistors as well as molecular machines based on coulomb interactions may help address fundamental questions in areas of many-body physics, such as the Kondo effect, electron-electron coulomb and spin interactions, and the Anderson impurity model [2]. In the case of molecules on graphene, control over the charge state may even enable novel physical systems like atomic collapse to be tuned.

Understanding and controlling structure is vitally important. Bottom-up on-surface synthesis of molecular electronic elements enables atomic level control over the final product. In bottom-up synthesis small elements like conductive polymers, carbon nanoribbons or other molecular structures can be assembled from smaller building blocks. This makes use of the natural tendency of self-assembly of molecules which can lead to reproducibly ordered functional structures. Understanding the processes involved in self-assembly and chemical reaction pathways is crucial to fine-tune and improve these techniques.

## 1.1 Previous work

Here I will give a brief overview of two specific areas. First, I will give an overview of the field of on-surface synthesis of nano-structures in UHV [3, 4], with brief examples of each of the main chemical reactions that have been used. Then I will discuss experiments on the electronic properties of molecules on surfaces like metals, semiconductors, ultra-thin insulating layers and graphene.

### 1.1.1 On-surface synthesis of nanostructures in UHV

On-surface polymerization is an emerging field that has gained much interest in the last decade because it may lead to atomically precise structures for molecular electronics and also give rise to interesting new chemistry due to the influence of the surface [4–6]. The study of atomically precise structures presents interesting opportunities for fundamental science. In particular I will discuss efforts to create covalently bonded structures because of their great technological promise. First I will describe how coupling reactions between aryl-halides, like Ullmann reactions [7, 8], have been used to create a variety of different extended nanostructures. Then I will give examples of other reaction mechanisms that have emerged recently but are less common.

Aryl-halide coupling reactions on surfaces are the most established and widely used reactions for achieving on-surface synthesis of covalently-bonded extended nanostructures. They are based on mechanisms like the Ullmann reaction [8] where aryl halides (usually a bromine or iodine atom connected to an aromatic ring) react with substrate copper atoms, forming a biaryl (coupling of two aromatic rings) and a copper halide. The Ullmann reaction is well established, but its precise reaction mechanism on surfaces is still under debate [5, 9–11].

On surfaces, the Ullmann reaction was first used to couple two individual molecules together using an STM tip in an experiment by Hla *et al.* [12]. Here an STM tip was used to induce the reaction between iodobenzene molecules and the copper surface to form aryl radicals, two of which were then laterally manipulated with the tip towards each other. A current pulse from the tip then induced the coupling reaction between them to form biphenyl. A procedure based on Ullmann-like self-assembly of molecules that yielded larger structures was later demonstrated by Grill and coworkers [13, 14]. This reaction involved brominated porphyrin molecules on Au(111). For porphyrins with two bromine substituents the bromines

dissociated from the molecules leaving behind diradicals, which then self-assembled into covalently bonded 1-D chains. Reactions between molecules with four substituents resulted in 2-D networks of porphyrins coupled on all four sides. A similar procedure was used to fabricate polyfluorene chains, which were subsequently lifted off the surface with an STM tip to measure the conductance as a function of the length [15, 16]. Atomically precise graphene nanoribbons with lengths of $\sim 30\,\mathrm{nm}$ were later synthesized by Roman Fasel and coworkers through a similar reaction on Au(111) followed by cyclodehydrogenation [17]. Wider nanoribbons were later assembled by Crommie and coworkers using a similar technique [18]. Using iodine substituted reactants, Fasel and coworkers have recently synthesized "porous graphene" structures on Ag(111) [19]. Many more studies have been done on using this versatile reaction pathway for on-surface polymerization [20–24].

Various other reaction mechanisms have additionally been used for on-surface synthesis. Cyclodehydrogenation has been used to form carbon nanoribbons [17, 18], "nano-graphene" tribenzocoronene [25], and fullerenes [26–28]. Alkyne coupling has been used to form polymeric networks [29, 30]. Radical $CH_2$ coupling has also been used [31], as well as imine bonds [32, 33], amide bonds [34, 35], and dehydration [36, 37]. Linear alkane polymerization [38] on Au(110) through surface templating has also been utilized, as well as click chemistry [39], Bergman cyclization [40], and the coupling of halide-substituted benzoic acids on an insulating calcite substrate [41].

### 1.1.2 Electronic properties of single molecules on surfaces

A number of techniques have been used to study the electronic properties of single molecules on surfaces [42], most prominently break-junction conductance measurements [43–47], thermoelectric measurements [48–50], and STM [51–56]. Additional nanoelectronic elements have been fabricated from single molecules in the form of amplifiers [57], transistors [44, 58–61], and switches [62]. Here I will specifically give an overview of scanning probe studies for molecules on surfaces. I will discuss studies performed on important substrates such as semiconductors, metals, ultra-thin insulating layers, and graphene.

The first scanning probe studies of molecules on surfaces were performed on graphite [63, 64] and molecular crystals [65]. Since then, the electronic structure of molecules on various semiconductor surfaces were studied by STM [66–73]. STM was also used to study the reactivity and growth of molecules on semiconductors [74–78].

STM studies of the electronic structure of molecules on metals are numerous [54, 79–81], in part due to the long history of experiments on metal substrates with STM. From the earliest studies on adsorption geometry [82], experiments have been performed on tip-induced reactions of molecules on metals [12, 83, 84], and phenomena like the Kondo effect [81, 85–88], negative differential resistance [89–91], molecule-metal charge transfer [54, 92–94], screening [95], photo-switching of molecules [96–100], inelastic tunneling [101–104], the Jahn-Teller effect [55, 105], atomic doping of molecules [56], and charging of molecules through local tip-gating [106–108]. However, charge states of single molecules have never previously been tuned remotely in a clean, single-molecule STM experiment.

Recently the growth of ultra-thin insulating layers of a few monolayers has enabled a new avenue for studying the electronic structure of molecules using STM [109, 110]. These ultra-thin layers consist of NaCl [111, 112], MgO [113], CuN [114], $Al_2O_3$ [115] or BN [116] on top of metal surfaces. When molecules adsorb onto such ultra-thin insulating layers, they become electronically decoupled from the underlying substrate, so that the usual electronic hybridization between molecular orbitals and substrate continuum states is significantly reduced. However, the insulating layer is sufficiently thin to allow tunneling processes and therefore measurement by STM. This decoupling causes the electronic structure of the molecules to be very similar to that of free molecules. This has allowed direct imaging of molecular orbitals [117, 118] which almost perfectly resemble theoretical images of the orbitals of free molecules. Additionally, charge states of individual atoms [51, 119] and molecules [120] have been controlled by the STM tip. Molecular switches have been realized [53, 84, 120–124], vibronic states of single molecules and polymers studied [52, 105, 123, 125–129], and single spins measured [114, 130–132].

Recently graphene has emerged as a promising new material for nanoelectronics [133–135]. The combination of graphene with functional organic molecules provides a number of intriguing possibilities [136]. On the one hand, molecules can be used to change graphene properties through nondestructive doping [136–140], and on the other hand graphene can be used to change the properties of adsorbed molecules *via* a gate. A number of transport and photoemission studies have already demonstrated that molecular adsorbates alter the electronic [137, 139–158], magnetic [146, 159, 160] and optical [161–163] properties of graphene. In STM experiments molecules deposited on graphene/metal systems showed that graphene acts as an effective electronic decoupling layer, similar to ultra-thin insulating layers, so that the free-molecule electronic properties can be probed [160, 164]. Additionally, the electronic structure of molecules on epitaxial graphene/SiC(0001) has been studied [152, 153, 156, 165–169], but studies of vibronic states for molecules on graphene are sparse [167]. In most graphene-on-metal systems the electronic structure of graphene is significantly altered, while graphene-on-SiC(0001) presents difficulties due to its complex surface structure. Neither of these configurations readily allow the application of a gate voltage in order to change the Fermi level of the graphene. Molecules have been studied in graphene-on-insulator substrates like $SiO_2$ or BN using STM [170], but the orbitals and charge states of the adsorbed molecules have not been previously tuned *via* gate electrodes in an STM experiment.

## 1.2 Outline of dissertation

In chapter 2 I describe the experimental methods used in this work. We utilized the established techniques of scanning tunneling microscopy (STM) and spectroscopy (STS), which are able to provide local topographic and electronic information of nanoelectronic structures. However, the chemical reactions that we studied involved organic bond rearrangements which turned adsorbed molecules into completely different, unknown structures, which could not be identified with STM alone (since STM only images electronic orbitals). As a result, we

needed to use a different technique that is better able to identify unknown adsorbates. To do this we chose to use the recently developed qPlus non-contact atomic force microscopy technique [171], which is able to identify unknown molecular adsorbates by directly imaging chemical bonds within a molecule [172].

Overall we have approached two problems in nanoelectronics: understanding new chemical reactions applicable to bottom-up synthesis of carbon nanostructures (chapter 3) and remotely tuning the molecular orbitals and charge states of individual molecules adsorbed onto graphene field-effect transistor (FET) devices (chapter 4).

The chemical reactions we have aimed to understand are a new class of surface-supported enediyne cyclization reactions [173] (section 3.1). These reactions could, in principle, be used to create extended carbon nanostructures, possibly even on insulating surfaces, which would lead to an ability of directly growing purely organic nanoelectronic devices that would not be "shorted out" by a metal substrate. To this end, we deposited 1,2-bis((2-ethynylphenyl)ethynyl)benzene on Ag(100) and annealed the surface to thermally induce cyclization cascades. While the resulting structures could not be identified by STM and density functional theory (DFT) alone, we were able to identify the products uniquely through qPlus AFM measurements. With the help of DFT, we then confirmed the corresponding reaction pathways. However, we did not observe any intermediates along these reaction pathways or intermolecular bonding.

For a different molecule, on the other hand, 1,2-bis(2-ethynylphenyl)ethyne, on the same surface Ag(100), we did observe both reaction intermediates and intermolecular bonding (section 3.2). We deposited this molecule and then annealed it to thermally induce the cyclization reactions mentioned above. After cooling down to cryogenic temperatures we used qPlus to take individual-bond-resolved images of a number of different structures, mostly dimers. We identified these structures to be intermediates along several reaction pathways. We were thus able to "freeze in" the intermediates and use them to directly map out the corresponding reaction pathways. On this surface these reactions resulted in, at most, only two molecules bonding.

Using the same precursor molecules on a different surface, Au(111), we succeeded in performing on-surface synthesis of extended oligomers, linking many monomers [174] (section 3.3). After heating this surface with adsorbed precursor molecules, the resulting oligomers had lengths of up to 20 monomers. We used qPlus imaging with sub-molecular resolution to identify the oligomers as polyacetylene derivatives, an important class of conductive polymers. Using the combined STM/AFM system we were able to correlate the electronic and chemical structure of these conductive oligomers.

We were able to achieve molecular orbital gating in an STM experiment for the first time by using a graphene FET device [175] (section 4.1). In this experiment, we deposited large benzene-derivative molecules 1,3,5-tris(2,2-dicyanovinyl)benzene (CVB) onto a graphene/BN/$SiO_2$ device with a doped Si back-gate electrode. We imaged the molecular LUMO and LUMO+1 orbitals of CVB using STS and were able to rigidly shift them in energy by applying a back gate. Using the gate we could switch between tunneling into the LUMO and LUMO+1 for the same applied sample bias. We also analyzed the vibronic

states of this system. Even though we could tune the orbital energies, we could not tune them across the Fermi level in order to change the charge states.

For a stronger acceptor molecule, tetrafluoro-tetracyanoquinodimethane (F4-TCNQ), on the same graphene FET device we were able to actually change the charge state of the molecules by applying a gate voltage (section 4.2). After deposition, F4-TCNQ p-doped the graphene and there was charge transfer between graphene and the adsorbed molecules. The degree of charge transfer per molecule depended on the detailed adsorption geometry of the molecules, which we imaged with sub-molecular resolution using qPlus AFM. Because single molecules were not stable enough for imaging, we co-deposited another type of molecule (10,12-pentacosadiynoic acid (PCDA)), which formed ordered islands and served as an anchor for the unstable F4-TCNQ. We then applied a gate to the system and used STS to confirm that we could change the charge state of the stabilized F4-TCNQ molecules between neutral and negatively charged.

# Chapter 2

# Experimental techniques

A number of different experimental methods are available to study molecules and polymers on surfaces and in thin films [176], and they can be roughly subdivided into momentum space and real space techniques. Momentum space imaging techniques measure the structure of materials in reciprocal space, for example through neutron or X-ray reflectivity. Spectroscopic information of the electronic structure of the substrate can be gained by angle-resolved photoemission spectroscopy and ultraviolet photoelectron spectroscopy, while chemical identity is typically probed using X-ray photoelectron spectroscopy or IR spectroscopy. In real space, the depth and composition of films can be analyzed through forward recoil spectrometry, nuclear reaction analysis and dynamic secondary ion mass spectrometry. Common microscopy techniques with resolutions on the nanometer scale are scanning electron microscopy, transmission electron microscopy, atomic force microscopy (AFM) and scanning tunneling microscopy (STM). Additionally, spectroscopic information on the local density of states can be gained through scanning tunneling spectroscopy (STS).

Of these methods I chose to use a combined STM/AFM system, because it has the ability to probe the topography and adsorption geometry of individual molecules and polymers, and to non-destructively image the intramolecular chemical bonds and local electronic structure of single molecules. All of these abilities have been essential for studying the physical systems described in this dissertation. Our main experimental instrument used in this work consists of a low temperature combined STM/AFM from Omicron, which can be used in STM or qPlus-AFM mode. It is operated at low temperature (4.6 K) and in UHV at base pressures of $< 1 \times 10^{-10}$ Torr. We use electronics and software from Specs/Nanonis to power and control the instrument.

In this chapter we will discuss the theoretical background of the measurement techniques used in this work, including STM (section 2.1), and FM-AFM (section 2.2).

## 2.1 STM Principles

The first scanning tunneling microscope was developed by Binnig, Rohrer, Gerber and Weibel [177–179]. Based on the quantum tunneling effect, it allowed imaging of surfaces with unprecedented resolution down to the atomic level.

An STM is operated by positioning a sharp tip wire within a distance of less than 1 nm of a sample surface with the gap creating a tunnel junction for electrons. Before sample and tip are brought into electrical contact their vacuum energies are aligned and their Fermi levels are different because they in general have different work functions (Fig. 2.1a). However, when they are brought into electrical contact the Fermi levels align, bringing the vacuum levels out of alignment, which creates an electric field between tip and sample (Fig. 2.1b). This is the origin of the contact potential difference, probed by electrostatic force microscopy or Kelvin probe force microscopy [180–182] (section 2.2.3). By applying a positive sample bias voltage between sample and tip ($V_s$ is defined to be positive if the sample is at higher potential) electrons can tunnel from the tip to sample because the Fermi level in the tip is higher and empty electron states in the sample are available to tip electrons at this higher energy (Fig. 2.1c). It is clear that the tunnel current depends on the density of states of the sample, as discussed below. When the applied sample bias is negative, the Fermi level of the tip is shifted below the Fermi level of the sample, thereby allowing electrons to tunnel from sample to tip (Fig. 2.1d).

A theoretical understanding of the tunnel current was developed by Bardeen [183] and Tersoff and Hamann [184]. A good introduction to STM is given by Chen [185]. The tunnel current, for sample bias $V$, is given by

$$I(V) \propto \int_{-\infty}^{\infty} \rho_s(E)\rho_t(E-eV) \left|M_{t-s}(E,V,z)\right|^2 \left[f(E-eV)-f(E)\right] \,\mathrm{d}E, \tag{2.1}$$

where $\rho_s$ and $\rho_t$ are the density of states of the sample and tip, respectively, $M_{t-s}(E,V,z)$ is the matrix element for the tunneling process, $f(E)$ is the Fermi-Dirac function, $z$ is the tip height and $E$ is energy. To understand this expression more intuitively we can assume $T = 0\,\mathrm{K}$ (which turns the Fermi-Dirac function into a step function) and also assume a featureless tip density of states so that $\rho_t$ can be pulled out of the integral and subsumed in the proportionality constant. It is also convenient to approximate the square of the tunneling matrix element with an exponential factor that depends only the tunneling barrier (which is related to the sample work function) and is approximated to be independent of energy. Doing this yields:

$$I(V) \propto \exp(-2\kappa z) \int_0^{eV} \rho_s(E_F+E) \,\mathrm{d}E, \tag{2.2}$$

where $\kappa = \sqrt{2m_e\phi_s/\hbar^2}$ and $\phi_s$ is the local effective work function of the sample. This equation shows how a scanning tunneling microscope can be operated in two main modes,

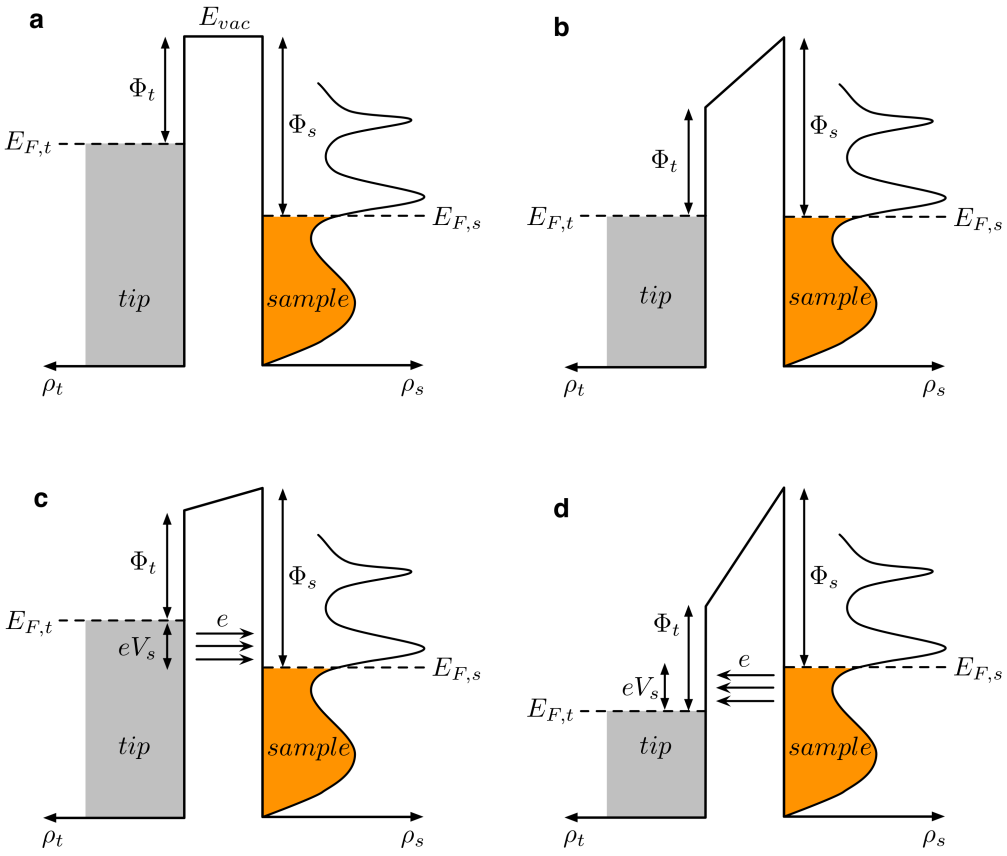


Figure 2.1: Energy alignment in STM measurements. **(a)** The tip is modeled to have a flat, featureless density of states $\rho_t$, while the sample has features in $\rho_s$. Before tip and sample are connected in a circuit, their vacuum levels $E_{vac}$ align, while their Fermi levels $E_{F,t}$ and $E_{F,s}$, in general, are different. **(b)** When tip and sample are connected, charges flow to align the Fermi levels, mostly by rigidly shifting the band structures through the creation of an electric field, rather than changes in the Fermi levels relative to the band structures (because the densities of states are large). **(c)** A positive bias voltage is applied to the sample which shifts the energies of the electrons in the tip to higher energies (again the rigid band structure, not the Fermi levels). This leads to electrons from the higher energies in the tip tunneling through the vacuum into empty states in the sample. **(d)** A negative bias voltage is applied to the sample, lowering the energies of electrons in the tip, allowing electrons from the sample to tunnel to the empty states on the tip.

measuring the current as a function of lateral position to obtain an "image" of the surface (scanning tunneling microscopy) or as a function of applied bias voltage to obtain energy-resolved information about the sample local density of states (scanning tunneling spectroscopy). In the following we will discuss these two modes in more detail.

### 2.1.1 Scanning tunneling microscopy

In scanning tunneling microscopy mode the tip is scanned laterally over the sample surface while the current is recorded to obtain an "image" of the surface. This is not an image in the traditional sense, and it also does not reflect the physical topography of the surface, since the tunnel current (2.2) does not simply depend on tip height. There are two main modes for scanning laterally: constant tip height, or constant tunnel current. Constant height scans are achieved by setting the piezo-controlled tip height to a constant value. This mode makes interpretation of images slightly more straightforward for comparison with theory (especially when doing scanning tunneling spectroscopy maps, see next section), but have the disadvantage that the tip can collide with tall features on an unknown sample surface. Therefore, usual operation is in constant current mode. This is achieved by using a feedback mechanism to control the tip height in order to achieve a predetermined tunnel current set-point. The image is then a map of the tip height corresponding to constant current contours.

A detailed description of contrast mechanisms in STM images is given for example in [185, 186]. From (2.2) we can see that there are two main sample attributes that influence the tunnel current and can therefore give rise to a contrast in both constant height or constant current images. They are as follows:

**Sample height -** This corresponds to the physical z-position of atoms on the sample surface and enters (2.2) by changing the relative tip height $z$. When this is the dominant contribution to lateral contrast the image corresponds very closely to the topography of the sample surface. Examples are atomic steps and terraces on a clean metallic surface.

**Local density of states -** The local density of states can have lateral variation and is a purely electronic effect on imaging contrast. When this is the dominant contribution to the contrast the image corresponds to maps of electronic states of the surface. Examples of this are molecular adsorbates (when resonantly tunneling into a molecular orbital) or the Shockley surface state [187].

### 2.1.2 Scanning tunneling spectroscopy

In addition to imaging the surface one can also perform spectroscopic measurements using STM tunnel current. In this technique [188] the tip is held at a constant height and the sample bias is swept while the current ($I$) is recorded as well as $\mathrm{d}I/\mathrm{d}V$ (using a lock-in amplifier). From (2.2), we can see that

$$\left(\frac{\mathrm{d}I}{\mathrm{d}V}\right)_{V=V'} \propto \rho_s(E_F + eV'), \tag{2.3}$$

so this signal allows a direct measurement of the sample local density of states. This has been a powerful tool to study, for example, electronic states of metals [189], molecular orbitals [110, 117, 122], and semiconductor band gaps [190]. In addition to yielding local information, it also has the advantage of being sensitive to both, filled and empty electronic states. A number of ensemble spectroscopic techniques access filled states only.

In an extension of this technique, the tip can be scanned laterally at constant height as $\mathrm{d}I/\mathrm{d}V$ is recorded for a constant sample bias. The resulting $\mathrm{d}I/\mathrm{d}V$ map corresponds to an image of the local density of states at a given height and energy. This can be a useful method to understand spatial variation in the electronic structure of a sample.

## 2.2 qPlus/FM-AFM principles

qPlus AFM, developed by Franz Giessibl [171, 191–193], is a version of frequency modulated noncontact AFM (FM-AFM) [194, 195], which is an extension of the original atomic force microscopy technique [196]. qPlus has a number of advantages over traditional FM-AFM when it comes to operating in a combined STM/AFM system for imaging molecular bonds. The differences between qPlus and traditional FM-AFM are summarized in Table 2.1. In particular, the characteristics of qPlus that make it useful for molecular studies are the following:

**Quartz cantilevers -** Quartz cantilevers have very small temperature dependence of the resonance frequency, as opposed to conventional silicon cantilevers whose frequency variations can be as large as the measurement signal for temperature variations of $< 1\,\mathrm{K}$ [197].

**Very stiff cantilevers -** qPlus cantilevers (also called "tuning forks" because they are made from quartz tuning forks of which one side is glued to a base, effectively turning them into cantilevers) have very high stiffness of $k \approx 1800\,\mathrm{N\,m^{-1}}$. This allows for operation at very small oscillation amplitudes because the restoring force is large even for small amplitudes, thereby preventing jump-to-contact when operating at small tip heights even in the presence of strong tip-sample interaction.

**Very small oscillation amplitudes -** Due to the high stiffness of qPlus cantilevers, very small oscillation amplitudes can be achieved ($< 1\,\text{Å}$). This is particularly useful when probing short-range Pauli repulsion forces in order to image chemical bond structure. By using small oscillation amplitudes the tip spends more time close to the sample where the Pauli exclusion forces are relevant, achieving a better signal to noise ratio. In addition, for small oscillation amplitudes the measurement signal is easier to interpret because in this

case the frequency shifty is proportional to the force gradient. The very small oscillation amplitudes are also beneficial for performing simultaneous STM and AFM measurements. Since the STM bandwidth is much lower than the oscillation frequency, the measured current is the average current during one cycle. For two different amplitudes, given the same distance of smallest approach (in order to avoid point contact) a larger amplitude has a smaller current signal because the tip spends less time near the surface. This means that small amplitudes have better signal to noise ratios for simultaneous STM/AFM measurements [197].

**Piezoelectric sensing -** The measurement signal in a qPlus sensor is measured directly from electrodes within the sensor, making use of the piezoelectric charges generated by the deflection of the piezoelectric quartz cantilever. In contrast to conventional piezoresistive measurements in silicon sensors, this dissipates very little power and is therefore advantageous for low temperature operation [197]. The amount of charge created is proportional to the stiffness $k$, which is very high for qPlus sensors.

**High Q-factor -** For qPlus high Q-factors of $10^5$ are routinely achieved, which are beneficial for achieving high signal-to-noise ratios because a high Q-factor results in low thermal noise according to [194]:

$$\delta f_{thermal}/f_0 \propto \sqrt{\frac{1}{f_0 Q}}, \tag{2.4}$$

where $f_0$ is the natural resonance frequency and $Q$ is the Q-factor. On the other hand, Q should not be too large because it makes the amplitude feedback less stable [197].

**High resonance frequency -** The relatively high resonance frequency of qPlus sensors of around 30 kHz keeps the thermal noise (2.4) low. Very high frequencies, however, can increase the detection noise, so increasing the frequency does not necessarily yield better noise.

Table 2.1: Conventional FM-AFM vs. qPlus [197]

| **Conventional FM-AFM** | **qPlus** |
|---|---|
| silicon | quartz |
| flexible cantilever: $k \approx 20\,\mathrm{N\,m^{-1}}$ | stiff cantilever: $k \approx 1800\,\mathrm{N\,m^{-1}}$ |
| large amplitude: $A \approx 10\,\mathrm{nm}$ | small amplitude: $A < 1\,\mathrm{\AA}$ |
| piezoresistive or optical detection | piezoelectric detection |
| low Q-factor: $Q \approx 3 \times 10^4$ | high Q-factor: $Q \approx 10^5$ |
| resonance frequency: $f_0 > 100\,\mathrm{kHz}$ | resonance frequency : $f_0 \approx 30\,\mathrm{kHz}$ |

In the following we will discuss in detail how these characteristics enable a complementary measurement signal to STM. We will start with the theoretical fundamentals of qPlus FM-AFM in section 2.2.1, before discussing the origin of sub-molecular chemical bond contrast in section 2.2.2. Then we will give a brief overview of electrostatic force microscopy in section 2.2.3.

### 2.2.1 qPlus fundamentals

The measurement signal for a qPlus sensor, as in conventional frequency modulated AFM, is the frequency shift of the resonance frequency of the sensor. Giessibl gives an introduction to the theory of qPlus in [197, 198] and we will give an overview of his arguments below.

In FM-AFM, the cantilever supplies a restoring force to the tip which results in simple harmonic motion with a natural frequency of

$$f_0 = \frac{1}{2\pi}\sqrt{\frac{k}{m^*}}, \tag{2.5}$$

where $k$ is the spring constant of the cantilever and $m^*$ is the effective mass of the oscillator, which takes into account that the cantilever is not a point mass. When the tip is brought into proximity of the sample there exists an additional force on the oscillating sensor $F_{ts}$. This tip-sample interaction force changes the resonance frequency of the cantilever away from the natural unperturbed resonance $f_0$. If we assume that the force is a linear function of the tip height $z$, which is a reasonable approximation for the small amplitudes of the qPlus sensor, the effect on the frequency is the same as adding another spring between tip and sample with spring constant $k_{ts}$:

$$f = \frac{1}{2\pi}\sqrt{\frac{k + k_{ts}}{m^*}}. \tag{2.6}$$

This approximation would have to be modified for the larger amplitudes of conventional FM-AFM, but here we concentrate only on the special case of qPlus, with small amplitudes. For the very stiff cantilevers of qPlus $k \gg k_{ts}$, so we can taylor expand (2.6) and approximate the frequency shift as

$$\Delta f = f - f_0 = \frac{f_0}{2k} k_{ts} = -\frac{f_0}{2k} \frac{\partial F_{ts}}{\partial z}. \tag{2.7}$$

From this we can see that for small amplitudes and the high stiffness of the qPlus sensor the frequency shift is proportional to the negative tip-sample force gradient. The high stiffness has the practical advantage of keeping $\Delta f$ small, which eases the amplitude feedback and results in lower measurement noise. For larger amplitudes, one needs to consider the weighted average $k_{ts}$ over an oscillation cycle [199]. It can easily be seen that if amplitudes are large, most of the signal will be due to long range forces, since the tip spends little time in the region where short-range forces are relevant. In contrast, for small tip-sample distances and amplitudes the signal is dominated by short range forces. An analysis of the thermal noise [194] and detector noise [197, 200] as a function of amplitude as well as the signal from a particular force as a function amplitude shows that the best signal-to-noise ratio is achieved when tuning the amplitude to the characteristic length scale of the interaction and to scan at slow speeds [198]. In the case of Pauli-repulsion forces which are the origin of molecular bond resolution images in [172, 173], this means amplitudes of $\sim 1\,\text{Å}$ are needed.

### 2.2.2 Origin of sub-molecular resolution

Gerhard Meyer and coworkers have shown that the internal chemical bond structure of molecules can be imaged with qPlus AFM if the tip is functionalized [172] and scanned in constant height mode at small tip heights over a molecule. The necessity of constant height imaging arises due to the non-monotonic function of $\Delta f(z)$ (see Fig. 2.2), which does not allow stable feedback operation. The highest resolution to date can be achieved by functionalizing the tip with a CO molecule. It is known that it adsorbs with the C atom connected to the tip and the O atom pointing away from it [201]. This gives rise to the high resolution for three main reasons:

1. The tip is terminated by a single oxygen atom which allows good lateral resolution.
2. The probing part of the tip (oxygen atom) is far away from the rest of the tip, so forces between sample and metal tip are not appreciable.
3. The CO molecule is inert, so it does not react with most sample molecules at the very small operational distances.

In the following we will describe the origin of the contrast in qPlus images with sub-molecular resolution [172–174]. Detailed theories of this contrast mechanism have been developed [172, 202–210] and here we will show how these theories can be understood intuitively.

The interaction potential between the tip and sample as a function of tip height $z$ can be described by a Morse potential [211], Lennard-Jones potential [212] or Stillinger-Weber potential [213]. The Lennard-Jones potential $V_{LJ}$, is sufficient as a qualitative model of the potential. We can then get the force and force gradient by differentiation:

$$V_{LJ}(z) \propto \left[\left(\frac{z_m}{z}\right)^{12} - 2\left(\frac{z_m}{z}\right)^{6}\right] \tag{2.8}$$

$$F(z) \propto \left[\frac{z_m^{12}}{z^{13}} - \frac{z_m^{6}}{z^{7}}\right] \tag{2.9}$$

$$-\frac{dF(z)}{dz} \propto \left[13\,\frac{z_m^{12}}{z^{14}} - 7\,\frac{z_m^{6}}{z^{8}}\right]. \tag{2.10}$$

Here $z_m$ is where the potential reaches its minimum (Fig. 2.2a). In this model the interaction is governed by long-range forces due to electrostatic and van der Waals interactions and short-range forces due to Pauli exclusion. At large tip-sample distances the force gradient is dominated by long-range forces and at these large tip heights the lateral differences in interaction are negligible (Fig. 2.2b), the small differences leading to slightly lower frequency shift values above a molecule compared to the substrate. For imaging a molecule this leads to a featureless region of negative frequency shift over the molecule. However, at smaller tip sample distances the short-range forces begin to dominate the interaction when the force reaches a minimum, i.e. when the force gradient and the frequency shift cross zero. In this case, for a lateral scan over a molecule, the short-range force gradient gives a large signal when the tip is above a carbon atom but not when it is above the center of a carbon ring or above the substrate, which has a much larger distance to the tip (Fig. 2.2b). This gives rise to the intramolecular contrast from short-range interactions.

The Pauli exclusion principle [214] is at the heart of these short range interactions. In essence, when two atoms come close to each other (here the oxygen probe atom of the tip and the sample atom of the molecule) then the wave functions need to remain orthogonal to each other due to the Pauli exclusion principle. For this to be possible as the atoms are brought close, the wavefunctions' curvature, and therefore kinetic energy, increases. This increase in kinetic energy creates the repulsive force between atoms.

A simple model for this interaction was developed by Meyer and coworkers [202] and is summarized below. Let us take the example of two hydrogen atoms. Their ground-state wavefunctions for the same spin are, using atomic units:

$$\psi_1(r,\phi,\theta) = \frac{1}{\sqrt{\pi}}\exp(-r) \tag{2.11}$$

$$\psi_2(r,\phi,\theta) = \frac{1}{\sqrt{\pi}}\exp(-\sqrt{r^2+R^2-2rR\cos\phi}, \tag{2.12}$$

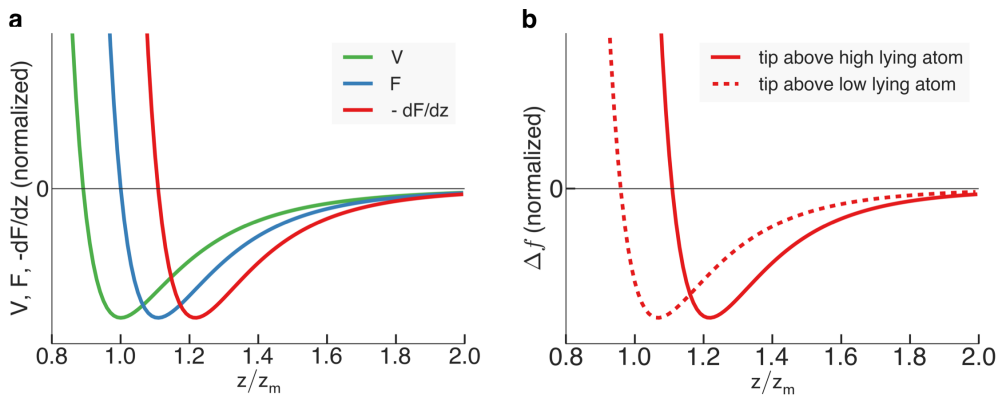


Figure 2.2: Tip-sample interaction. **(a)** The tip-sample interaction potential $V$, the z-component of the force $F$ and the negative force gradient $-\frac{dF}{dz}$, all normalized by their respective values at their minimum. The x-axis is normalized by the tip height at the potential minimum $z_m$. Successive derivatives qualitatively move the curves to the right. At tip heights where repulsive forces become relevant (at the force minimum), the force gradient and therefore the frequency shift cross zero. **(b)** The calculated frequency shift (which is proportional to the negative force gradient) for two different lateral positions of the tip, one above an atom that is close, one above a lower lying atom. In this case there is a clear difference in the measured $\Delta f$ at lower tip heights, while it is similar at higher tip heights. This is an aspect that leads to higher intramolecular contrast when bringing the tip close, compared to far away. Another aspect not taken into account in this simple model is that the z-component of force from neighboring atoms (in addition to the atom exactly below the tip) influences the tip more at greater tip heights, reducing the lateral contrast even further.

where R is the distance between atoms. When they are brought near each other they need to be orthogonalized. Without loss of generality we assume that $\psi_2$ of the probe atom changes in order to become orthogonal to $\psi_1$ of the sample atom. The resulting increase of kinetic energy is due to the difference in kinetic energy of the orthogonalized $\psi_2'$ and the original $\psi_2$. This change in kinetic energy, for the relatively large distances relevant for us (several atomic radii) reduces to:

$$\Delta E_{\text{kin}} \approx \frac{2}{9} \exp(-2R) R^2 (3 + 3R + R^2). \tag{2.13}$$

Here the exponential $\exp(-2R)$ is proportional to the charge density $|\psi_1|^2$ of the sample atom. We assume that the hydrogen-like treatment of atoms is still a good approximation for atoms with higher atomic numbers and so the resulting increase in kinetic energy depends on each of the atoms' atomic numbers and has a more complicated form of exponentials and powers of $R$. However, even in those cases the exponential term dominates at large distances, so we can approximate the kinetic energy increase as the simple form:

$$\Delta E_{\text{kin}}(R) = A \left[\rho_s(R)\right]^B, \tag{2.14}$$

where A and B are parameters and $\rho_s(R)$ is the sample charge density at the position R, the position of the probe atom. The pre-factor A and exponent B are corrections to the purely

exponential behavior of the charge density arising from the polynomial terms in $\Delta E_{\text{kin}}$, which make it decay slightly slower. From this we can see that the interaction energy at a distance $R$, which is proportional to the integral of $\Delta E_{\text{kin}}(z)$ from $R$ to infinity, can be approximated to be purely a function of the charge density of the sample atom. Therefore the frequency shift, the second derivative of the interaction energy, also is a function of the charge density. In fact, qualitatively, constant height images of frequency shift of a flat sample molecule can be interpreted to reflect the charge density of the molecule, similar to how constant height $\mathrm{d}I/\,\mathrm{d}V$ maps reflect the sample molecule LDOS.

### 2.2.3 Electrostatic force microscopy

Similar to STS, by sweeping the sample bias and recording the frequency shift in FM-AFM we can gain additional information. In this case, however, the signal is usually less feature-rich than $\mathrm{d}I/\,\mathrm{d}V$, since $\Delta f(V)$ usually has a simple parabolic shape. Nevertheless, the maximum of the parabola gives a measure of the local contact potential difference (LCPD), which is related to the work function of the sample, and is not directly accessible by STM/STS. Such measurements of bias dependent frequency shift represent a variant of electrostatic force microscopy (EFM). In similar techniques like Kelvin probe force microscopy an ac-voltage is applied in addition to the dc sample bias, which allows scanning of the sample, yielding a map of the LCPD.

In this work we implement EFM by taking point bias sweeps at individual locations of the sample (as in [119]), which can give information on the charge state of atoms/molecules because the LCPD is sensitive to local charge. In practice this can be done at many points on a grid, thus yielding a map of the LCPD. This approach has been used, for example, to map out the internal charge distribution within a single molecule [215].

In the following we give a theoretical overview of the relationship between the frequency shift and the LCPD (for more detailed background, see [180–182]). As discussed before, the relevant tip-sample interaction forces are Pauli repulsion, and van der Waals and electrostatic attraction. As opposed to chemical bond imaging of section 2.2.2, EFM is done in the attractive regime where only van der Waals and electrostatic forces are relevant. The van der Waals forces are not dependent on sample bias so the only component of the interaction force with a voltage dependence is the electrostatic force, whose z-component (to which vertical FM-AFM is sensitive) we can write as the gradient of the capacitive energy $U_{el} = {}^1\!/_2\, CV^2$ between tip and sample [181]:

$$F_{el,z} = +\frac{\partial U_{el}}{\partial z} = \frac{1}{2}\frac{\partial C}{\partial z}V^2 \tag{2.15}$$

where $V$ is the total potential difference between tip and sample, $C$ is the capacitance of the tip-sample system, and $V$ is independent of $z$. Note that the force is the positive gradient [216] of the energy when the voltage is kept constant because one has to take into account the energy of charges in the source of the applied bias [217]. The total potential

difference is given by the difference of the applied sample bias $V_s$ and the contact potential difference $V_{CPD}$, if we use the definition

$$V_{CPD} = \frac{1}{e}(\Phi_{sample} - \Phi_{tip}). \tag{2.16}$$

Now the electrostatic force becomes

$$F_{el,z} = \frac{1}{2}\frac{\partial C}{\partial z}(V_s - V_{CPD})^2. \tag{2.17}$$

Since the measurement signal is the frequency shift, which can be taken as proportional to the negative force gradient for small amplitudes as in (2.7), we get

$$\Delta f(V_s) = -\frac{f_0}{2k}\frac{\partial F_{el,z}}{\partial z} = -\frac{f_0}{4k}\frac{\partial^2 C}{\partial z^2}(V_s - V_{CPD})^2, \tag{2.18}$$

which usually is a parabola with negative curvature when $\partial^2 C/\partial z^2$ is positive, however positive curvature parabolae have been observed due to the so-called phantom force [216] when the simple equation above no longer holds. According to (2.18) $\Delta f$ has a maximum at $V_s = V_{CPD}$, which therefore yields the local contact potential difference, a measure of the work function of the sample (see (2.16)).

## 2.3 Conclusion

In this chapter we gave an introduction to the techniques of STM and qPlus-AFM and demonstrated the versatility of a combined STM/qPlus-AFM system. STM can give information on topography with single-atom vertical and lateral resolution, and can be used to manipulate single atoms and molecules [218]. Additionally its spectroscopic variant, STS, provides information on the local density of states of systems as small as single atoms, molecules, and polymers on surfaces. Since STM is only sensitive to the electronic states near the Fermi energy, these states have a large influence on the "topography" images. In particular, when imaging adsorbed molecules, STM images represent the extended orbitals near the Fermi level of the molecules. In contrast, a strength of qPlus AFM is to image very short range forces, like Pauli repulsion between chemical bonds and the tip, which can be used to capture images of molecules with single atom and chemical bond resolution. Additionally, bias-dependent qPlus-AFM can yield information on the local work function of a sample, including the charge state of molecules with sub-molecular resolution.

# Chapter 3

# Imaging individual chemical bonds in reaction products

One of the reasons molecular electronics has so much promise is that the chemical and electronic structure of molecules and organic materials can be tailored to specific applications with a high level of control. When developing new devices for molecular electronics it is therefore critical to precisely understand the intra- and intermolecular bond configurations, in addition to electronic orbitals of the molecules. This can be a challenge for new bottom-up synthesized molecules and polymers, where the products of a chemical reaction are not known *a priori*. To address this we have taken three specific steps towards understanding both chemical reactions on surfaces and the resulting chemical and electronic structure of their products.

Section 3.1 discusses our use of combined qPlus AFM and STM techniques to image the chemical structure of the products of enediyne cyclization cascades [219] for molecules on Ag(100) [173]. The goal of this chemical reaction was to synthesize extended carbon nanostructures through bottom-up synthesis using cyclization reactions. However, the precursor molecules did not turn into extended graphene nanostructures, but rather into single molecule products. In order to tune the chemical reaction to yield more extended products it was necessary to uniquely identify the reaction products. The products of this reaction could not be identified with STM and DFT alone, because the number of possible structures was too large and the simulated DFT images too similar for each of them. Therefore, we employed the CO-modified qPlus AFM technique [172] to measure the internal bond structure of the products and thereby uniquely identify them.

Section 3.2 discusses our investigation of intermediates of the enediyne cyclization reactions on Ag(100). Since the first molecules we explored (section 3.1) did not produce intermolecular bonding or intermediate structures we moved to a different molecule: 1,2-bis(2-ethynylphenyl)ethyne. This molecule underwent cyclization reactions on Ag(100) and did lead to both intermolecular bonding and intermediate species. We used qPlus AFM to identify the intermediates and map out specific reaction pathways for the many products of these enediyne cyclizations on Ag(100).

Section 3.3 discusses cyclization reactions of enediynes on Au(111) resulting in step-growth of oligomers belonging to the technologically relevant conductive polymer class of polyacetylene derivatives [175]. The new reaction mechanism we observed here is interesting because it could possibly lead to the on-surface synthesis of conductive polymers on insulating surfaces [220], which is rarely achieved [16, 41] and could enable studies of the electronic structure of polymers, without the disturbing influence of a metal substrate. Again, due to the complicated nature of the reaction there are, in principle, a number of possible reaction products, many of which are realized on the surface. By using the qPlus technique we were able to identify them. For these oligomers we additionally studied the electronic structure and found that the LUMO of the oligomers lies at a much lower energy than the LUMO of the monomeric building blocks due to delocalization and efficient $\pi$-orbital overlap and screening effects. We visualized the particle-in-a-box-like spatial structure of the oligomer LUMO along the conjugated backbone of the oligomer, demonstrating its conductive nature.

## 3.1 Imaging internal bond structure of cyclization reaction products on Ag(100)

This section was originally published in **Science** [173].

Observing the intricate chemical transformation of an individual molecule as it undergoes a complex reaction is a longstanding challenge in molecular imaging. Advances in scanning probe microscopy now provide the tools to visualize not only the frontier orbitals of chemical reaction partners and products, but their internal covalent bond configurations as well. We used noncontact atomic force microscopy to investigate reaction-induced changes in the detailed internal bond structure of individual oligo-(phenylene-1,2-ethynylenes) on a (100) oriented silver surface as they underwent a series of cyclization processes. Our images reveal the complex surface reaction mechanisms underlying thermally induced cyclization cascades of enediynes. Calculations using *ab initio* density functional theory provide additional support for the proposed reaction pathways.

Understanding the microscopic rearrangements of matter that occur during chemical reactions is of great importance for catalytic mechanisms and may lead to greater efficiencies in industrially relevant processes [221, 222]. However, traditional chemical structure characterization methods are typically limited to ensemble techniques where different molecular structures, if present, are convolved in each measurement [223]. This limitation complicates the determination of final chemical products, and often it renders such identification impossible for products present only in small amounts. Single-molecule characterization techniques such as scanning tunneling microscopy (STM) [12, 224] potentially provide a means for surpassing these limitations. Structural identification using STM, however, is limited by the microscopic contrast arising from the electronic local density of states (LDOS), which is not always easily related to chemical structure. Another important subnanometer-resolved

From [173]. Reprinted with permission from AAAS.

technique is transmission electron microscopy (TEM). Here, however, the high-energy electron beam is often too destructive for organic molecule imaging. Recent advances in tuning fork-based noncontact atomic force microscopy (nc-AFM) provide a method capable of nondestructive sub-nanometer spatial resolution [121, 172, 210, 225–229]. Single-molecule images obtained with this technique are reminiscent of wire-frame chemical structures and even allow differences in chemical bond order to be identified [227]. Here we show that it is possible to resolve with nc-AFM the intramolecular structural changes and bond rearrangements associated with complex surface-supported cyclization cascades, thereby revealing the microscopic processes involved in chemical reaction pathways.

Intramolecular structural characterization was performed on the products of a thermally induced enediyne cyclization of 1,2-bis((2-ethynylphenyl)ethynyl)benzene (**1**). Enediynes exhibit a variety of radical cyclization processes known to compete with traditional Bergman cyclizations [230, 231], thus often rendering numerous products with complex structures that are difficult to characterize using ensemble techniques [232]. To directly image these products with subnanometer spatial resolution, we thermally activated the cyclization reaction on an atomically clean metallic surface under ultrahigh vacuum (UHV). We used STM and nc-AFM to probe both the reactant and final products at the single-molecule level. Our images reveal how the thermally induced complex bond rearrangement of **1** resulted in a variety of unexpected products, from which we have obtained a detailed mechanistic picture - corroborated by *ab initio* density functional theory (DFT) calculations - of the cyclization processes.

### 3.1.1 Methods

We synthesized 1,2-bis((2-ethynylphenyl)ethynyl)benzene (**1**) through iterative Sonogashira cross-coupling reactions. We deposited **1** from a Knudsen cell onto a Ag(100) surface held at room temperature under UHV. Molecule-decorated samples were transferred to a cryogenic imaging stage ($T \leq 7\,\mathrm{K}$) before and after undergoing a thermal annealing step. Cryogenic imaging was performed both in a home-built $T = 7\,\mathrm{K}$ scanning tunneling microscope and in a qPlus-equipped [193, 197] commercial Omicron LT-STM/AFM at $T = 4\,\mathrm{K}$. nc-AFM images were recorded by measuring the frequency shift of the qPlus resonator while scanning over the sample surface in constant-height mode. For nc-AFM measurements, the apex of the tip was first functionalized with a single CO molecule [172]. To assess the reaction pathway energetics, we performed *ab initio* DFT calculations within the local density approximation [233] using the GPAW (Grid-based Projector Augmented Wavefunction) code [234, 235].

### 3.1.2 Results

Figure 3.1 shows a representative STM image of **1** on Ag(100) before undergoing thermal annealing. The adsorbed molecules each exhibited three maxima in their LDOS at positions

From [173]. Reprinted with permission from AAAS.

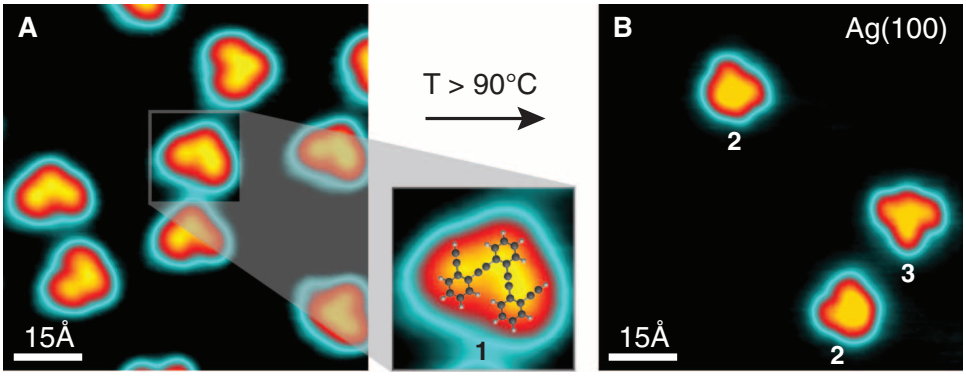


Figure 3.1: STM images of a reactant-decorated Ag(100) surface before and after thermally induced cyclization reactions. **(A)** Constant-current STM image of **1** as deposited on Ag(100) ($I = 25$ pA, $V = 0.1$ V, $T = 7$ K). A model of the molecular structure is overlaid on a close-up STM image. **(B)** STM image of products **2** and **3** on the surface shown in (A) after annealing at $T = 145\,^{\circ}$C for 1 min ($I = 45$ pA, $V = 0.1$ V, $T = 7$ K).

suggestive of the phenyl rings in **1** (Fig. 3.1A). Annealing the molecule-decorated Ag surface up to 80 °C left the structure of the molecules unchanged. Annealing the sample at $T >= 90\,^{\circ}$C, however, induced a chemical transformation of **1** into distinctively different molecular products (some molecular desorption was observed). Figure 3.1B shows an STM image of the surface after annealing at 145 °C for 1 min. Two of the reaction products can be seen in this image, labeled as **2** and **3**. The structures of the products are unambiguously distinguishable from one another and from the starting material **1**, as shown in the close-up STM images of the most common products **2**, **3** and **4** in Fig. 3.2, B to D. The observed product ratios are 2:3:4 = (51 ± 7%):(28 ± 5%):(7 ± 3%), with the remaining products comprising other minority monomers as well as fused oligomers (Fig. 3.3).

Detailed subnanometer-resolved structure and bond conformations of the molecular reactant **1** and products (**2**, **3**, and **4**) were obtained by performing nc-AFM measurements of the molecule-decorated sample both before and after annealing at $T \geq 90\,^{\circ}$C. Figure 3.2E shows a nc-AFM image of **1** before annealing. In contrast to the STM image (Fig. 3.2A) of **1**, which reflects the diffuse electronic LDOS of the molecule, the AFM image reveals the highly spatially resolved internal bond structure. A dark halo observed along the periphery of the molecule is associated with long-range electrostatic and van der Waals interactions [172, 203]. The detailed intramolecular contrast arises from short-ranged Pauli repulsion, which is maximized in the regions of highest electron density [203]. These regions include the atomic positions and the covalent bonds. Even subtle differences in the electron density attributed to specific bond orders can be distinguished [227], as evidenced by the enhanced contrast at the positions of the triple bonds within **1**. This effect is to be distinguished from the enhanced contrast observed along the periphery of the molecule, where spurious effects (e.g.,

From [173]. Reprinted with permission from AAAS.

because of a smaller van der Waals background, enhanced electron density at the boundaries of the delocalized $\pi$-electron system, and molecular deviations from planarity) generally influence the contrast [203, 227].

Figure 3.2, F to H, shows subnanometer-resolved nc-AFM images of reaction products **2**, **3**, and **4** that were observed after annealing the sample at $T > 90\,^{\circ}\mathrm{C}$. The structure of these products remained unaltered even after further annealing to temperatures within the probed range from 90 °C to 150 °C (150 °C was the maximum annealing temperature explored in this study). The nc-AFM images reveal structural patterns of annulated six-, five-, and four-membered rings. The inferred molecular structures are shown in Fig. 3.2, J to L. Internal bond lengths measured by nc-AFM have previously been shown to correlate with Pauling bond order [227], but with deviations occurring near a molecules periphery, as described above. As a result, we could extract clear bonding geometries for the products (Fig. 3.2, J to L), but not their detailed bond order. The subtle radial streaking extending from the peripheral carbon atoms suggests that the valences of the carbon atoms are terminated by hydrogen [203]. This is in agreement with molecular mass conservation for all proposed product structures and indicates that the chemical reactions leading to products **2**, **3**, and **4** are exclusively isomerization processes. Figure 3.2G suggests a four-membered ring between two six-membered rings, but does not resolve it perfectly. DFT calculations indicate that other structural isomers, such as an eight-membered ring next to a six-membered ring, are energetically very unfavorable relative to the structure of **3**.

Images of other minority products (**9** and **10**) are included in Fig. 3.3. The bonding structure of **9** is non-planar and thus leads to a complex contrast in the nc-AFM images that hampers direct structure determination. Product **10** is the result of two $C^1{-}C^5$ cyclizations on the sterically less hindered outer enediynes in combination with a $C^1{-}C^6$ cyclization on the inner enediyne. The AFM contrast of the terminal carbon atom in the C=C bonds of **10** is lower than expected. We attribute this to a molecular distortion resulting from the stabilizing interaction between the Ag surface and the terminal $sp^2$ carbon centered radicals [236]. DFT calculations indicate that the carbon atom on the exocyclic double bond comes to lie closer to the Ag surface.

Our ability to directly visualize the bond geometry of the reaction products (Fig. 3.2, F to H) provides insight into the detailed thermal reaction mechanisms that convert **1** into the products. We limit our discussion to the reaction pathways leading from **1** to the two most abundant products, **2** and **3**. The reactivity of oligo-1,2-diethynylbenzene **1** can be rationalized by treating the 1,2-diethynylbenzene subunits as independent but overlapping enediyne systems that are either substituted by two phenyl rings for the central enediyne, or by one phenyl ring and one hydrogen atom in the terminal segments. This treatment suggests three potential cyclizations along the reaction pathway (resulting in six-, five-, or four-membered rings) [237], in addition to other possible isomerization processes such as [1,2]-radical shifts or bond rotations that have been observed in related systems [238]. Combinations of these processes leading to the products in a minimal number of steps were

From [173]. Reprinted with permission from AAAS.

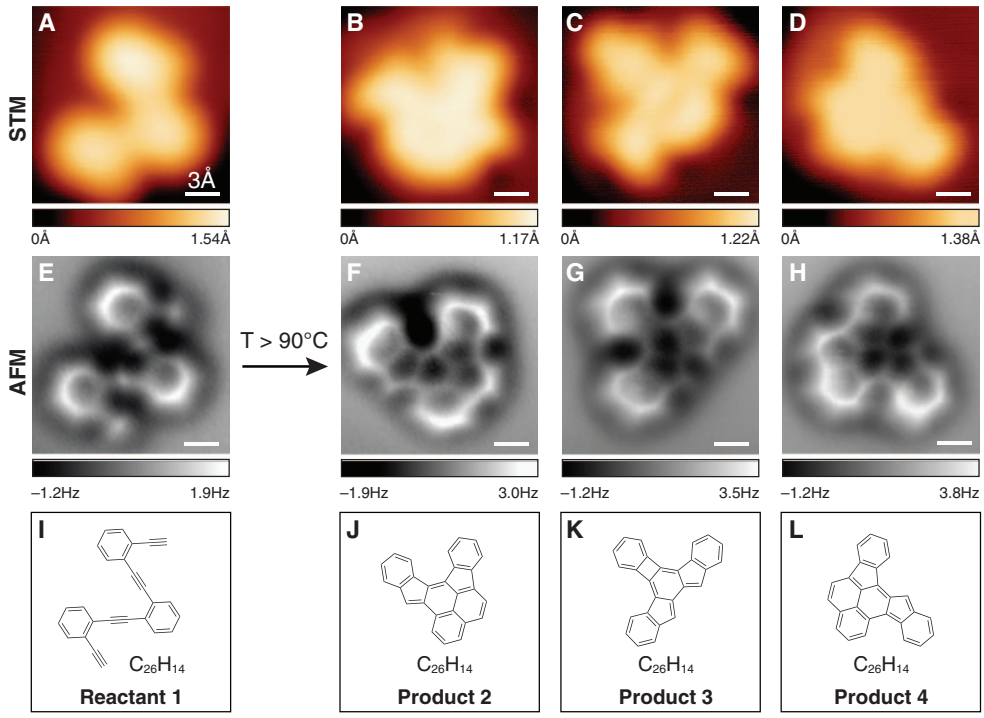


Figure 3.2: Comparison of STM images, nc-AFM images, and structures for molecular reactant and products. **(A)** STM image of **1** on Ag(100) before annealing. **(B to D)** STM images of individual products **2**, **3**, and **4** on Ag(100) after annealing at $T > 90\,^{\circ}\mathrm{C}$ ($I = 10$ pA, $V =$ -0.2 V, $T = 4$ K). **(E)** nc-AFM image of the same molecule (reactant **1**) depicted in (A). **(F to H)** nc-AFM images of the same molecules (products **2**, **3**, and **4**) depicted in (B) to (D). nc-AFM images were obtained at sample bias $V = -0.2$ V (qPlus sensor resonance frequency = 29.73 kHz, nominal spring constant = $1800\,\mathrm{N\,m^{-1}}$, Q-value = 90,000, oscillation amplitude = 60 pm). **(I to L)** Schematic representation of the molecular structure of reactant **1** and products **2**, **3**, and **4**. All images were acquired with a CO-modified tip.

explored and analyzed using DFT calculations.

We started by calculating the total energy of a single adsorbed molecule of the reactant **1** on a Ag(100) surface. Activation barriers and the energy of metastable intermediates were calculated (including molecule-surface interactions) for a variety of isomeric structures along the reaction pathway leading toward the products **2** and **3**. Our observations that the structure of reactants on Ag(100) remains unchanged for $T < 90\,^{\circ}\mathrm{C}$ and that no reaction intermediates can be detected among the products indicate that the initial enediyne cyclization is associated with a notable activation barrier that represents the rate-determining step in the reaction. In agreement with experiments, DFT calculations predict an initial high barrier for the first cyclization reactions, followed by a series of lower barriers associated with subsequent bond rotations and hydrogen shifts.

From [173]. Reprinted with permission from AAAS.

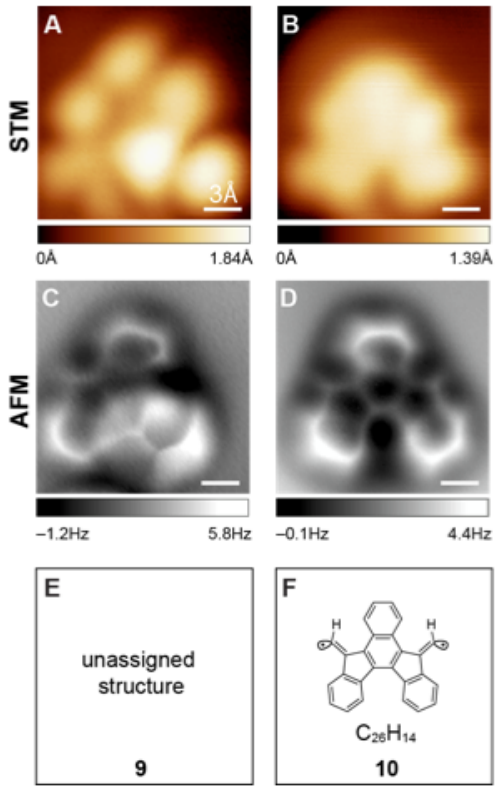


Figure 3.3: STM and nc-AFM images of other minority products on the surface after annealing. **(A to B)** STM images of **9** and **10**. Imaging parameters were ($I$ = 5 pA, $V$ = -0.066 V), and ($I$ = 10 pA, $V$ = -0.2 V), respectively. **(C to D)** Constant height frequency shift images of the same products, revealing the chemical structure in (D), but not clearly in (C). Imaging parameters: ($V$ = -0.25 V, amplitude = 60 pm), and ($V$ = -0.2 V, amplitude = 70 pm), respectively. qPlus sensor resonance frequency = 29.73 kHz, nominal spring constant = 1800 N m$^{-1}$, Q-value = 90000. **(E)** We cannot assign a unique structure to product 9 based on the qPlus image. **(F)** A schematic representation of the proposed molecular structure of **10**.

Figure 3.4A shows the reaction pathway determined for the transformation of **1** into product **2**. The rate-determining activation barrier is associated with a $C^1-C^6$ Bergman cyclization of a terminal enediyne coupled with a $C^1-C^5$ cyclization of the internal enediyne segment to give the intermediate diradical **Int1** in an overall exothermic process (-60.8 kcal mol$^{-1}$). Rotation of the third enediyne subunit around a double bond, followed by the $C^1-C^5$ cyclization of the fulvene radical with the remaining triple bond, leads to **Int2**. The rotation around the exocyclic double bond is hindered by the Ag surface and requires the breaking of the bond between the unsaturated valence on the sp$^2$ carbon atom and the Ag. Yet the activation barrier associated with this process does not exceed the energy of the starting material used as a reference. The formation of three new carbon-carbon bonds and the extended aromatic conjugation stabilize **Int2** by -123.9 kcal mol$^{-1}$ relative to **1**. Finally,

From [173]. Reprinted with permission from AAAS.

a sequence of radical [1,2]- and [1,3]-hydrogen shifts followed by a $C^1-C^6$ cyclization leads from **Int2** directly to the dibenzofulvalene **2**. Our calculations indicate that the substantial activation barriers generally associated with radical hydrogen shifts in the gas phase (50 to 60 kcal $mol^{-1}$) [239, 240] are lowered through the stabilizing effect of the Ag atoms on the surface, and thus they do not represent a rate-limiting process (Fig. 3.4A).

The reaction sequence toward **3** is illustrated in Fig. 3.4B. The rate-determining first step involves two $C^1-C^5$ cyclizations of the sterically less hindered terminal enediynes to yield benzofulvene diradicals. The radicals localized on the exocyclic double bonds subsequently recombine in a formal $C^1-C^4$ cyclization to yield the four-membered ring in the transient intermediate **tInt1**. This process involves the formation of three new carbon-carbon bonds, yet it lacks the aromatic stabilization associated with the formation of the naphthyl fragment in **Int2** and is consequently less exothermic (-60.7 kcal $mol^{-1}$). A sequence of bond rotations transforms **tInt1** via **Int3** into **tInt2**. Alignment of the unsaturated carbon valences in diradical **tInt1** with underlying Ag atoms maximizes the interaction with the substrate and induces a highly non-planar arrangement, thereby making subsequent rotations essentially barrierless. [1,2]-Hydrogen shifts and a formal $C^1-C^6$ cyclization yield the biphenylene **3**.

Both reaction pathways toward **2** and **3** involve $C^1-C^5$ enediyne cyclizations. These are generally energetically less favorable relative to the preferred $C^1-C^6$ Bergman cyclizations [237], but factors such as the steric congestion induced by substituents on the alkynes [231, 237], the presence of metal catalysts [241], or single-electron reductions of enediynes [242, 243] have been shown to sway the balance toward $C^1-C^5$ cyclizations yielding benzofulvene diradicals. All three of these factors apply to the present case of the thermally induced cyclization of **1** on Ag(100) (e.g., bulky phenyl substituent on $C^1$ and $C^6$, a metallic substrate, and a charge transfer of 0.5 electrons from the substrate to **1**), thus facilitating the $C^1-C^5$ cyclizations. The precise order of the low-energy processes (such as the **Int3**-**tInt2** rotation and the **tInt2**-**3** [1,2]-hydrogen shifts) following the rate-limiting initial cyclizations cannot be strictly determined experimentally. However, the sequence does not change the overall reaction kinetics and thermodynamics discussed above. Our bond-resolved single-molecule imaging thus allows us to extract an exhaustive picture and unparalleled insight into the chemistry involved in complex enediyne cyclization cascades on Ag(100) surfaces. This detailed mechanistic understanding in turn guides the design of precursors for the rational synthesis of functional surface-supported molecular architectures.

From [173]. Reprinted with permission from AAAS.

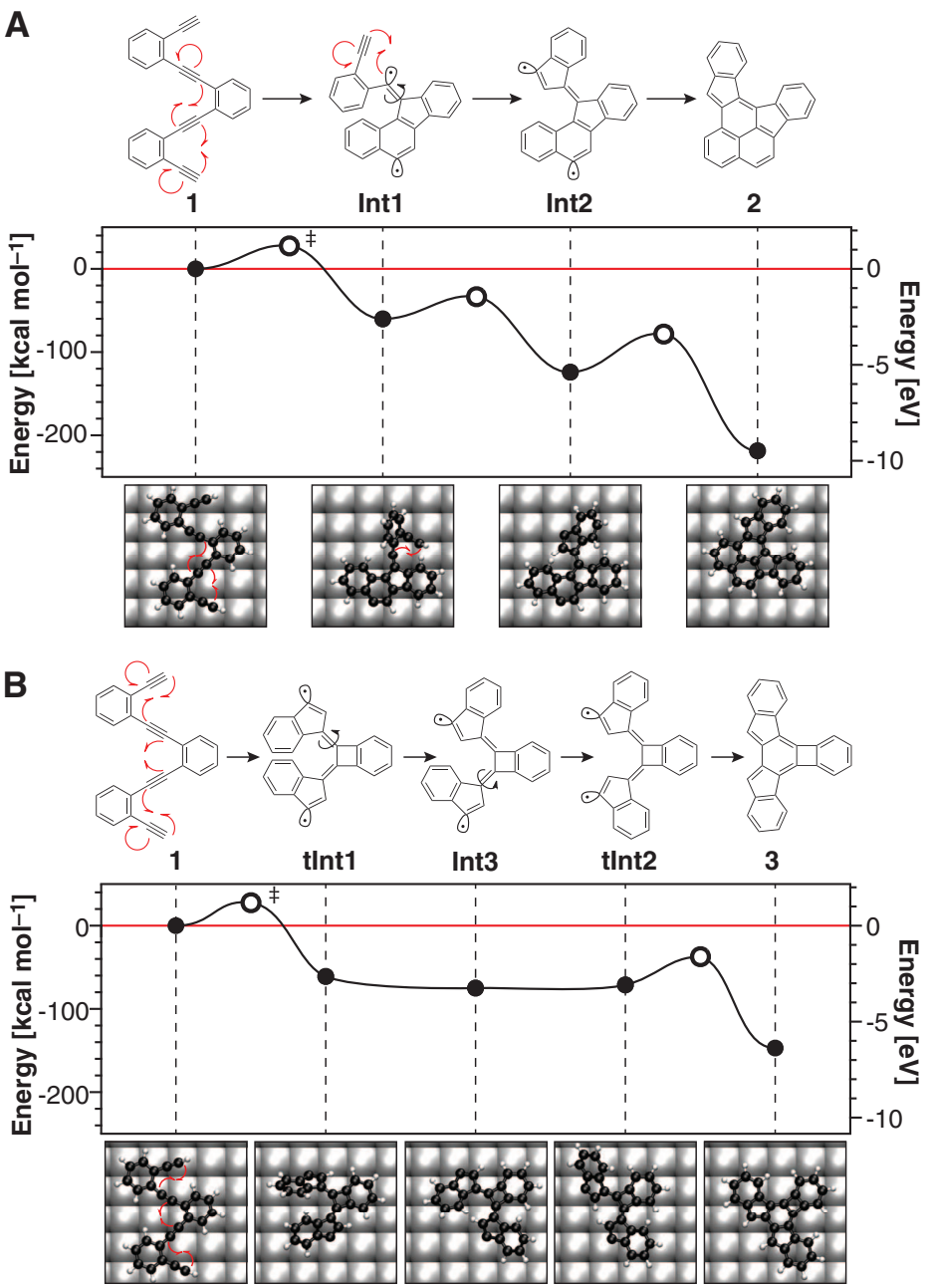


Figure 3.4: Reaction pathways and their associated energies as calculated by DFT. **(A)** Proposed pathway for the cyclization of reactant **1** into product **2** on Ag(100). **(B)** Proposed pathway for the cyclization of reactant **1** into product **3** on Ag(100). Energies for **1**, **2**, and **3** (end point solid circles), for the intermediates **Int1**, **Int2**, **Int3**, **tInt1**, and **tInt2** (intermediate solid circles), and for the reaction barriers (open circles) were calculated using *ab initio* DFT theory. Ball-and-stick models show the nonplanar structure of intermediates. The symbol ‡ indicates the rate-determining transition state; the red line is the reference energy of **1** on Ag(100).[a]

[a]From [173]. Reprinted with permission from AAAS.

## 3.2 Chemical reaction intermediates for enediyne cyclizations on Ag(100)

In the previous section we reported the identification of final reaction products on surfaces with individual-bond resolved qPlus imaging. Unfortunately, we never observed intermediates to provide further proof of our suggested reaction pathways. Additionally we did not observe any intermolecular coupling, which is an important ingredient for creating devices and extended carbon nanostructures for molecular electronics. In contrast, both of these features were observed when doing similar experiments with a different molecule: 1,2-bis(2-ethynylphenyl)ethyne (**1**, beginning a new numbering scheme, because the molecules from section 3.1 will not appear again in this dissertation).

### 3.2.1 Methods

We deposited the molecular precursor **1** from a Knudsen cell onto Ag(100) while holding the substrate at room temperature. We then imaged the surface using qPlus AFM at $T = 4\,\mathrm{K}$ with CO-modified tips, achieving individual-bond resolution. Then we annealed the substrate for 15 minutes in order to thermally induce reactions, and cooled it back down to $T = 4\,\mathrm{K}$ for imaging. This was done multiple times at various temperatures to "freeze in" intermediates of the chemical reactions.

### 3.2.2 Results

After deposition of **1**, but before annealing the surface, the molecules existed as two different conformational isomers on the surface (Fig. 3.5a,b). These isomers, a $C_{2h}$ symmetric trans-conformation and a $C_{2v}$ symmetric cis-conformation, are expected to occur because of rotations around the central single bonds [174]. As seen previously [173], we observed regions of increased imaging intensity, which correspond to the locations of the triple bonds within the molecules. After a high temperature annealing step we observed that the molecules transformed into many different structures (Fig. 3.5c). Various different monomer structures can be seen in Fig. 3.5c, including one of the unreacted precursors **1**. We also observed a number of different dimers that formed due to intermolecular coupling.

In an effort to better understand the reaction pathways leading to intermolecular coupling, we took high resolution qPlus AFM images of various dimeric structures. We observed 3 different dimer structures: (i) Dimers in which both of the two building blocks had not cyclized and were essentially the same as **1**, but coupled together at their alkyne groups. (ii) Dimers in which one of the two building block molecules had essentially the same chemical structure as **1**, without any cyclization, while the other building block had the same fully cyclized structures we observed for reacted monomers on the surface. (iii) Dimers in which both building blocks had undergone full cyclization.

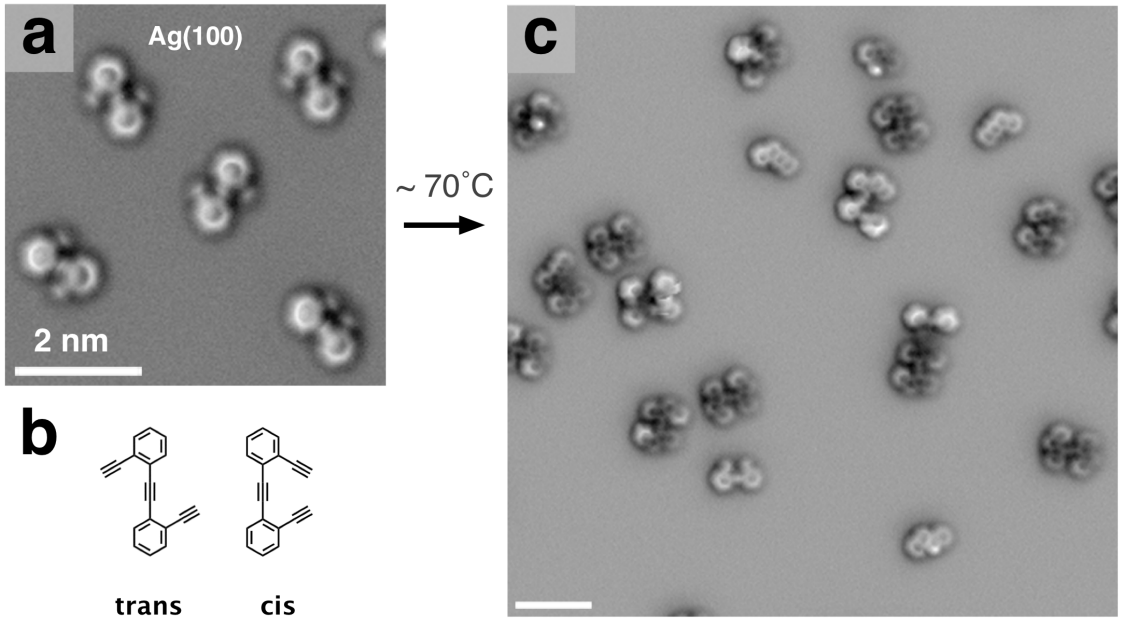


Figure 3.5: Overview of molecular adsorbates before and after annealing. **(a)** Constant height qPlus frequency shift image of the precursor **1** on Ag(100) as deposited. The precursor exists as two conformational isomers. Areas of increased frequency shift intensity within bonds of the molecules correspond to the locations of the triple bonds, which have higher electron density. **(b)** The two conformational isomers of **1** on the surface: a $C_{2h}$ symmetric trans-conformation and a $C_{2v}$ symmetric cis-conformation. **(c)** Constant height frequency shift image of the surface after annealing at $\sim$ 70 °C. A number of different monomer structures, including an unreacted cis precursor can be observed. Additionally different types of dimers are visible, resulting from intermolecular bonding.

In order to elucidate the reaction mechanisms involved in creating these three different types of dimers we performed systematic measurements during a series of annealing steps followed by low-temperature imaging. At each annealing step we increased the temperature compared to the previous step, ranging from $\sim$ 40 °C to $\sim$ 70 °C. In this way we were able to "freeze in" the intermediates of the reactions by supplying just enough thermal energy for intermediate structures to form but not enough to form the final products.

Various observed intermediate structures are shown in Fig. 3.6, together with the proposed reaction pathways in which they participate. Statistics taken from the experiments described above show that the structures in the early parts of the proposed pathways in Fig. 3.6 are mostly present for lower temperature annealing steps, while the later structures are mostly present after higher temperature annealing steps. This supports our hypothesis that these structures represent intermediates of these two reaction pathways.

Here is a description of the proposed pathways: The proposed pathway in Fig. 3.6a leads from precursor **1** to final product **5**. The pathway begins with coupling a trans and cis isomer of the precursor molecules **1** along their alkyne groups without any of the two building blocks undergoing cyclizations (**2**). Then one of the trans or cis building blocks

undergoes a series of cyclization steps resulting in new five- and six-membered rings (**3** or **3a**). This is followed by a cyclization of the other building block (**4**). Finally, two pairs of hydrogens dissociate to form the two red bonds in **5** in a cyclodehydrogenation step.

The proposed pathway in Fig. 3.6b is similar to the one above, but in this case the molecules initially couple together along the other combination of alkynes and we did not observe any cyclodehydrogenation step along this pathway. After the precursor couples without cyclization along the other alkyne groups (**6**), one of the building blocks cyclizes to form new five- and six-membered rings (**7**) . Finally the other building block fully cyclizes to form **8**.

To conclude this section on intermediates, we have shown that **1** adsorbed onto Ag(100) reacts to form cyclized and coupled dimers when heated. qPlus imaging with individual-bond resolution was used to uniquely identify the products and possible intermediates of reaction pathways by freezing them in after individual annealing steps followed by cooling to low temperatures for imaging. qPlus images of a number of these intermediates has allowed us to propose specific reaction pathways for the dimer formation. Further theoretical calculations are needed to confirm the intermediate hypothesis and elucidate the energetics of these processes.

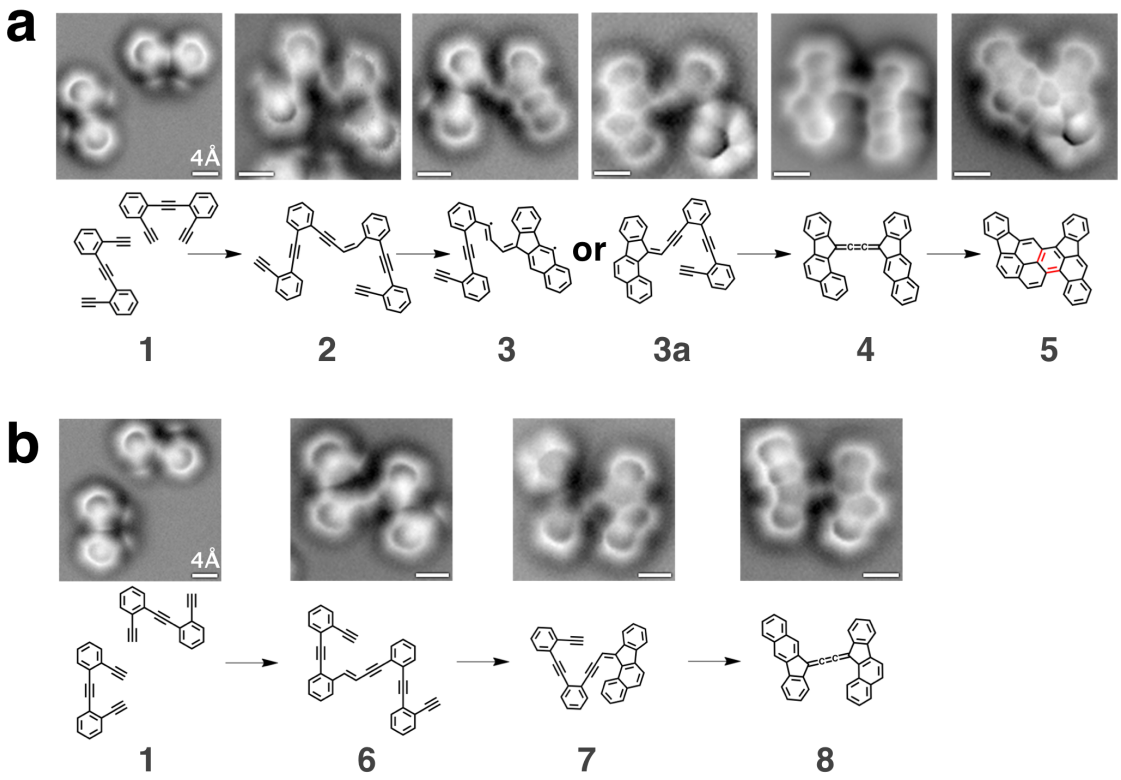


Figure 3.6: Two reaction pathways implied by the observed intermediates. **(a)** Constant height frequency shift image of various intermediates found on the surface after consecutive annealing steps with increasing temperatures and the corresponding hypothesized chemical structures and reaction pathway. The structures early in the pathway were most prevalent after annealing at lower temperature while the later structures were most prevalent at higher temperatures. The lower alkyne group in structure **3a** is not visible in the image, which we believe is due to tilting of the alkyne towards the Ag(100) surface. This results in less contrast for our constant height image. It also explains the enhanced contrast on the connected ring, due to tilting towards the tip. **(b)** Constant height frequency shift images showing various intermediates along a proposed second pathway. In structure **7** we observe a similar lack of contrast for the alkyne as in **3a**, which we interpret again as tilting of the alkyne towards Ag(100).

## 3.3 Chemical and electronic structure of polyacetylene derivatives on Au(111)

This section was originally published in **Nano Letters** [174].

Semiconducting $\pi$-conjugated polymers have attracted significant interest for applications in light-emitting diodes, field-effect transistors, photovoltaics, and nonlinear optoelectronic devices. Central to the success of these functional organic materials is the facile tunability of their electrical, optical, and magnetic properties along with easy processability and the outstanding mechanical properties associated with polymeric structures. In this work we characterize the chemical and electronic structure of individual chains of oligo-(E)-1,1′-bi(indenylidene), a polyacetylene derivative that we have obtained through cooperative C1−C5 thermal enediyne cyclizations on Au(111) surfaces followed by a step-growth polymerization of the (E)-1,1′-bi(indenylidene) diradical intermediates. We have determined the combined structural and electronic properties of this class of oligomers by characterizing the atomically precise chemical structure of individual monomer building blocks and oligomer chains (via noncontact atomic force microscopy (nc-AFM)), as well as by imaging their localized and extended molecular orbitals (via scanning tunneling microscopy and spectroscopy (STM/STS)). Our combined structural and electronic measurements reveal that the energy associated with extended $\pi$-conjugated states in these oligomers is significantly lower than the energy of the corresponding localized monomer orbitals, consistent with theoretical predictions.

Conjugated polymers have attracted considerable interest into their fundamental properties as well as their potential for industrial applications [244–246]. Their tunable electronic structure makes them a useful material for applications in the fields of molecular electronics and photonics [247–249]. Numerous chemical reactions yielding conjugated polymers have been adapted for the synthesis of well-defined molecular wires on surfaces [4, 12, 13, 17, 29, 30, 34, 37, 250–252]. These reactions include Ullmann-type cross-coupling [12, 13, 17], diyne polymerization [29, 252], and alkyne homocoupling [30], most of which require catalytically active metal substrates to facilitate polymerization. Thermally induced enediyne cyclization on surfaces [40, 173], a newer polymerization technique, has received increased attention due to its greater flexibility regarding noncatalytic growth substrates [220]. Effective utilization of carbon-based nanostructures resulting from these reactions requires the development of synthetic tools to control the chemical and electronic structure of the polymer products. Of particular importance for advanced electronics applications [253] is the formation of polymeric structures featuring extended $\pi$-conjugation during the growth process from small-molecule building blocks [254, 255].

Here we report the synthesis and characterization of individual chains of oligo-(E)-1,1′-bi(indenylidene) [256] obtained through thermally induced cooperative C1−C5 radical cyclizations of enediyne precursors followed by step-growth polymerization on Au(111). We have gained new insight into the relationship between the chemical structure and electronic

properties in these oligomers by utilizing nc-AFM to determine the precise atomic-scale structure of the enediyne starting material, cyclized monomers, and covalently linked oligomeric chains, while simultaneously utilizing STM/STS measurements to probe the localized and extended electronic states of these species (including orbital energies). These measurements help us to understand the oligomer formation reaction mechanism and show that the development of oligomer extended electronic states can be rationalized as the result of an efficient $\pi$-orbital overlap between monomer building blocks. Increased spatial delocalization is associated with a decrease in oligomer electronic energy, as confirmed by our theoretical simulations.

### 3.3.1 Methods

The enediyne precursor 1,2-bis(2-ethynylphenyl)ethyne (**1**, with a new numbering scheme) (Figure 3.7) used in this study was synthesized through iterative Sonogashira cross-coupling reactions. **1** was deposited in ultrahigh vacuum onto a Au(111) surface held at room temperature ($T = 293\,\mathrm{K}$). Cryogenic nc-AFM measurements ($T = 4\,\mathrm{K}$) (Figure 3.7a) reveal that **1** adopts two conformational isomers on the surface: a $C_{2h}$ symmetric trans-conformation (Figure 3.7b) and a $C_{2v}$ symmetric cis-conformation (Figure 3.7c). The atomic structure of the phenyl rings and the positions of the single and triple bonds are clearly resolved in the nc-AFM image. Contrast in nc-AFM measurements at the small oscillation amplitudes used here (60 pm) is dominated by short-range chemical forces that arise from repulsive interactions between the CO functionalized AFM tip and molecular adsorbates on the surface [172, 197]. This imaging technique allows precise spatial resolution of surface-bound atoms and bonds at a level that is not attainable by other surface probes [172, 173, 227], as indicated by comparison of the nc-AFM image in Figure 3.7a to the wire-frame structures in Figure 3.7b,c.

### 3.3.2 Results

Thermal annealing of the Au(111) surface decorated with a submonolayer coverage of **1** at 160 °C induces two intramolecular C1−C5 radical cyclization reactions (Figure 3.7d) as well as intermolecular carbon-carbon coupling reactions between monomer units. Following this annealing step more than 70% of the material on the surface becomes part of covalently linked molecular assemblies with lengths $n > 3$ (where n denotes the number of monomer subunits). As depicted in the nc-AFM image of Figure 3.10a, the most common structures observed are covalently linked oligo-(E)-1,1′-bi-(indenylidene) chains (an oligo-acetylene derivative) containing the common monomer subunit **2** (Figure 3.10b, dashed box). Most chains are composed of 5-10 monomer units, but sometimes exceed 20. Defect-free translational symmetry along the oligomer backbones is typically retained over segments of three to five monomers. While **2** (Figure 3.10b, dashed box) is representative of the dominant monomer incorporated into extended oligomer chains, other monomer subunits were also observed within the chains.

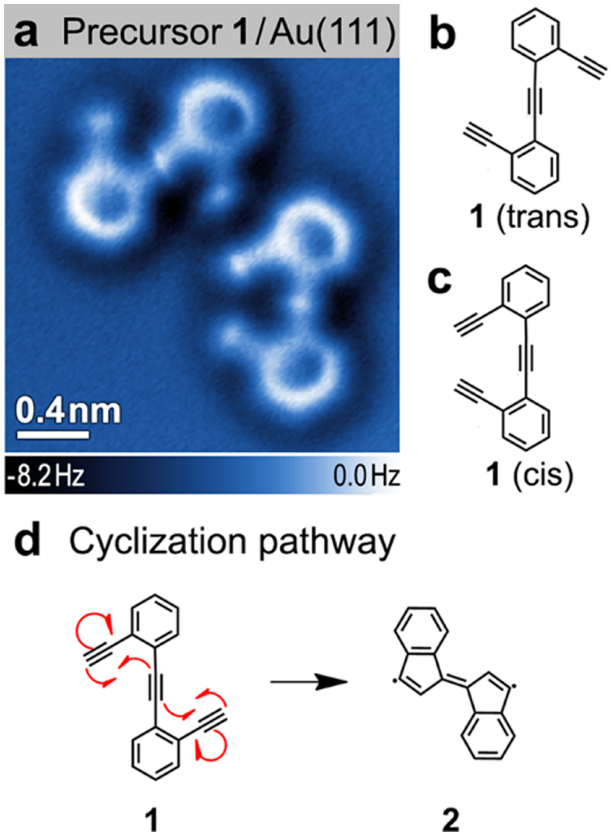


Figure 3.7: Precursor molecule **1**. **(a)** nc-AFM image of the two conformational isomers of **1** on Au(111) ($T = 4\,\mathrm{K}$; tip height corresponds to tunnel current set point $V_s = 50$ mV and $I = 10$ pA above Au(111)). **(b)** Schematic representation of trans conformation and **(c)** cis conformation. **(d)** Cyclization reaction: The precursor **1** can transform to the monomer **2** via two C1−C5 thermal enediyne cyclizations.

After deposition, the precursors aligned along the direction of the herringbone reconstruction (Figure 3.8a). After thermal annealing we observed a number of different structures including dimers and oligomers of various lengths. From the STM images alone we could not be certain that we succeeded in synthesizing polyacetylene derivatives, because STM is only sensitive to the spatially large orbitals near the Fermi energy (see chapter 2).

Therefore we performed qPlus imaging with sub-molecular resolution to reveal the precise chemical structure of the on-surface synthesized oligomers (Fig. 3.9). We observed various different subunits within the chains. The ends of the oligomers are often made up of various uncommon molecular structures. Within the chains the most common structure was **2** (Fig. 3.7d), which forms poly-acetylene derivatives when coupled together as in Fig. 3.9. Sometimes uncyclized monomers **1** are still found within oligomers.

A more detailed examination of qPlus imaging of the atomic structure of the oligomer chains (Figure 3.10a) reveals that the $\pi$-conjugated carbon-carbon double bonds along the backbone exhibit alternating lengths. Even though the symmetry of their local chemical

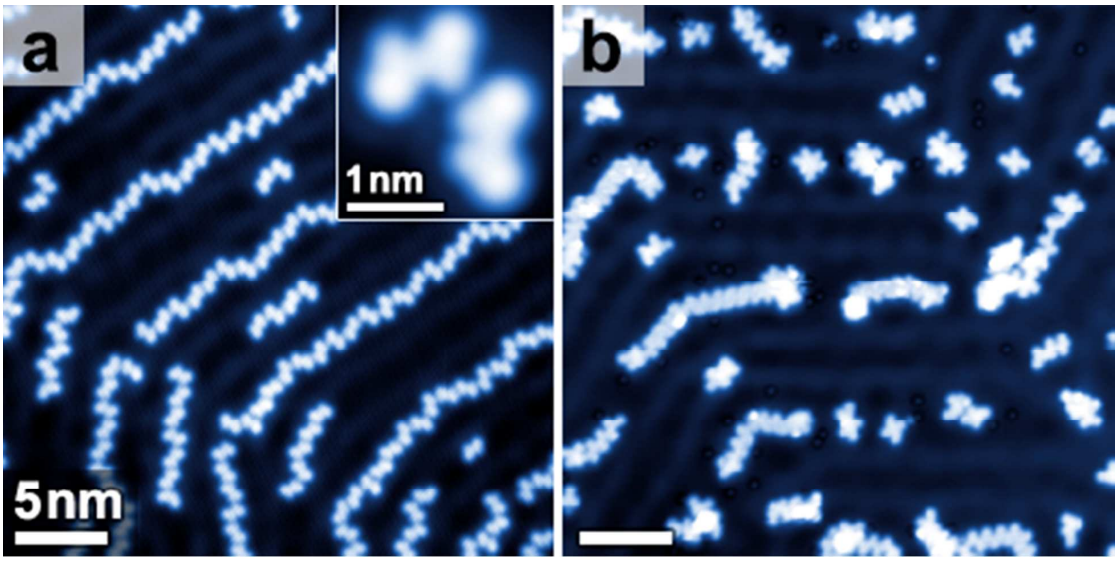


Figure 3.8: Overview of molecules on Au(111) before and after annealing. **(a)** STM image of precursor molecules (**1**) adsorbed onto Au(111) before annealing. The herringbone reconstruction of Au(111) leads to a one-dimensional arrangement of the molecules ($V_s$ = 50 mV, $I$ = 50 pA). The inset in (a) shows a close-up image of the precursor molecules (upper left is trans, lower right is cis; $V_s$ = 50 mV, $I$ = 10 pA). **(b)** STM image of the surface after annealing precursor molecules on Au(111) to 160 °C for 5 minutes shows the formation of oligomer chains and shorter molecular adducts ($V_s$ = 50 mV, $I$ = 10 pA).

structure is equivalent, bonds between the five-membered rings of adjacent indenyl groups alternate in length and are marked by red arrows (short bonds) and green arrows (long bonds) in the image. A schematic representation of the alternating pattern of short (C=C) and long (C-C) carbon-carbon bonds along the conjugated backbone is depicted in Figure 3.10b. The shorter (double) bonds between indenyl groups appear to be roughly 50% of the length of the longer (single) bonds for the tip-sample distance used to obtain the image in Figure 3.10a.

Figure 3.11 shows a Laplace filtered image of Figure 3.10a that sharpens features of the image and demonstrates our bond length measurement procedure. The bond lengths are measured between neighboring dashed yellow lines and show a clear alternation in apparent length. As expected, this apparent bond length variation becomes less pronounced with increasing tip height (not shown). It is important to note that while our nc-AFM measurement correctly identifies alternating trends in bond lengths, the magnitude of this effect is greatly exaggerated by this imaging technique [227]. Bonds within the five-membered rings are also seen to exhibit a bond length modulation. In particular, the double bonds in indenyl end-groups show a distinctive deviation compared to indenyl groups along the extended oligomer chain (Figure 3.10a, 3.11).

Our STM spectroscopy of oligo-(E)-1,1′-bi(indenylidene) reveals that the electronic structure of the covalently linked oligomer chains exhibits extended-state behavior (Figure 3.12).

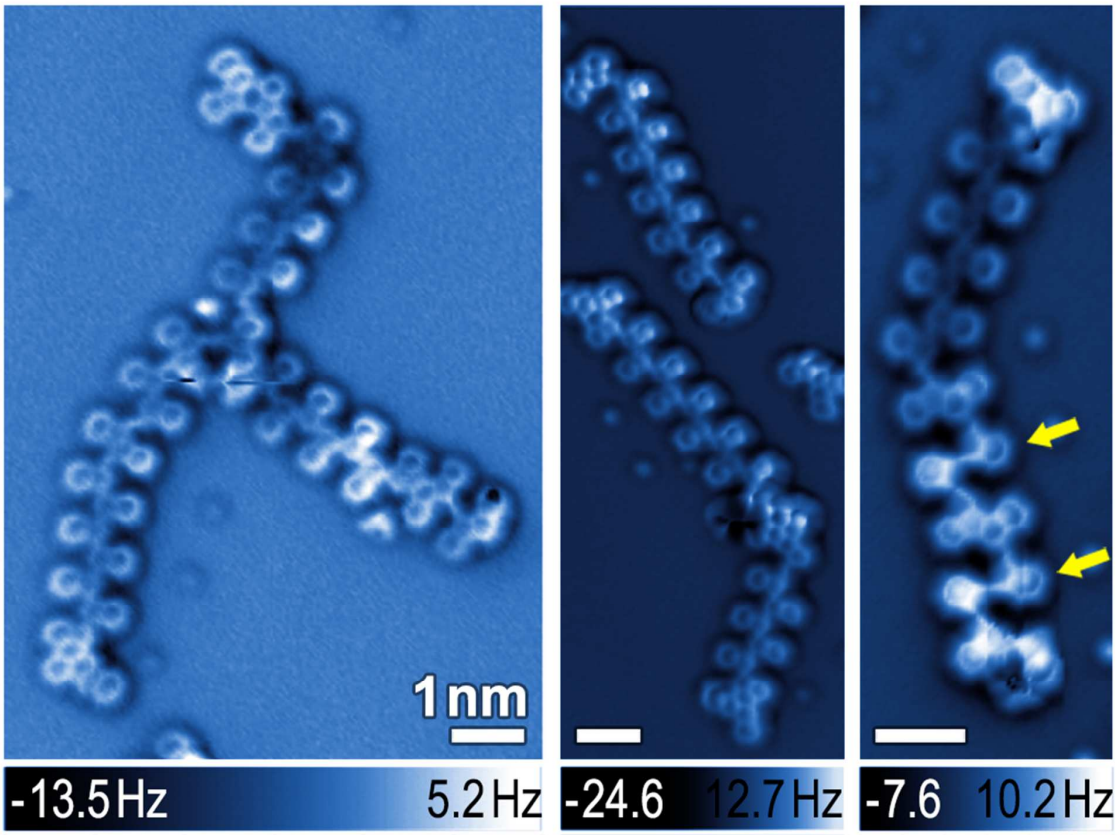


Figure 3.9: nc-AFM images of oligomer chains on Au(111) ($T = 4\,\mathrm{K}$) formed after thermally-induced reactions of the precursor molecule **1**. Oligomers of different length are found, as well as other short species. Yellow arrows mark uncyclized molecules (**1**) observed within an oligomer chain.

An AFM image of a representative oligomer chain on the Au(111) surface is depicted in Figure 3.12a along with the STM $\mathrm{d}I/\mathrm{d}V$ spectrum (Figure 3.12d) measured at one point along the backbone of the oligomer chain ($\mathrm{d}I/\mathrm{d}V$ measurement reflects the electronic local density of states (LDOS) at the energy selected by the sample bias; spectra taken at different points on the oligomer differ only in the intensity of the observed resonance). A well-defined electronic resonance is observed at an energy approximately 0.125 V above $E_F$ (blue arrow) compared to the $\mathrm{d}I/\mathrm{d}V$ spectrum on bare Au(111). A $\mathrm{d}I/\mathrm{d}V$ spatial map of the oligomer chain at a tip bias of 0.125 V (Figure 3.12b) reveals that the intensity of this state is localized along the oligomer backbone and extends continuously along the full length of the $\pi$-conjugated chain (excluding the ends, which are often composed of different types of monomer subunits).

This extended-state spatial distribution was observed for oligomer chains of different lengths composed of monomer units **2** (see Figure 3.13). In this figure we can see that the nodal pattern of the electronic state sometimes persists even in the presence of defects (cyclization reaction products, other than **2**). However, it is not present at locations within

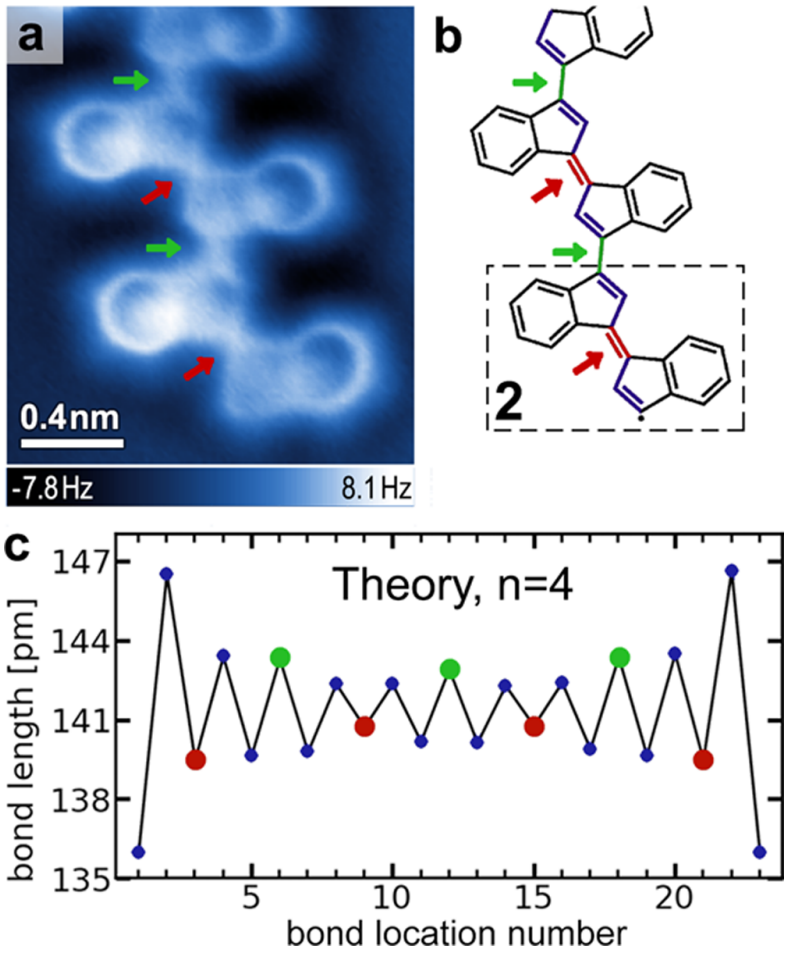


Figure 3.10: qPlus image of polyacetylene derivative. **(a)** nc-AFM image of an oligomer chain on Au(111) ($T = 4\,\mathrm{K}$; tip height corresponds to tunnel current set point $V_s = 50$ mV and $I = 30\,\mathrm{pA}$ above Au(111)). **(b)** Schematic representation of chemical structure of the oligomer in (a). Arrows indicate short (red) and long (green) bonds between indenyl groups. The dashed box shows monomer structure **2**. **(c)** DFT calculated bond lengths for a four-unit oligomer chain (composed of units of **2** as seen in (b) as a function of the location of the bond along the chain. Red and green dots indicate short and long bonds between indenyl groups, while blue dots indicate bonds within the five-membered rings (calculation shown for an oligomer chain having unsaturated radical valences at the chain ends; results are similar for hydrogen-terminated chains).

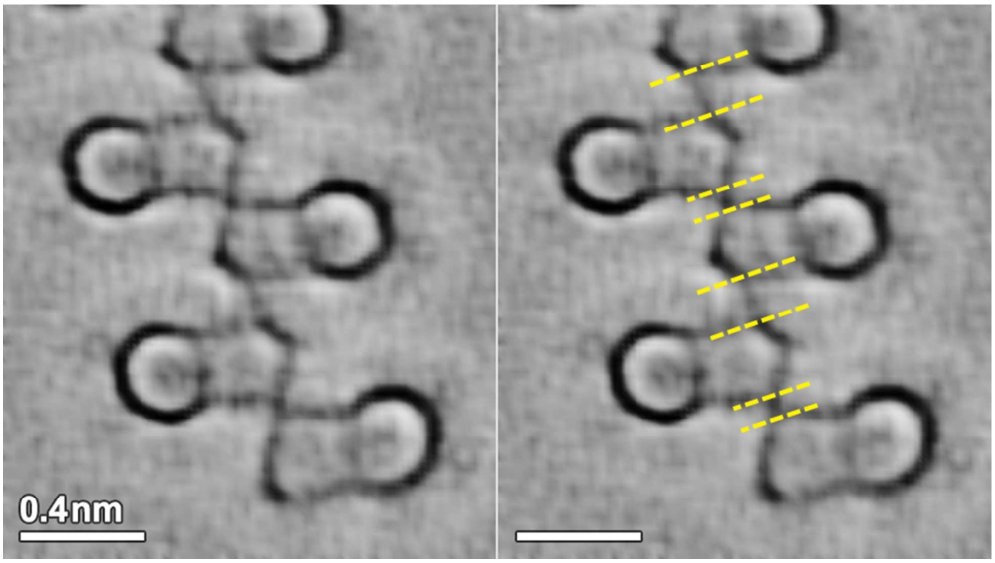


Figure 3.11: Laplace-filtered nc-AFM images of oligomer chains showing a carbon-carbon bond length ratio of ∼50% between indenyl groups. The Length of a carbon-carbon bond connecting two indenyl groups is measured as the distance between the corners of two connected five-membered rings (dashed yellow lines). A range of bond length ratios between indenyl groups was observed in our measurements (from 30% to 60%) for different tip heights spanning a range of 0.05 nm. This variation in bond length ratios can be explained by CO-tip/molecule interaction effects which become more pronounced at the lowest tip heights (as observed in previous work, see ref. [227]).

the oligomer that have a significant number of uncyclized monomers **1** (Fig. 3.13a,b,e,f).

Isolated monomer building blocks **2** not incorporated into oligomeric structures were observed to coexist with the chains on the Au(111) surface. These monomers account for a few percent of the material on the surface (other monomer structures have also been observed). Figure 3.14a depicts a nc-AFM image of an isolated (E)-1,1′-bi(indenylidene) monomer. Isolated monomer building blocks **2** exhibit a geometry that resembles the indenyl end-groups in oligomer chains (Figure 3.10a, bottom), including the presence of highly distorted five-membered rings (such distortion might arise due to the interaction of a radical with the surface [257]). The electronic structure of bi(indenylidene) monomers **2** was characterized by STM spectroscopy. A representative $\mathrm{d}I/\mathrm{d}V$ spectrum measured on an isolated (E)-1,1′-bi(indenylidene) monomer and the corresponding spectrum of the bare Au(111) surface are depicted in Figure 3.14d (spectra taken at different points on the monomer differ only in the intensity of the observed resonance). A prominent resonance at $V_s = 1.2$ V (blue arrow) marks the lowest unoccupied molecular orbital (LUMO) of the molecule adsorbed onto the Au(111) surface. The spatial distribution of this molecular electronic state was imaged using $\mathrm{d}I/\mathrm{d}V$ mapping (Figure 3.14b).

The combination of nc-AFM and STM spectroscopy measurements on individual oligomer chains and small molecule precursors reveals both the underlying reaction mechanism that

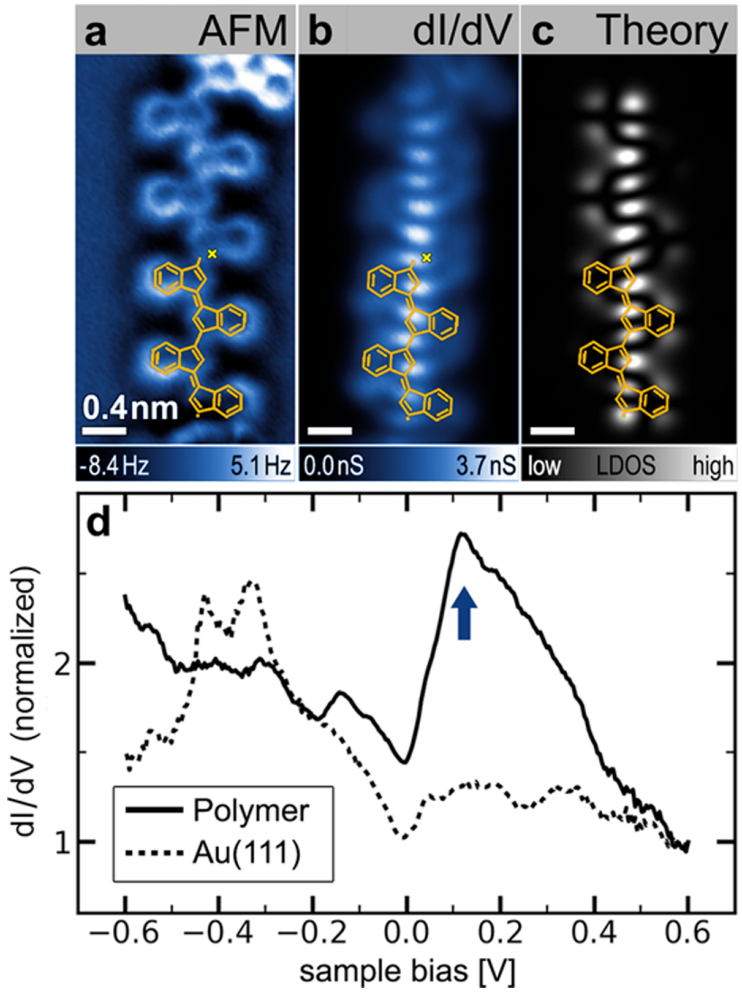


Figure 3.12: Electronic structure of an individual oligomer. **(a)** nc-AFM image of oligomer chain (tip height corresponds to tunnel current set point $V_s = 50$ mV and $I = 20$ pA above Au(111)). **(b)** Experimental STM $\mathrm{d}I/\mathrm{d}V$ map (constant height) at $V_s = 0.125$ V reveals an extended electronic state along the conjugated backbone of oligomer shown in (a). **(c)** GW calculation of electronic local density of states of the LUMO for a free-standing oligomer chain containing four monomer **2** subunits (n = 4). Orange overlays in (a)-(c) show the chemical structure of two units of the n = 4 oligomer chain used in the calculation. **(d)** STM $\mathrm{d}I/\mathrm{d}V$ point spectroscopy of oligomer chain shown in (a) at the position indicated by the yellow cross reveals an electronic resonance at $V_s \approx 0.13$ V (blue arrow) compared to a reference spectrum on bare Au(111) (spectra are normalized by their respective values at $V_s = 0.6$ V, open feedback spectroscopy starting parameters $V_s = 0.6$ V, $I = 0.8$ nA, $T = 4$ K).

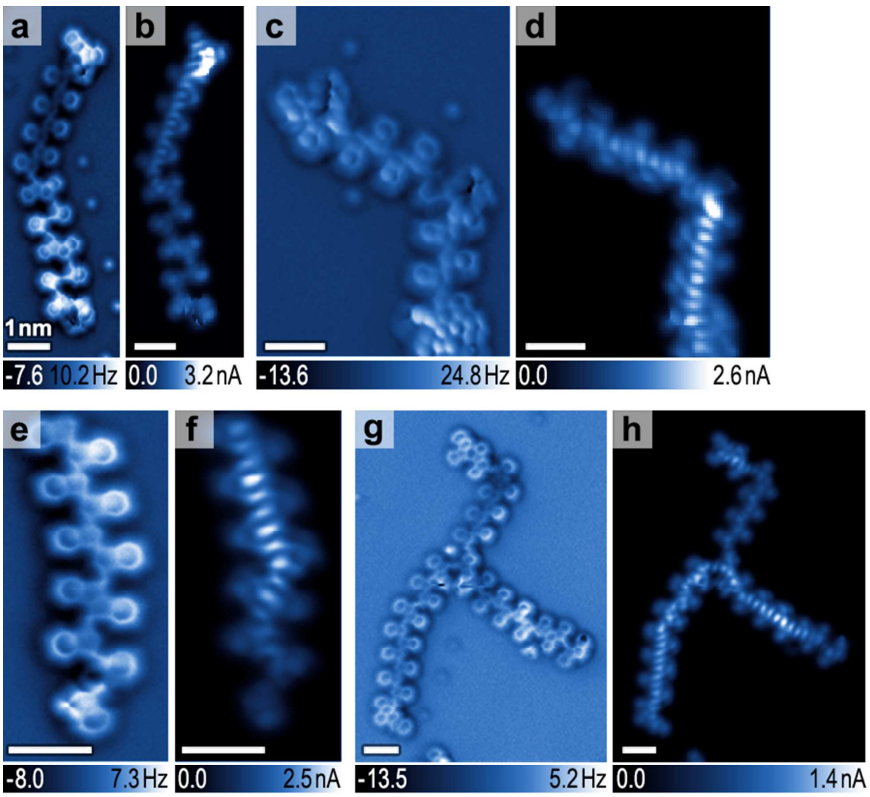


Figure 3.13: qPlus and STM measurements of oligomers of various lengths, showing an extended electronic state along the backbone. **(a,c,e,g)** nc-AFM images and **(b,d,f,h)** STM images of oligomer chains exhibiting sequences of the monomer building blocks (**2**) with different length ($V_s = 50$ mV, $T = 4$ K). The tunneling current images (b,d,f,h) show characteristics of the extended electronic state along the conjugated backbone of these different-length segments composed of monomer **2**.

leads to the formation of oligo-(E)-1,1′-bi(indenylidene), as well as the origin of the oligomer electronic structure. Two thermally induced intramolecular C1−C5 enediyne cyclizations of **1** yield the monomer building-block **2** that has been observed on the surface (Figure 3.14). This highly reactive 3,3′-diradical intermediate diffuses along the Au(111) surface and recombines with other monomers in a step-growth process. While theoretical models in the gas phase have reported an activation barrier of $\sim 40\,\mathrm{kcal\,mol^{-1}}$ for the C1−C5 cyclization of benzannulated enediynes [237], we have previously shown that metal surface-supported C1−C5 cyclizations can proceed at temperatures below 100 °C [173]. In some oligomer chains we have observed uncyclized precursor molecules **1** that are covalently linked via their terminal alkyne carbon atoms (Figure 3.9). We attribute this structural defect to the reaction of a radical at the end of the growing oligo-(E)-1,1′-bi(indenylidene) chain with a terminal alkyne carbon atom of an uncyclized building block **1**.

The electronic structure of the oligo-acetylene derivative oligo-(E)-1,1′-bi(indenylidene) can be understood as a consequence of spatial delocalization caused by extended conjugation

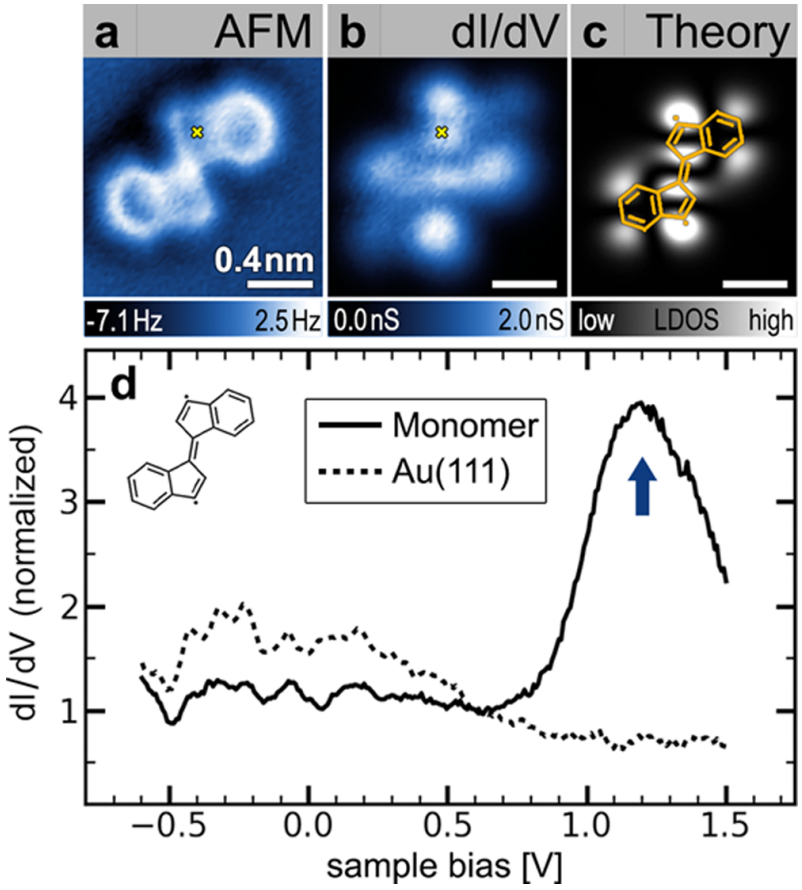


Figure 3.14: Electronic structure of isolated monomer building block **2**. **(a)** nc-AFM image of an isolated monomer **2** on Au(111) ($T = 4\,\mathrm{K}$, tip height corresponds to tunnel current set point $V_s = 50$ mV and $I = 35$ pA above Au(111)). **(b)** Experimental constant-height $\mathrm{d}I/\mathrm{d}V$ map of monomer **2** shown in a at $V_s = 1.2$ V depicts the spatial distribution of the monomer LUMO. **(c)** GW calculation of the local density of states of the LUMO for a free-standing monomer **2**. **(d)** STM $\mathrm{d}I/\mathrm{d}V$ point spectroscopy performed on the monomer shown in (a) at the position indicated by the yellow cross reveals the monomer LUMO at $V_s \simeq 1.2$ V (blue arrow) compared to a reference spectrum on bare Au(111) (spectra are normalized by their respective values at $V_s = 0.6$ V, open feedback spectroscopy starting parameters $V_s = 1.5$ V, $I = 0.5$ nA, $T = 4\,\mathrm{K}$).

of $\pi$-systems between monomer building blocks. While an individual monomer exhibits localized electronic states separated by a large energy gap, the efficient $\pi$-overlap between monomer orbitals in the oligomer chains results in the formation of lower energy extended states. This behavior is evident in the spectroscopic data in Figures 3.12 and 3.14, where the LUMO of an isolated monomer lies ∼1.1 eV higher in energy than the extended state (relative to $E_F$).

These conclusions were confirmed by GW calculations [258, 259] performed to model both an isolated monomer **2** and an n = 4 oligomer chain having the same structure indicated by the partial wireframe image (orange overlay) in Figure 3.12a-c. The calculated LDOS of the isolated monomer LUMO is depicted in Figure 3.14c. It closely resembles the experimental $\mathrm{d}I/\,\mathrm{d}V$ map (Figure 3.14b), with strong intensity arising from the 3- and 3′-positions in the (E)-1,1′-bi(indenylidene). When monomer subunits are joined in the $n = 4$ oligomer chain, GW calculations indicate the formation of an extended electronic state that is lower in energy by 1.0 ± 0.1 eV compared to the monomer LUMO, assuming typical physisorption distances of 0.33 ± 0.03 nm [260] (these values were obtained using an image-charge model of the surface combined with the GW calculation [261]). This state extends continuously along the oligomer backbone as depicted in the theoretical LDOS of Figure 3.12c. The energetic lowering and spatial extent of the calculated oligomer LDOS closely resembles the experimental data. The nodal pattern of the LUMO can also be qualitatively explained via a simple one-dimensional particle-in-a-box model whereby for an oligomer of length n (with 6n carbon atoms along the backbone) the 6n $\pi$-electrons fill the first 3n levels. The LUMO level, being the next highest level, thus exhibits 3n+1 antinodes.

The agreement between theory and experiment extends to the appearance of alternating bond lengths in the oligomer. Figure 3.10c shows that the calculated bond lengths along the conjugated backbone of an n = 4 oligomer chain alternate in the same pattern as observed experimentally for the C−C/C=C bond lengths between indenyl groups (green circles represent long bonds between indenyl groups, red circles represent short bonds between indenyl groups). In the calculation this behavior arises from a combination of Peierls distortion and boundary effects (since the boundary fixes the bond phase). As expected, there is a discrepancy between the nc-AFM experimental results and the theoretical calculations regarding the absolute magnitude of the bond-alternation effect. Whereas the AFM images (Figure 3.10a) largely exaggerate bond length variations (∼ 50%), the calculation predicts bond-to-bond variations of only ∼ 3%. This discrepancy does not arise from oligomer interaction with the substrate lattice, since similar bond variations are experimentally observed for oligomers lying along different substrate crystallographic directions. Also, artifacts caused by long-range forces [227] can be excluded because the respective bonds within the chains are in a symmetrically equivalent chemical environment, which leads to an equivalent van der Waals background. The anomalously large bond alternation observed experimentally is likely an image distortion caused by tilting of the CO molecule adsorbed onto the AFM tip. [227, 262]

In conclusion, we have grown 1D chains of the oligo-acetylene derivative oligo-(E)-1,1′-bi(indenylidene) on a surface through a thermally induced radical cyclization/step-growth polymerization process. Individual oligomer chains exhibit extended 1D electronic states

and alternating bond lengths. This radical polymerization process on surfaces provides a new route toward fully conjugated low-bandgap derivatives of all-trans polyacetylene.

## 3.4 Conclusion

We have shown how qPlus AFM can be used to study reaction products on surfaces at the single molecule level. We identified chemical reaction products of enediyne cyclization reactions on Ag(100), which would not be possible using only STM and DFT. This reaction did not lead to any intermolecular bonding, an important prerequisite for the on-surface synthesis of extended carbon nanostructures. A different enediyne molecule on Ag(100), however, did result in intermolecular bonding by reacting to form dimers. Additionally we were able to freeze in intermediates by taking measurements at low temperature between consecutive annealing steps. The sub-molecular-resolution images of the intermediates give us unprecedented insight into the precise reaction mechanism of on-surface reactions involving organic bond rearrangements. Because of the lack of extended carbon nanostructures beyond dimers we also induced reactions of the same enediyne molecules on a different surface, Au(111), which did lead to the formation of oligomers. With qPlus we confirmed that these oligomers were polyacetylene derivatives, belonging to an important class of conductive polymers. Using the combined STM/AFM we then correlated the electronic and chemical structure of these oligomers.

# Chapter 4

# Tuning single-molecule orbitals and charge states

Remotely controlling the orbital energies and charges states of molecules could lead to devices such as single-molecule transistors. This type of control has been shown before [44, 61], but it has not been demonstrated while using local probe techniques to image the local adsorption configuration and local electronic structure at the small length scales that are relevant for molecular electronics. In this chapter we report on our use of back-gated graphene to remotely and controllably tune the orbitals and charge states of adsorbed molecules while monitoring their electronic structure at the single molecule level.

Section 4.1 discusses our study on tuning the orbital energies of benzene-derived molecules adsorbed onto a graphene FET device [175]. After deposition, the molecules formed a well-ordered monolayer with hexagonal lattice on the low-corrugation graphene/BN substrate. STS measurements revealed a LUMO far from the Fermi level, with signatures of a coherent combination of electron and phonon states (vibronic states). We then applied a back-gate voltage, which shifted the graphene Fermi level and therefore the energies of the molecular orbitals with respect to the Fermi energy. This allowed us to switch between tunneling into the LUMO and LUMO+1 at the same bias voltage, depending on the applied gate voltage. However, we did not observe any changes in the charge states of these molecules.

Section 4.2 discusses our study on actually tuning the charge states of individual molecules. This study involved the strong acceptor F4-TCNQ adsorbed onto a graphene FET device. When deposited onto graphene, charge transfer from graphene to F4-TCNQ results in p-doping of graphene. Using our local probe techniques we are able to show that the charge states of molecules depend sensitively on the precise adsorption configuration and local environment of the molecules. By applying a back-gate to graphene we were able to control the charge state of single molecules, switching them controllably and reversibly between neutral and negatively charged. This level of control could lead to local probe studies of phenomena such as the Kondo effect on graphene [263] or atomic collapse with negative "nuclei" [264].

## 4.1 Imaging and tuning molecular levels at the surface of a gated graphene device

This section was originally published in **ACS Nano** [175].

Gate-controlled tuning of the charge carrier density in graphene devices provides new opportunities to control the behavior of molecular adsorbates. We have used scanning tunneling microscopy (STM) and spectroscopy (STS) to show how the vibronic electronic levels of 1,3,5-tris(2,2-dicyanovinyl)benzene molecules adsorbed onto a graphene/BN/SiO2 device can be tuned via application of a back-gate voltage. The molecules are observed to electronically decouple from the graphene layer, giving rise to well-resolved vibronic states in $\mathrm{d}I/\,\mathrm{d}V$ spectroscopy at the single-molecule level. Density functional theory (DFT) and many-body spectral function calculations show that these states arise from molecular orbitals coupled strongly to carbon-hydrogen rocking modes. Application of a back-gate voltage allows switching between different electronic states of the molecules for fixed sample bias.

Combining organic molecules with graphene creates new opportunities for fabricating hybrid devices with tailored properties. Previous experiments have shown that electronic [137, 139–155], magnetic [146, 159, 160] and optical [161–163] characteristics, as well as chemical reactivity [162, 265, 266] of graphene devices can be tuned through molecular adsorption. Such measurements have been performed primarily using electrical conductivity and optical spectroscopy techniques. These measurements, however, do not directly yield local microscopic information regarding the hybrid graphene/molecule interface. Additional electronic structure information on molecule/graphene systems in non-gated configurations has been provided by STM [152, 153, 156, 160, 165–170, 267] and photoemission spectroscopy [137, 139, 140, 152, 156–158] experiments, including measurement of the energy location of molecular orbitals. Such measurements, however, have so far precluded the hybrid molecule/graphene electronic structure from being electrostatically tuned through the use of a back-gate, and molecular vibronic properties in these systems remain poorly understood [167].

Here we describe a single-molecule-resolved STM study of a molecular monolayer adsorbed onto a back-gated graphene device that allows both characterization and gate-induced modification of molecular electronic properties. 1,3,5-Tris(2,2-dicyanovinyl)-benzene (CVB) molecules were adsorbed onto a graphene device in ultra-high vacuum (UHV) and studied via STM spectroscopy at cryogenic temperatures. Hybridized electronic levels of individual CVB molecules on graphene were imaged, and the electronic states were observed to exhibit unexpectedly strong vibronic satellites. The hybridized vibronic electronic structure of the CVB molecules rigidly shifted in energy as a voltage was applied to the device back-gate, thus allowing the electronic local density of states (LDOS) at fixed sample bias to be switched between different molecular orbitals. Identification of the experimentally observed molecular orbitals was facilitated via density functional theory (DFT)-based spectral function simula-

tions which accurately reproduce the orbital structure imaged by STM. These simulations also allow identification of the vibronic satellites through calculation of the CVB electron-phonon coupling. Although CVB molecules exhibit a broad spectrum of vibrational modes, only C-H rocking modes of the CVB molecules having an energy close to 200 meV are seen to contribute significantly to the molecule/graphene electron-phonon coupling. The energy of these modes is in good agreement with the energy spacing of vibronic satellites observed experimentally for CVB on graphene.

### 4.1.1 Methods

We used back-gated graphene/BN/SiO2 devices [133, 268, 269] similar to the one schematically depicted in Fig. 4.1a. The graphene sample was grown by the CVD method described in [270]. Hexagonal boron nitride flakes were exfoliated onto heavily doped silicon wafers coated in 285 nm thermal oxide. The graphene was transferred on top of the BN/SiO2 [269] using a polydimethylsiloxane (PDMS) stamp and electrical contact was made by depositing Ti (10 nm-thick)/Au (30 nm-thick) electrodes using a stencil mask technique. 1,3,5-Tris(2,2-dicyanovinyl)benzene (CVB) was synthesized through a Knoevenagel condensation of benzene-1,3,5-tricarboxaldehyde and malononitrile [271, 272]. The molecules were evaporated from a Knudsen cell onto the graphene device in UHV while the device was held at $T = 5\,\mathrm{K}$. The device was then briefly annealed at room temperature before being cooled back to 4 K. CVB was chosen for this experiment due to its extended $\pi$-system and the high electron affinity of its dicyanovinyl groups. STM/STS was performed using an Omicron LT STM at $T = 4\,\mathrm{K}$. STM differential conductance ($\mathrm{d}I/\,\mathrm{d}V$) was measured in constant-height mode (both for point spectroscopy and for spatial maps) by lock-in detection of the a.c. tunnel current generated by a 6 mV r.m.s. 316 Hz signal added to the sample bias.

DFT calculations were performed using an exchange-correlation functional that combines the PBE functional together with a semi-empirical dispersion correction to take into account van der Waals interaction between the molecules and graphene [273, 274]. We used a supercell containing one CVB molecule and 42 graphene atoms, with a lattice constant of 1.13 nm. The combined CVB and graphene system was allowed to relax in these simulations to its most stable configuration. Frequencies of vibrational modes and electron-phonon matrix elements were calculated in the framework of density functional perturbation theory (DFPT) [275] using the QUANTUM ESPRESSO package [276]. We performed GW [258, 277] corrections employing the BerkeleyGW package [259] to account for electron-electron correlations not captured in DFT. The molecular orbital energies were further corrected for electron-phonon interactions using the 1st order cumulant approximation.

### 4.1.2 Results

Fig. 4.1b-d show STM images of a monolayer-high self-assembled island of CVB molecules on graphene/BN. The Moiré pattern arising from interaction between the graphene lattice and the underlying BN lattice is clearly visible (Fig. 4.1b,c) even though the graphene is covered

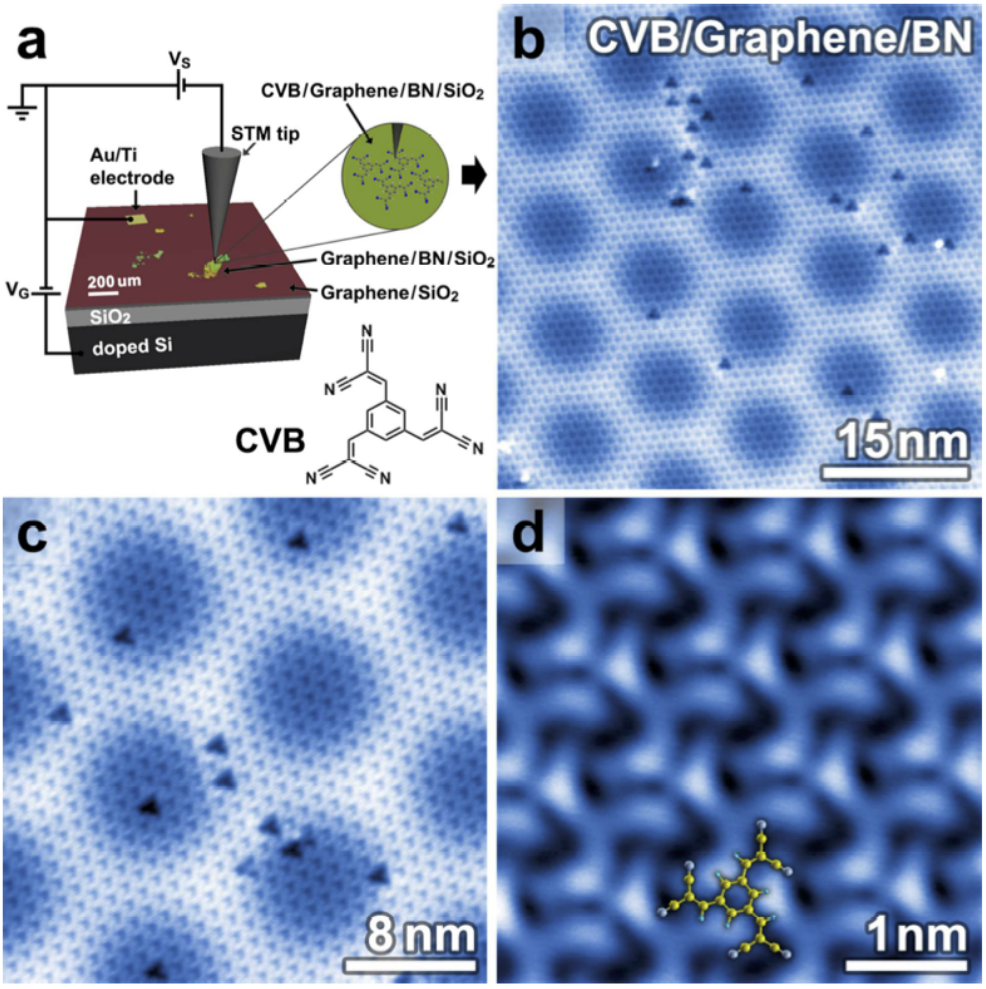


Figure 4.1: CVB molecules on a graphene/BN FET device. **(a)** Sketch of the back-gated graphene device used in these STM/STS measurements, as well as a model of the CVB molecule. **(b)-(d)** STM images of a monolayer of CVB molecules on graphene/BN show the hexagonal lattice of the CVB molecules at different zoom values ($V_S = 2.0\,\mathrm{V}$, $I_t = 10\,\mathrm{pA}$, $T = 4\,\mathrm{K}$). Isolated vacancies are observed in (b) and (c).

with a layer of molecules. The molecules form a hexagonal lattice with a lattice constant of $a = 1.13 \pm 0.01\,\mathrm{nm}$, and isolated defects having triangular shape can be observed. The close-up STM image in Fig. 4.1d shows a spiral-like electronic LDOS associated with the molecules (the opposite chirality was also observed in different islands). The presence of single-molecule vacancies (Fig. 4.1b,c) allows us to assign the location of CVB molecules in the film.

$\mathrm{d}I/\mathrm{d}V$ spectra were measured while holding the STM tip above the CVB monolayer. The spectra were essentially featureless over the range $-0.5\,\mathrm{V} < V_S < 1.6\,\mathrm{V}$, but for $V_S > 1.6\,\mathrm{V}$ clear resonance features were observed (Fig. 4.2a). For $V_S < -0.5\,\mathrm{V}$ the CVB molecules

tended to jump to the STM tip, and so reproducible STM spectra at sample voltages lower than $-0.5\,\mathrm{V}$ could not be obtained. The Dirac point of the underlying graphene substrate could be seen when the tip-height was lowered by $4\,\text{Å}$ relative to the typical $\mathrm{d}I/\,\mathrm{d}V$ measurement tip-height (Fig. 4.2a inset), but this usually led to CVB molecules jumping to the STM tip. The empty state spectrum for larger tip-heights, however, was quite stable up to nearly $3\,\mathrm{V}$, as seen in the spectrum of Fig. 4.2a (this spectrum was reproduced with numerous different tips and samples). Four pronounced peaks can be seen in the spectrum, labeled 1-4. A statistical analysis of our spectra (using Gaussian fits to the peaks) yields the following energy locations for the four peaks (where $E = |e|V_S$): $E_1 = 1.86 \pm 0.02\,\mathrm{eV}$, $E_2 = 2.06 \pm 0.02\,\mathrm{eV}$, $E_3 = 2.28 \pm 0.02\,\mathrm{eV}$, and $E_4 = 2.68 \pm 0.03\,\mathrm{eV}$. The energy differences between peaks 1-2 and peaks 2-3 are quite similar, whereas the energy difference between peaks 3-4 is twice as big: $E_2 - E_1 = 0.20 \pm 0.03\,\mathrm{eV}$, $E_3 - E_2 = 0.22 \pm 0.03\,\mathrm{eV}$ and $E_4 - E_3 = 0.4 \pm 0.04\,\mathrm{eV}$. $\mathrm{d}I/\,\mathrm{d}V$ maps taken at sample biases covering the range of the first three peaks ($1.85\,\mathrm{V} < V_S < 2.4\,\mathrm{V}$ ) show no significant differences in the spatial distribution of the electronic LDOS (Fig. 4.2b, first two panels). However, the $\mathrm{d}I/\,\mathrm{d}V$ map obtained at the energy of the fourth peak ($V_S = 2.65\,\mathrm{V}$) shows a significantly different spatial distribution of the electronic LDOS (Fig. 4.2b, third panel).

One of the unique aspects of this study is that we were able to perform STM spectroscopy and imaging while modifying the hybridized molecule/graphene electronic doping using an electrostatic back-gate. Fig. 4.3a shows $\mathrm{d}I/\,\mathrm{d}V$ spectra taken on a CVB monolayer island at two different back-gate voltages ($V_G$). The black trace shows the spectrum acquired at $V_G = 0\,\mathrm{V}$ while the red trace shows the spectrum taken at a gate voltage of $V_G = 60\,\mathrm{V}$. The red trace is rigidly shifted by $\sim 0.2\,\mathrm{V}$ toward lower sample bias, but does not exhibit any other significant changes in its features. We see a similar gate-dependent shift in the Dirac point energy via STM spectroscopy for these graphene devices without molecular layers [278], corresponding to a change in the carrier concentration from $n = 4 \times 10^{10}\,/\mathrm{cm}^2$ ($V_G = 0\,\mathrm{V}$) to $n = 4 \times 10^{12}\,/\mathrm{cm}^2$ ($V_G = 60\,\mathrm{V}$). We next acquired $\mathrm{d}I/\,\mathrm{d}V$ maps at a fixed sample bias of $V_S = 2.4\,\mathrm{V}$, but for different gate voltages $V_G$. The $\mathrm{d}I/\,\mathrm{d}V$ map acquired at $V_G = 0\,\mathrm{V}$ (Fig. 4.3b) shows the same features as observed at biases corresponding to peaks 1-3 (Fig. 4.2b, first two panels), but the $\mathrm{d}I/\,\mathrm{d}V$ map acquired at $V_G = 60\,\mathrm{V}$ (Fig. 4.3c) exhibits a significantly different LDOS that is similar to what was observed previously for peak 4 (Fig. 4.2b, third panel). The LDOS at this fixed energy with respect to $E_F$ can thus be toggled between two different molecular orbitals via application of a positive gate voltage (this orbital switching is reversible and has no hysteresis).

We are able to understand our gate-dependent local electronic structure measurements of the hybrid CVB/graphene system through the use of first-principles simulations. The main questions we wish to answer here concern the origin and behavior of spectroscopic peaks 1-4 (Figs. 4.1,4.3). To do this we performed density functional theory (DFT) calculations of the combined CVB/graphene system using an exchange-correlation functional which combines the PBE functional together with a semi-empirical dispersion correction to take into account van der Waals interaction between the molecules and graphene [273, 274]. After correcting for electron-electron [258, 259, 277] and electron-phonon interactions [275,

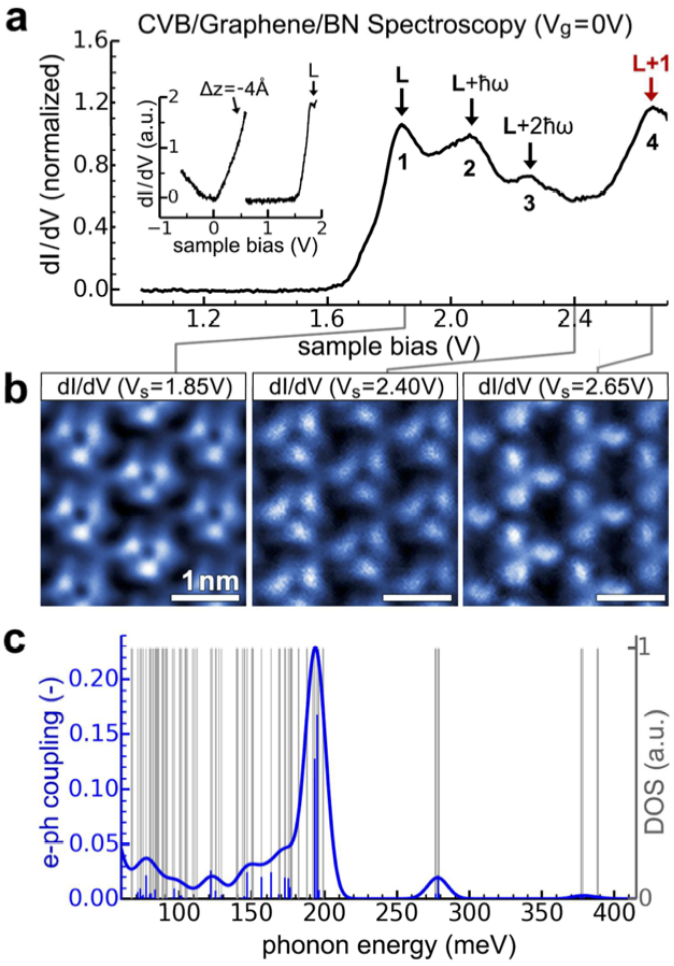


Figure 4.2: STM Spectroscopy of CVB/graphene/BN reveals vibronic response. **(a)** $\mathrm{d}I/\mathrm{d}V$ spectrum measured with STM tip held above a monolayer of CVB molecules on a graphene/BN FET device ($V_G = 0$). Spectrum is featureless over range $-0.5\,\mathrm{V} < V_S < 1.6\,\mathrm{V}$, but shows four clear molecule-induced resonances (marked 1-4) in the range $1.6\,\mathrm{V} < V_S < 2.8\,\mathrm{V}$ (junction set-point parameters $V_S = 2.7\,\mathrm{V}$, $I_t = 160\,\mathrm{pA}$; the spectrum is normalized by its value at 2.6 V). Inset shows a section of the $\mathrm{d}I/\mathrm{d}V$ spectrum over the range $-0.6\,\mathrm{V} < V_S < 0.6\,\mathrm{V}$ where the tip has been lowered by 4 Å relative to other spectra (junction set-point parameters: $V_S = 0.6\,\mathrm{V}$, $I_t = 40\,\mathrm{pA}$). Here the Dirac point can be observed at $V_S \approx 0\,\mathrm{V}$ ($V_G = 0\,\mathrm{V}$). Inset also shows onset of peak 1 ($0.6\,\mathrm{V} < V_S < 1.9\,\mathrm{V}$) for typical junction set-point parameters: $V_S = 1.9\,\mathrm{V}$, $I_t = 40\,\mathrm{pA}$. Peaks 1 and 4 are interpreted as LUMO and LUMO+1, respectively, while peaks 2 and 3 are interpreted as vibronic satellites of the LUMO (see text). **(b)** Experimental $\mathrm{d}I/\mathrm{d}V$ maps obtained at voltages $V_S = 1.85$, 2.4 and 2.65 V ($V_G = 0\,\mathrm{V}$). $\mathrm{d}I/\mathrm{d}V$ maps taken in range $1.85\,\mathrm{V} < V_S < 2.4\,\mathrm{V}$ probe the local density of states (LDOS) of peaks 1-3 and look very similar. The $\mathrm{d}I/\mathrm{d}V$ map taken at $V_S = 2.65\,\mathrm{V}$ probes peak 4 and yields a LDOS pattern that is different from the pattern observed for peaks 1-3. **(c)** Calculated density of states (DOS) of vibrational modes of CVB molecules on graphene (grey lines), as well as the electron-phonon coupling strength between the CVB vibrational modes and the CVB LUMO state (vertical blue lines). The blue curve shows the calculated electron-phonon coupling broadened with a Gaussian function of width 16 mV.

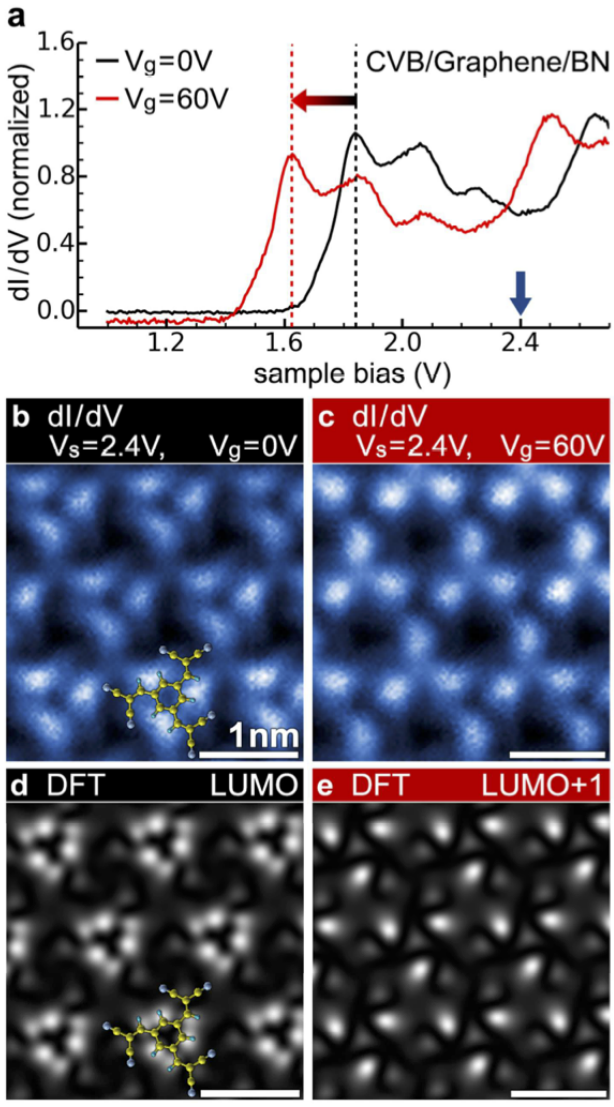


Figure 4.3: Gate-induced shift of the electronic levels of CVB molecules on a graphene/BN FET device. **(a)** $\mathrm{d}I/\mathrm{d}V$ spectra of CVB/graphene/BN at two different gate voltages: $V_G = 0\,\mathrm{V}$ (black trace) and $V_G = 60\,\mathrm{V}$ (red trace). Increasing the gate voltage to $V_G = 60\,\mathrm{V}$ causes a rigid downward shift of the molecular electronic resonances by 0.2 eV, consistent with the gate-induced shift seen in the Dirac point for graphene/BN devices without adsorbed molecules (spectra are normalized by their respective values at $V_S = 2.6\,\mathrm{V}$). **(b)** Experimental $\mathrm{d}I/\mathrm{d}V$ map obtained with $V_S = 2.4\,\mathrm{V}$ and $V_G = 0\,\mathrm{V}$. **(c)** Same as (b) except that $V_G = 60\,\mathrm{V}$. **(d)** Theoretical local density of states map of the CVB/graphene LUMO state calculated using DFT. **(e)** Same as (d) except for LUMO+1 state. These maps show that changing the device gate voltage allows the STM to access different molecular orbitals for a fixed sample bias.

276] in the electron self energy, we obtained a HOMO-LUMO energy gap of 6.3 eV and a (LUMO)-(LUMO+1) energy gap of 0.8 eV. Although our experimental energy range does not allow us to experimentally verify the predicted HOMO-LUMO gap, we note that the theoretical (LUMO)-(LUMO+1) energy almost perfectly matches the experimental energy difference between peaks 1 and 4 ($\Delta E_{14} = 0.82 \pm 0.04$ eV). This suggests that peak 1 is the CVB/graphene LUMO and that peak 4 is the LUMO+1 state. To further test this hypothesis we calculated the theoretical LDOS of the LUMO and LUMO+1 states and compared it to the experimental $\mathrm{d}I/\mathrm{d}V$ maps measured at the energies of peaks 1 and 4. The theoretical LDOS of these different states (Fig. 4.3d,e) is in good agreement with the experimental LDOS maps (first panel and third panel in Fig. 4.2b), thus providing additional evidence that peaks 1 and 4 correspond to the system's LUMO and LUMO+1 states (this procedure also allowed us to confirm the molecular orientation shown in Figs. 4.1 and 4.3).

An important remaining question is the origin of peaks 2 and 3, which do not appear in the calculated DOS obtained via DFT. These peaks clearly have some relation to the LUMO state, since their experimental $\mathrm{d}I/\mathrm{d}V$ maps are essentially identical to the $\mathrm{d}I/\mathrm{d}V$ map for peak 1 (Fig. 4.2b), and they strongly resemble the theoretical LDOS map that was calculated for the LUMO state (Fig. 4.3d). We believe that these additional peaks (2 and 3) arise due to the existence of vibronic modes of the CVB molecule on graphene. Such modes reflect coupling between the electronic and vibrational states of a molecule and result in new features in the electron spectral function. Vibronic modes have been seen previously in STM spectroscopy of molecules that are decoupled from a metallic substrate [52, 279, 280] (single-particle vibronic modes are quenched by direct molecular coupling to a metallic electrode [52, 280]). The spacing between vibronic satellites corresponds to the quantum of vibrational energy ($\hbar\omega$) for the molecular vibrational state that is entangled with the electronic orbital. Vibronic states do not appear in DFT calculations of electronic levels because the Born-Oppenheimer assumption prevents mixing of electronic states with vibrational modes.

To verify this picture, we calculated the theoretical vibrational modes for CVB molecules on graphene, as well as the electron-phonon coupling that exists between the molecular LUMO state and each vibrational mode. While the molecular vibrations are expected to span a wide energy range, we seek to understand whether strong electron-phonon coupling exists for any modes having energy similar to the energy difference between peaks 1 and 2 (0.2 eV), as well as between peaks 2 and 3 (0.22 eV). The grey lines in Fig. 4.2c show the theoretical vibrational modes of CVB on graphene, calculated within the framework of DFT perturbation theory. As expected, they span a wide energy range, up to 400 meV. The calculated electron-phonon coupling strength between these modes and the CVB LUMO state is shown by the bold blue trace in Fig. 4.2c. The electron-phonon coupling shows a strong peak at the modes near 200 meV, in good agreement with the experimental value of $\Delta E_{12}$ and $\Delta E_{23}$ which have an average value of 210 meV. From the calculation we are able to determine that the modes with high electron-phonon coupling at 200 meV mainly involve C-H rocking vibrations (which have representations $A_1'$, $E_1'$, and $E_2'$ of the $C_{3h}$ point group) suggesting that this particular type of vibration is the origin of the vibronic satellites observed experimentally as peaks 2 and 3 (a detailed calculation of electronic LDOS within

the 1st order cumulant approximation for the electron-phonon coupling is shown in the Supporting Information of [175]).

This vibronic interpretation of the $\mathrm{d}I/\mathrm{d}V$ spectrum helps to explain the gate-dependent orbital switching observed in $\mathrm{d}I/\mathrm{d}V$ maps obtained at a fixed tip-sample bias of $V_S = 2.4\,\mathrm{V}$. Here a gate voltage of $V_G = 0\,\mathrm{V}$ yields a $\mathrm{d}I/\mathrm{d}V$ map reflecting the LUMO density (Fig. 4.3b,d) while a gate voltage of $V_G = 60\,\mathrm{V}$ yields a $\mathrm{d}I/\mathrm{d}V$ map reflecting the LUMO+1 density (Figs. 4.3c,e). Within a vibronic picture the fixed tip-sample bias at $V_G = 0\,\mathrm{V}$ probes the peak 3 resonance which is a vibronic LUMO satellite, whereas gating at $V_G = 60\,\mathrm{V}$ shifts the tunnel current to the peak 4 resonance which reflects the LUMO+1 state. Electrostatic gating thus allows a fixed tip-sample bias to switch between imaging the LUMO and LUMO+1 orbitals.

In conclusion, we have shown that CVB molecules adsorbed onto a graphene/BN device self-assemble into a hexagonal lattice and develop vibronic peaks that correspond to coupling of electrons to the $A_1'$, $E_1'$, and $E_2'$ rocking modes of the CVB carbon-hydrogen bonds. The fact that vibronic peaks can be so readily resolved in the molecule/graphene spectra shown here suggests that substrate-induced lifetime broadening is weak on graphene due to electronic decoupling of adsorbed molecules [52, 280]. Gating the hybrid molecule/graphene device allows electronic switching between two different molecular states (LUMO and LUMO+1) for a fixed tip-sample bias voltage. Extensions of this approach can be envisioned that might allow exploration of gate-controlled changes in molecular functionality for hybrid graphene devices at the single-molecule level.

## 4.2 Tuning molecular charge states using a gated graphene device

In the previous section we tuned the orbitals of CVB through the application of a back-gate. However, since the frontier molecular orbitals were far from the Fermi energy we were not able to change the charge state of the molecules by moving their orbitals across the Fermi energy. Therefore, we moved to study a stronger electron acceptor tetrafluorotetracyanoquinodimethane (F4-TCNQ), which is known to have a very high electron affinity [136], and therefore orbitals that should lie closer to the graphene Dirac point. F4-TCNQ has also been shown to undergo charge transfer with graphene [137–139]. This leads to p-doping of the graphene and negative charging of F4-TCNQ, since electrons are transferred from graphene to the molecule. For this charge transfer to occur we expect the LUMO of F4-TCNQ to lie below the Fermi energy of graphene, which would make it susceptible to be tuned by applying a back-gate (assuming the LUMO is not too low in energy). Strong acceptors like F4-TCNQ, TCNQ or TCNE are also known to undergo charge transfer with metals [281–285], and experiments have shown that this charge transfer is accompanied by a strong surface reconstruction of the substrate [92, 282, 286, 287], e.g. Au(111), leading to metal-organic networks between molecules and individual metal atoms.

We tested our deposition procedure for F4-TCNQ by first depositing it onto Au(111). This allowed us to study the properties of F4-TCNQ on a simple metal, and shed more light on recent results in the literature (section 4.2.2). Then we deposited F4-TCNQ onto graphene and studied charge transfer within the F4-TCNQ/graphene system in addition to controllably switching the charge state of F4-TCNQ between neutral and negative states (section 4.2.3).

### 4.2.1 Methods

We deposited F4-TCNQ (Fig. 4.4g) from a Knudsen cell onto a Au(111) sample held at room temperature. The Au(111) crystal was previously prepared using the typical UHV argon-ion sputtering and annealing techniques. The sample was then cooled to $T = 4\,\mathrm{K}$ and measured using our Omicron low temperature STM/AFM system and CO was deposited at $T = 5\,\mathrm{K}$ for tip modification involving qPlus AFM measurements [172].

A back-gated graphene sample was used, as described in section 4.1.1. In order to take qPlus measurements of internal bond structure of adsorbed molecules on graphene we had to functionalize the tip with a single CO molecule. This tip functionalization is an important ingredient for sub-molecular resolution (see chapter 3 [172]), but CO molecules do not adsorb well onto graphene. We therefore deposited CO molecules onto Au(111) at $T = 5\,\mathrm{K}$ as usual, then functionalized the tip, and then exchanged the sample in the STM stage with graphene and approached the graphene while the CO molecule stayed adsorbed to the tip. On graphene we could then undertake qPlus measurements as in chapter 3.

### 4.2.2 F4-TCNQ adsorption configuration on Au(111)

F4-TCNQ on Au(111) was first studied with STM and STS by Hla and coworkers [281]. Later it was found that the strong interaction of F4-TCNQ with Au(111) leads to individual Au atoms being pulled towards the F4-TCNQ molecules, creating islands of metal-organic coordination bond networks [282]. Supporting evidence for this reconstruction came from STM images showing that the conventional herringbone reconstruction of Au(111) is destroyed due to the displacement of Au atoms. We studied this system with qPlus AFM with sub-molecular resolution in an effort to directly image the metal-organic bonds [121, 228] of such a network.

At low coverages we observed that F4-TCNQ adopts a flat-lying geometry on Au(111), with single molecules adsorbed with their long axis perpendicular to the gold step edges. At higher coverages, F4-TCNQ formed dimers, trimers and well-ordered islands (Fig. 4.4), similar to what was observed previously [281, 282]. In the STM images F4-TCNQ molecules in all adsorption configurations have featureless elongated shapes at the imaging parameters used here (Fig. 4.4a,c,e). However, in the island configuration (Fig. 4.4a), clear smaller round features are visible between F4-TCNQ molecules. In addition, the herringbone reconstruction of Au(111) is not visible on the islands.

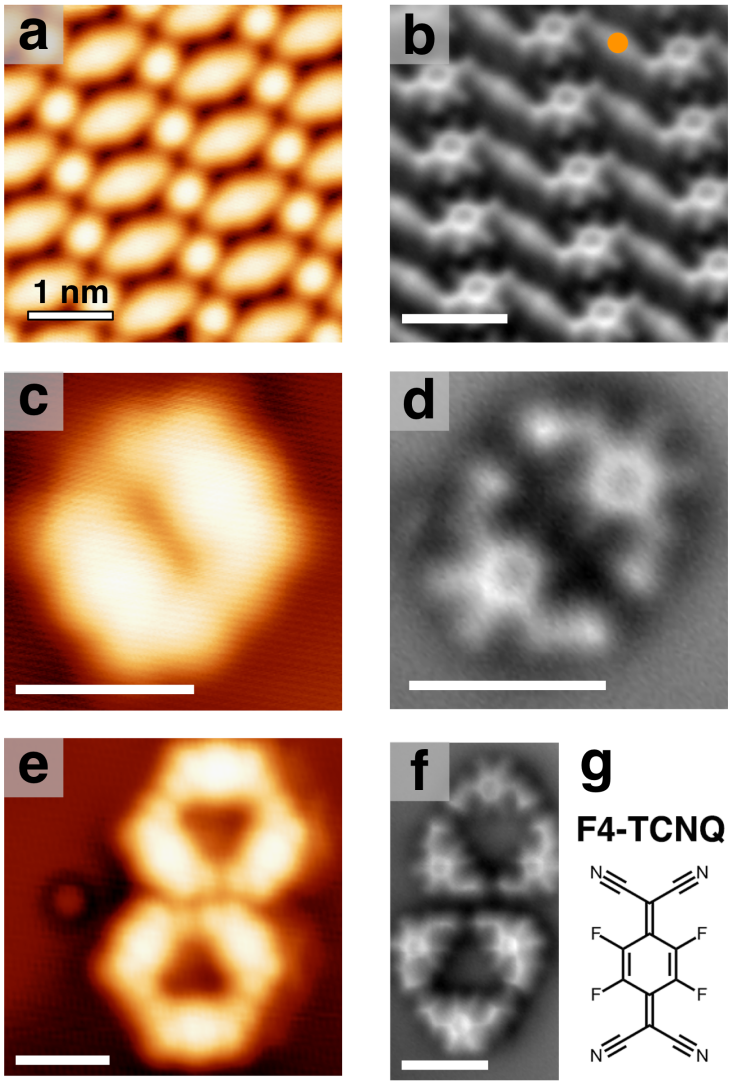


Figure 4.4: Various F4-TCNQ adsorption configurations on Au(111). **(a)** Constant current STM image of an island of F4-TCNQ on Au(111). In addition to the featureless oblong shapes of F4-TCNQ, round features appear between them. Imaging parameters: $V_S = 100\,\mathrm{mV}$, $I_t = 10\,\mathrm{pA}$. **(b)** Constant height qPlus measurement of frequency shift over the F4-TCNQ island (using a CO-modified tip). The chemical structures of individual F4-TCNQ molecules are clearly visible, with a central ring, fluorine atoms and cyano groups. The orange circle marks the position of additional bright, round protrusions, which we assign to vertically displaced Au atoms. Some cyano groups of the F4-TCNQ are not visible, possibly due to bending away from the tip towards the surface. **(c)** STM image of F4-TCNQ dimer. Imaging parameters: $V_S = 50\,\mathrm{mV}$, $I_t = 20\,\mathrm{pA}$. **(d)** qPlus image of F4-TCNQ dimer showing one missing pair of cyano groups for each molecule, indicating that they are bent towards the surface. This also shows that the molecules adsorb with cyano groups facing each other. **(e)** STM image of F4-TCNQ trimer. Imaging parameters: $V_S = 50\,\mathrm{mV}$, $I_t = 10\,\mathrm{pA}$. **(f)** qPlus image of F4-TCNQ trimer, revealing a missing pair of cyano groups as in (d) and cyano groups facing each other. **(g)** Chemical structure of F4-TCNQ.

qPlus AFM measurements of F4-TCNQ in these adsorption configurations (performed with a CO-modified tip) reveal the sub-molecular structure and intermolecular bonding configuration (Fig. 4.4b,d,f). For the dimers and trimers we notice that the chemical structure of F4-TCNQ (Fig. 4.4g) is nearly completely reproduced in the images, with a central C ring, four fluorine atoms connected to it, and cyano groups at the ends. However, only one pair of these cyano groups is visible, which suggests that the other side either dissociated from F4-TCNQ or is bent towards the surface, which would result in reduced contrast from these constant height images. For the island (Fig. 4.4b) we also observed F4-TCNQ chemical structure, again without measuring contrast from two cyano groups. Additionally, there are bright features in the qPlus image between the neighboring molecules' cyano groups. These bright, round, features are at the locations where bright features in STM images appear (Fig. 4.4a).

From previous DFT calculations [282, 283, 286] we know that F4-TCNQ and TCNQ can adopt a bent geometry when adsorbed onto metals. This is facilitated by the charge transfer to F4-TCNQ, which turns the rigid quinoidal structure into a more flexible aromatic one (this turns the C=C bonds between the central and neighboring C atoms into single bonds, which allows more freedom of rotation), as shown for TCNQ [286]. Additionally, due to the strong interaction between F4-TCNQ and Au(111), it was calculated [282] that Au atoms are displaced vertically and participate in the bonding between molecules. These two findings are corroborated by our qPlus measurements. We interpret the bright protrusions between F4-TCNQ in the island to be the vertically displaced Au atoms that bond to F4-TCNQ molecules, the bonds of which can also be seen in Fig. 4.4b. Additionally, we believe that the reason we cannot resolve one pair of cyano groups in the qPlus images of the island is due to those cyano groups bending towards the surface more than the others. For dimers and trimers we speculate that the Au atoms are vertically displaced and participate in the bonding, but are still far below the molecular plane and cannot be seen in the images (Fig. 4.4d,f), again we hypothesize that the unobserved cyano groups are bent strongly towards the Au(111) surface.

Our images of metal molecule bonds [121, 228] support the conclusions of [282] that when F4-TCNQ adsorbs onto Au(111) a surface reconstruction occurs, which involves vertical displacement of Au atoms and organo-metallic bonding leading to extended molecule-metal networks. Our qPlus images allow us to determine the bonding configuration by directly imaging the molecule-metal bonds and the lack of contrast on some of the cyano groups indicates that they are bent towards the Au(111) surface.

### 4.2.3 F4-TCNQ on graphene

In the previous section we saw that there are different adsorption configurations for F4-TCNQ on Au(111), which have been linked to charge transfer. In this section we will show that there is also charge transfer for F4-TCNQ on graphene and that the amount of charge transfer depends on the type of adsorption configuration, which we determine in detail *via* sub-molecular qPlus imaging (section 4.2.3.1). Furthermore, we will also demonstrate that

charge transfer can be tuned for single molecules through the application of a back-gate (section 4.2.3.2).

#### 4.2.3.1 Adsorption configuration of F4-TCNQ and charge transfer

As in section 4.2.2 we deposited F4-TCNQ from a Knudsen cell, but this time onto a graphene FET device at room temperature instead of Au(111). This graphene device allows back-gating, which leads to control of the Fermi level of graphene, as discussed in section 4.1. After deposition, the device was cooled to 4 K for STM and qPlus measurements.

At different deposition coverages the F4-TCNQ molecules adopted various adsorption configurations and for higher coverage a greater amount of p-doping of graphene was observed (Fig. 4.5). At low coverage F4-TCNQ formed isolated monomers on the surface of graphene. This is in contrast to other molecules, which have been deposited on graphene on insulators, e.g. PCDA [288, 289], CVB [175], CoPc [170], which all formed islands and were not observed as monomers. Even when scanning at small currents the F4-TCNQ monomers were not always stable (Fig. 4.5a). Their shape is similar to the LUMO of F4-TCNQ [282, 283], having a central oblong shape with four circular "lobes" at the corners. They appear evenly spaced, not randomly distributed, which would result in more heterogeneous molecule-molecule distances. The existence of monomers on the surfaces indicates relatively high binding of F4-TCNQ on graphene, possibly due to charge transfer, which might also explain the even spacing due to electrostatic repulsion.

For slightly higher coverage we observed the emergence of two new adsorption configurations: "chains" and "clusters" (Fig. 4.5b). Chains are formed by joining molecules along their long axis, with neighboring molecules slightly offset, which results in two possible connections between molecules and the formation of zig-zag and straight segments in chains. Clusters are usually formed by four molecules (though rarely trimers are also observed). The core of the four-molecule clusters contains two molecules connected head-on, i.e. not offset, along either the long or short axis of the molecules. The remaining two molecules each connect with one of their corners to the corners of the other two. For even higher coverages the chains and clusters become more dense and a second layer of molecules grows (Fig. 4.5c). The second layer molecules have similar geometries as the chains, but usually there is an additional bright feature close to an edge molecule that is not related to the typical molecule shape in any obvious way. Additionally, more extended islands are formed in some areas of the sample (Fig. 4.9). $\mathrm{d}I/\mathrm{d}V$ measurements on pristine graphene and at increasing F4-TCNQ coverages show that graphene becomes increasingly p-doped as the coverage of F4-TCNQ is increased (Fig. 4.5d). This p-doping of graphene indicates that electrons are transferred from graphene to F4-TCNQ, which has been observed before in photoemission experiments [137, 139] for F4-TCNQ on graphene on SiC, but never for molecules graphene/BN. The maximum shift in Fermi energy from p-doping with F4-TCNQ observed here is $\sim 200\,\mathrm{meV}$.

Since there is clear p-doping of graphene there must be charge transfer to some of the molecules. An important question to address is if the F4-TCNQ adsorption configuration

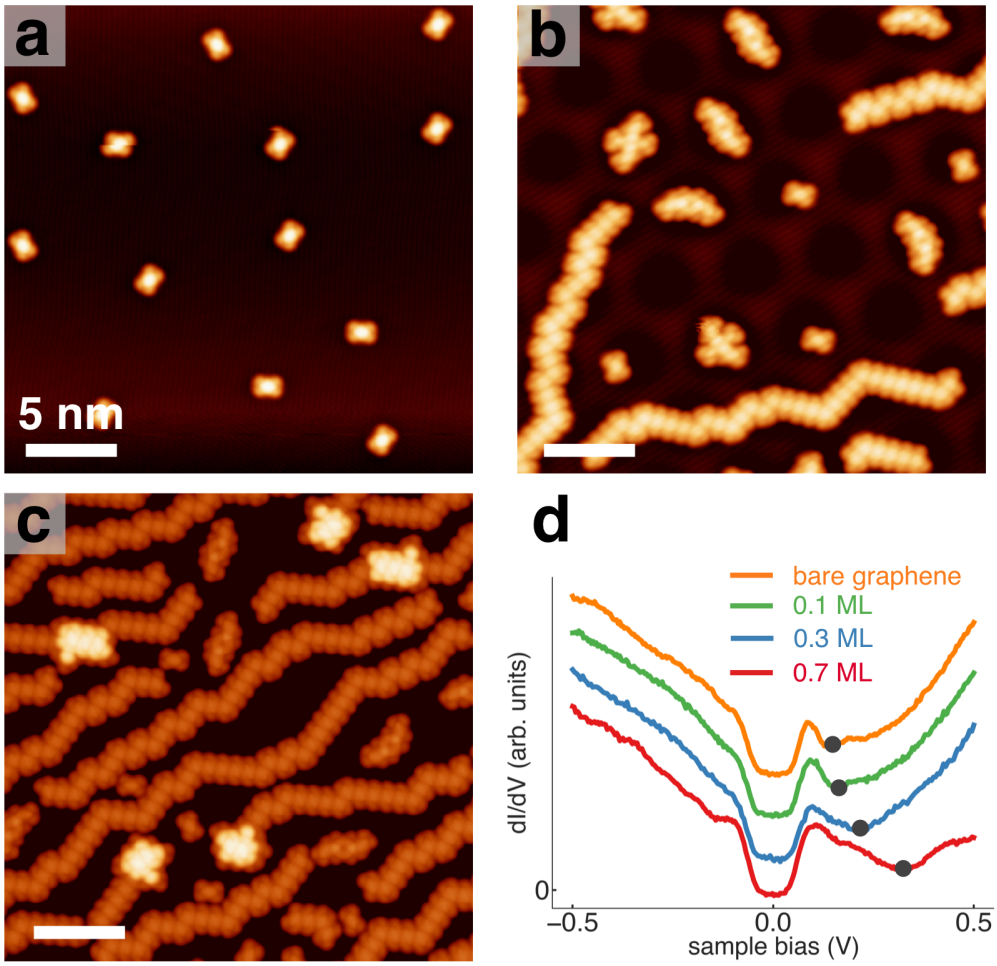


Figure 4.5: Various adsorption configurations of F4-TCNQ on graphene. **(a)** Lower coverage of $\sim$ 0.1 monolayers (ML). The F4-TCNQ molecules adsorb as roughly evenly spaced monomers. They are not always stable, even for low tunnel currents, as can be seen in sudden changes in position of some of the molecules. Imaging parameters: $V_S = 2.3\,\mathrm{V}$, $I_t = 5\,\mathrm{pA}$. **(b)** Higher coverage of $\sim$ 0.3 ML yields two new adsorption configurations: "chains" and "clusters". The chains are overall 1-d structures with zig-zag and straight segments and are formed by molecules arranged slightly offset from each other. Clusters are usually formed by four molecules, where the central two molecules are connected head-on (not offset). Imaging parameters: $V_S = 2\,\mathrm{V}$, $I_t = 5\,\mathrm{pA}$. **(c)** At even higher coverages of $\sim$ 0.7ML a second layer of molecules grows. It usually has similar structure as chains, but additional bright circular spots appear near the second layer molecules. Imaging parameters: $V_S = 2\,\mathrm{V}$, $I_t = 5\,\mathrm{pA}$. **(d)** Representative $\mathrm{d}I/\mathrm{d}V$ spectra taken on graphene for bare graphene and F4-TCNQ coverages similar to the ones shown in (a)-(c). The black dot indicates the Dirac point (see [268, 278] on graphene spectroscopy features) and is clearly shifting to higher energies for higher coverages, indicating increasing p-doping, with a maximum shift of $\sim 200\,\mathrm{meV}$.

has any influence on the amount of charge transfer. This can be tested through STM spectroscopy. It has been theoretically predicted [290–292] and experimentally verified [293] that a charged impurity in graphene leads to asymmetric $\mathrm{d}I/\mathrm{d}V$ spectra on graphene near the impurity. This asymmetry between the spectrum at positive and negative energies becomes less pronounced for areas on graphene that are farther away from the impurity. No such asymmetry is observed for neutral impurities.

We performed $\mathrm{d}I/\mathrm{d}V$ spectroscopy on graphene at various distances from monomers, chains, and clusters. For monomers it was not possible to do controlled measurements because the monomers moved due to the influence of the tip during spectroscopy measurements on the nearby graphene. For chains we did not observe any electron-hole asymmetry, indicating that the chains were not charged. For clusters, however, distance dependent $\mathrm{d}I/\mathrm{d}V$ on graphene revealed an asymmetry that weakened with increasing distance to the cluster (Fig. 4.6). The different positions probed are indicated by colored crosses in Fig. 4.6a. As the distance is decreased the $\mathrm{d}I/\mathrm{d}V$ value at $V_S = -0.5\,\mathrm{V}$ increases, while the value at $V_S = 0.5\,\mathrm{V}$ decreases. This qualitative behavior is consistent with the interpretation that the cluster is negatively charged as calculated in [290–292]. In the immediate vicinity of the cluster, we observe a slight depression (dark feature) in the STM image (Fig. 4.6c, white arrow). This could possibly indicate a screening cloud in graphene similar to what has been observed on other semiconductors around charged adsorbates [51, 294, 295]. A similar depression feature is absent near the chains (Fig. 4.6c, blue arrow), which further indicates that the clusters are charged while the chains are not.

To understand this adsorption dependent charge transfer between graphene and F4-TCNQ we performed spectroscopy on the chains and clusters of F4-TCNQ (Fig. 4.7). On clusters, $\mathrm{d}I/\mathrm{d}V$ spectroscopy reveals three main resonances, two below the Fermi energy and one above (Fig. 4.7b). Since the on-graphene spectroscopy of Fig. 4.6 indicates that the clusters are charged, we interpret the three resonances as HOMO, singly occupied orbital SOMO (previously LUMO) and uncharged SOMO+U above the Fermi level (whose energy is that of the SOMO plus the onsite Coulomb repulsion due to adding another electron), see Fig. 4.7b. The state above the Fermi level shows some additional features on a smaller scale, which might be related to vibronic states, as discussed in section 4.1 for CVB.

For the chains, however, the $\mathrm{d}I/\mathrm{d}V$ spectra were very different (Fig. 4.7d). There is a peak just above the Fermi level, with smaller features (again possibly related to vibronic states) and a very sharp feature at $\sim -1.1\,\mathrm{V}$. Because distance dependent spectroscopy indicates that chains are not charged we interpret the peak just above the Fermi level as the uncharged LUMO. The sharp feature at negative bias is similar to what has been observed previously for tip induced charging events, so we interpret it as such a "charging peak" [108, 296]. This charging event is caused by the tip bias creating a potential on the molecule which pulls the molecular orbital beyond the Fermi level and can therefore change the charge state of the molecule. High-resolution spectroscopy of F4-TCNQ monomers was not possible because they were unstable, moving laterally as well as jumping to the tip.

These measurements indicate that of all the molecules on graphene, only the clusters are charged (and also larger islands which have a similar adsorption configuration to clusters,

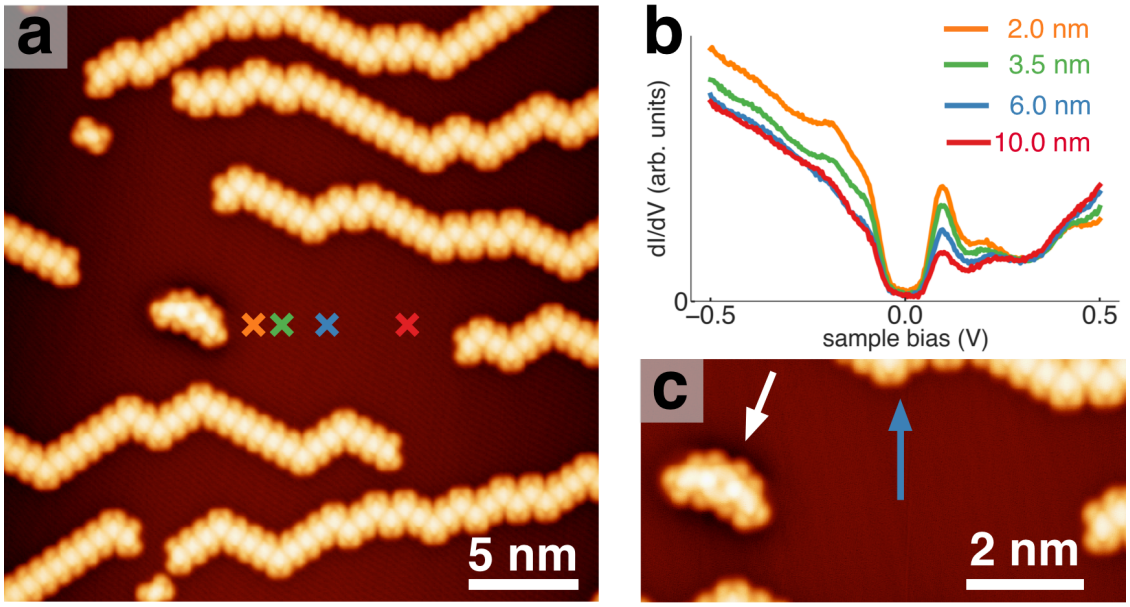


Figure 4.6: Graphene spectroscopy near clusters shows that the clusters are charged. **(a)** Overview STM image of the area where spectroscopy measurements were taken. The positions of $\mathrm{d}I/\mathrm{d}V$ measurements are indicated by colored crosses corresponding to similarly colored curves in (b). There is only one cluster in this region. **(b)** $\mathrm{d}I/\mathrm{d}V$ measurements on graphene for various distances from the cluster in (a). For small distances $\mathrm{d}I/\mathrm{d}V$ is higher at $V_S = -0.5\,\mathrm{V}$ and lower at $V_S = 0.5\,\mathrm{V}$ than farther away, which indicates that the cluster is negatively charged [290–293]. **(c)** Close-up STM image of the area, showing a slight dark depression very close to the cluster (white arrow), which is absent very close to the chains (blue arrow). All imaging parameters: $V_S = 2\,\mathrm{V}$, $I_t = 5\,\mathrm{pA}$.

see Fig. 4.9, with similar electronic structure), but the chains are not charged, at least when the tip is approached. A possible reason for this stark difference in electronic structure and charge state based on adsorption configuration could be a difference in polarization of the environment around the molecule, which leads to a different amount of screening of charge and can have an influence on the energy of the molecular orbitals. The molecular environment, specifically the number of polarizable neighbors, has been shown to shift the energy levels for molecules on metals [95]. This could have a bigger effect on the molecules in determining their charge states if the levels are shifted across the Fermi level.

To better understand the impact adsorption configuration might play in the energy level alignment and charge states of F4-TCNQ/graphene/BN, we performed qPlus and STM measurements with sub-molecular resolution on the F4-TCNQ chains (Fig. 4.8). A closeup STM image of a chain structure shows that the electronic structure of the chains looks quite different from a simple addition of monomer shapes (Fig. 4.8a). This indicates orbital overlap and significant hopping between molecules. qPlus images of the chain structures are shown in Fig. 4.8b. These images reveal unambiguously that the molecules are arranged parallel to each other but offset, such that two of the fluorine atoms on one side of the central

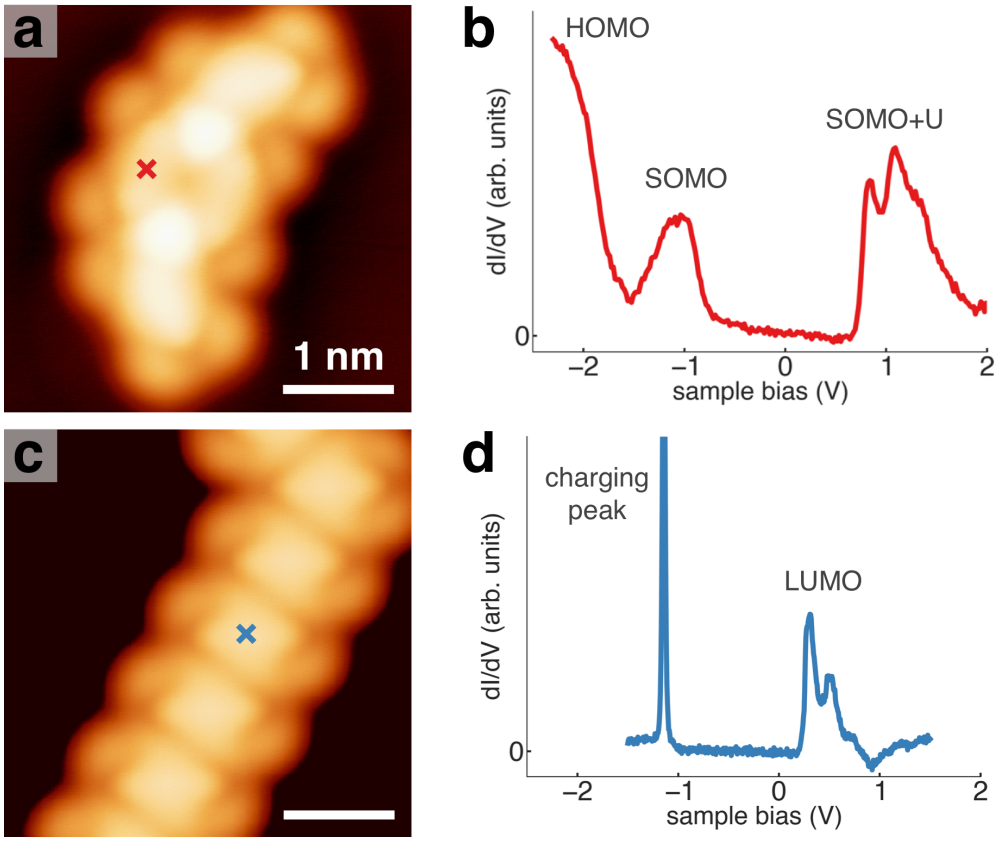


Figure 4.7: Spectroscopy for two different adsorption configurations show different electronic structure. **(a)** STM close-up image of a cluster, showing how F4-TCNQ orbitals overlap on the corners of the molecules. The red cross indicates the position where spectroscopy was taken. All imaging parameters: $V_S = 2\,\mathrm{V}$, $I_t = 10\,\mathrm{pA}$. **(b)** $\mathrm{d}I/\mathrm{d}V$ spectrum taken at the red cross in (a). Three main resonances are visible, which we assign to the HOMO, singly occupied orbital SOMO (former LUMO), and the SOMO+U (whose energy is that of the SOMO plus the onsite repulsion from adding another electron). We expect the LUMO of the free molecule to now be below the Fermi energy (as the SOMO) because graphene spectroscopy indicates that clusters are charged. **(c)** STM close-up image of the chains, shows orbital overlap at the corners of slightly different type than for clusters. The blue cross indicates the spectroscopy location. **(d)** $\mathrm{d}I/\mathrm{d}V$ spectrum at the blue cross in (c). There are two main features. The first is a broad resonance just above the Fermi energy which we assign to the empty LUMO because graphene spectroscopy shows that chains are not charged. The other one is a sharp feature at $\sim -1.1\,\mathrm{V}$, which we assign to a charging peak that occurs due to sudden charging of the molecule through the application of a tip bias.

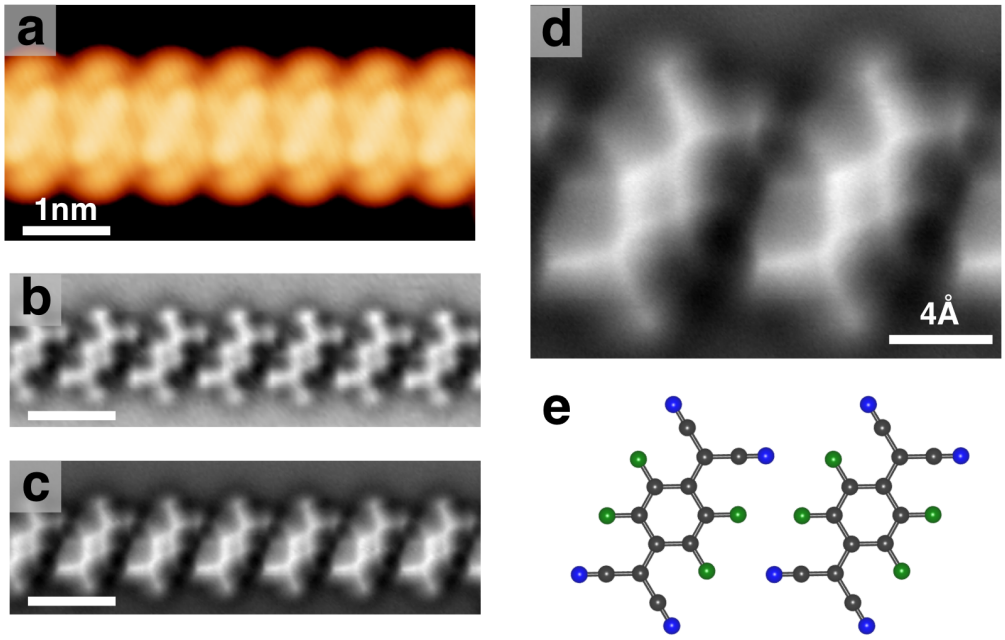


Figure 4.8: One dimensional "chain" adsorption configuration for F4-TCNQ. **(a)** STM constant current image of a chain of F4-TCNQ molecules on graphene/BN. The orbital structure of the molecules shows overlap, which suggests a certain degree of electron hopping and delocalization between molecules. Imaging parameters: $V_S = 2\,\mathrm{V}$, $I_t = 5\,\mathrm{pA}$. **(b)** Constant height qPlus frequency shift image of the same chain. The adsorption configuration of the molecules can clearly be determined from the image. The molecules are aligned in parallel to each other, offset such that fluorine atoms on the central ring of one molecule are lined up next to a nitrogen atom of the neighbor. **(c)** qPlus image with lower tip height than (b) to increase contrast. **(d)** Zoom in on two molecules in the chain, showing very faint lines connecting two fluorines of the right molecule with a nitrogen of the left molecule. This might either indicate bonding between molecules or be an imaging artifact due to tilting of the CO on the tip. **(e)** Ball and stick model of the adsorption configuration shown in the images.

carbon ring are lined up with a cyano group of the neighboring molecule (Fig. 4.8e). The image does not reveal any obvious covalent bonding between molecules, as one might expect given the STM data. Even an image taken at lower tip height for increased contrast does not show any such bonding (Fig. 4.8c). A zoom-in on one pair of molecules (Fig. 4.8d) does show very faint lines connecting the fluorine atoms of one molecule to the nitrogen atoms of the neighbor. It is not clear how to interpret these lines because they could either indicate bonding electron density, or possibly an imaging artifact caused by tilting of the CO molecule on the tip. Further theoretical modeling of the molecule-tip system has to be done to conclusively determine which interpretation is correct.

In addition to clusters, chains, and monomers, we also found F4-TCNQ molecules arranged into larger islands on the graphene/BN surface (Fig. 4.9). $\mathrm{d}I/\mathrm{d}V$ spectroscopy of these islands showed the same features as clusters, indicating that they are also charged. Therefore, they serve as a more ordered geometry to investigate the origin of the differences

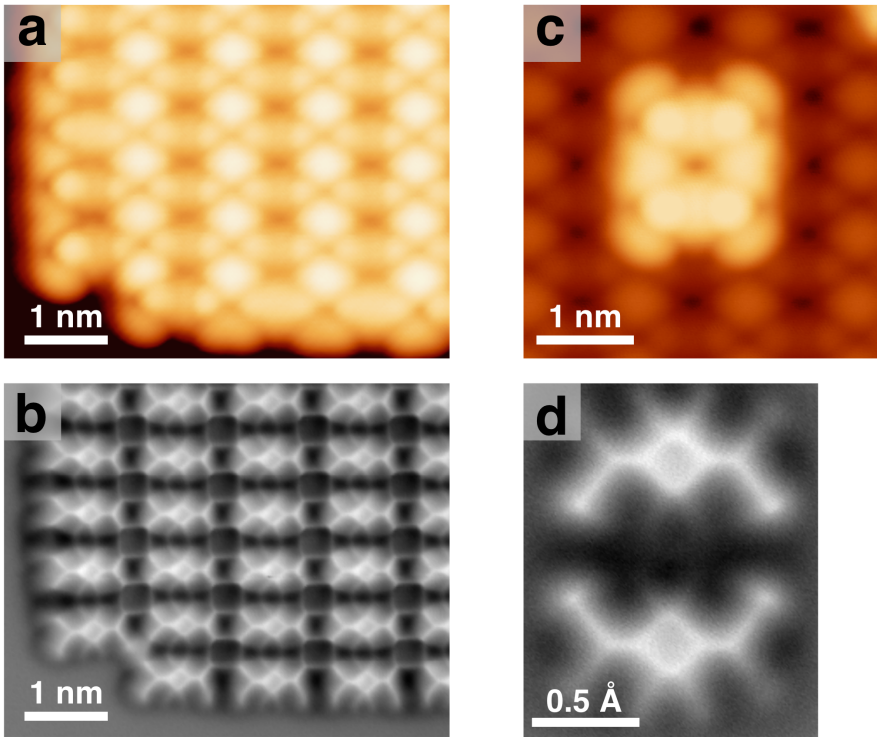


Figure 4.9: Adsorption configuration for islands of F4-TCNQ. **(a)** Constant current STM image of F4-TCNQ on graphene in the island geometry. The orbitals of the molecules show clear overlap, which could indicate significant electron hopping and delocalization between molecules. Imaging parameters: $V_S = 2\,\mathrm{V}$, $I_t = 7\,\mathrm{pA}$. **(b)** Constant height qPlus frequency shift image of the same island. Thin lines can be seen, connecting nitrogen atoms of neighboring molecules to each other. **(c)** Constant current STM image of an F4-TCNQ dimer on top of an F4-TCNQ island. There is orbital overlap and the molecule positions are commensurate with the underlying F4-TCNQ lattice. Imaging parameters: $V_S = 2\,\mathrm{V}$, $I_t = 5\,\mathrm{pA}$. **(d)** Constant height qPlus image of the same dimer, revealing the internal bond structure of the molecules but no lines between them.

in electronic structure between clusters/islands and chains. STM images of these islands show clear signs of orbital overlap, which could indicate electron delocalization within the island (Fig. 4.9a). To understand the precise adsorption configuration of these islands we performed constant height qPlus AFM imaging, which showed that the molecules are arranged parallel and head-on relatively to each other (Fig. 4.9b). At this tip height we can also clearly observe thin lines connecting nitrogen atoms of neighboring molecules with each other. Again this may either indicate a bond, the existence of which would be surprising in this configuration, or an imaging artifact. We will discuss this further using height dependent images below (Fig. 4.10). We also observed the growth of a second layer of F4-TCNQ on top of molecular islands (Fig. 4.9c). qPlus images of the adsorption configuration of the dimer (Fig. 4.9d) does not show any lines between nitrogens.

In an effort to better understand the nature of the faint connecting lines between molecules

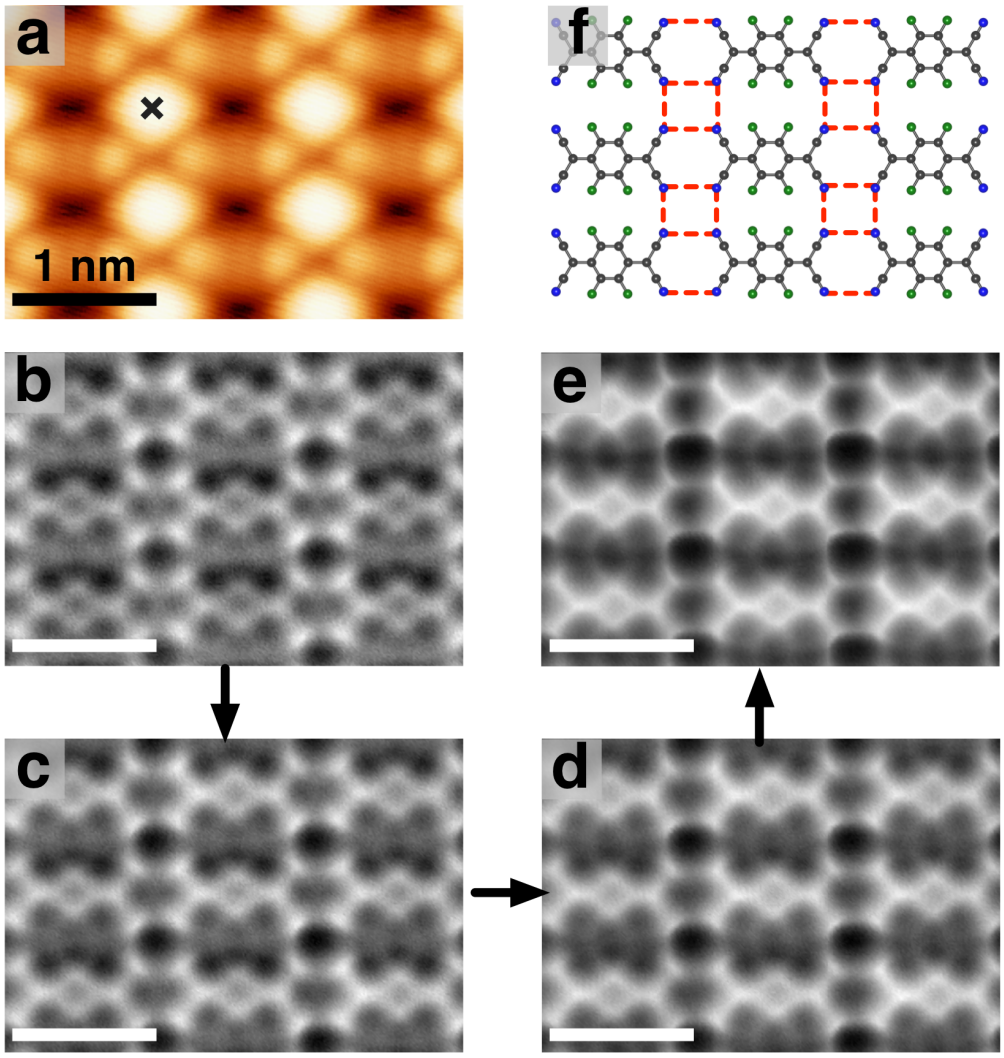


Figure 4.10: Tip height dependent qPlus images of F4-TCNQ islands show the appearance of intermolecular bonding. **(a)** Close up STM image of nine molecules within an F4-TCNQ island. All tip heights given in this caption are relative to a tunneling setpoint of $V_s = 2\,\mathrm{V}$ and $I_t = 5\,\mathrm{pA}$ at the location of the cross. Imaging parameters: $V_S = 2\,\mathrm{V}$, $I_t = 60\,\mathrm{pA}$. **(b)** qPlus image of the same area at a tip height of $\Delta z = -0.30\,\mathrm{nm}$. There are no bright lines between molecules, however one can see regions of increased intensity near the triple bonds of the CN groups. **(c)** qPlus image at tip height $\Delta z = -0.32\,\mathrm{nm}$. **(d)** qPlus image at tip height $\Delta z = -0.33\,\mathrm{nm}$. **(e)** qPlus image at $\Delta z = -0.34\,\mathrm{nm}$. Here, clear thin lines are visible between the CN groups of neighboring molecules. **(f)** Adsorption configuration using ball and stick models. The red dashed lines indicate the position of the thin line features in the qPlus images.

in islands seen in qPlus images (Fig. 4.9b) we imaged an area of nine molecules within an island at various tip heights (Fig. 4.10). It is known from previous studies [227] that the CO molecule on the tip tilts more when it is closer to a surface molecule which can result in sharper lines representing the bonds in images. In our images (Fig. 4.10b-e) we moved the tip closer for each image and the sharp thin lines began to emerge for close tip heights, but were absent at larger tip heights. In contrast, at higher tip heights, areas of increased intensity are visible near the CN triple bonds, similar to what has been shown in chapter 3 and previous work [173, 174]. One hypothesis for the emergence of the sharp line features for smaller tip heights is that the CO tip switches between two metastable tilt positions due to the large electron density of the neighboring triple bonds.

As we have seen above there are several adsorption configurations for F4-TCNQ on graphene/BN whose precise nature determines the charge states of the molecules for zero applied gate voltage. To test whether we could switch the charge states of adsorbed molecules we applied a range of gate voltages $-60\,\mathrm{V} < V_s < 60\,\mathrm{V}$. The result was that $\mathrm{d}I/\mathrm{d}V$ spectroscopy showed almost no effect of the gate on clusters, and that for chains the molecules often became unstable when applying a gate.

When studying this instability more systematically, however, we found that chains could be dissociated through the application of a back-gate in combination with the influence of the tip (Fig. 4.11). We imaged an area of graphene where a number of molecules were adsorbed in the chain configuration (Fig. 4.11a). Then we positioned the tip in the top left corner of the image, while applying a sample bias of 2 V and a gate voltage of 55 V for 5 minutes. We then turned off the gate voltage and rescanned the same area. Some of the chains had now dissociated into monomers, and after repeating this procedure three more times many more molecules had dissociated from chains and now existed as monomers on the surface (Fig. 4.11b). This phenomenon did not occur if the gate was not applied at all, or if the tip was withdrawn far from the surface while the gate was applied. The influence of both the gate and the tip in concert with each other leads to this dissociation. This leads to the following hypothesis. Since we have seen before that the LUMO in the chains is relatively close to the Fermi energy (Fig. 4.11d), it is possible that the application of a positive back-gate voltage of 55 V is sufficient to shift the LUMO below the Fermi level and therefore charge the molecules negatively. These negatively charged molecules are still bonded to each other in the chain configuration if no tip is near, apparently because the bonding strength exceeds the coulomb repulsion. When the tip is near the molecules, however, the negative tip bias creates an electric field which could lead to the dissociation of the negatively charged chains, because each monomer is additionally repelled by the tip. This hypothesis would also explain why it was difficult to perform controlled $\mathrm{d}I/\mathrm{d}V$ spectroscopy on chains while applying a gate.

To conclude this section, we have deposited F4-TCNQ molecules onto a gated graphene/BN device and demonstrated that there is charge transfer from the graphene to the molecules. This charge transfer was shown to be highly dependent on the local adsorption configuration of the molecules, with chains being neutral and clusters and islands being negatively charged. We investigated the differences in adsorption configuration in an effort to explain

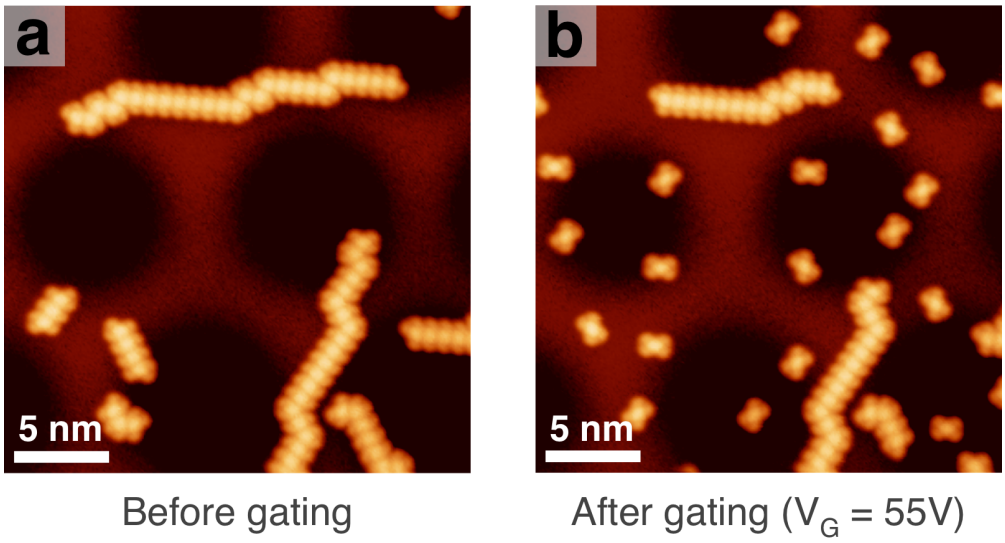


Figure 4.11: Diffusion of molecules, remotely actuated by the back-gate and the tip. **(a)** STM image of F4-TCNQ molecules in chain configuration on graphene/BN, before applying a gate voltage, imaged at $V_G = 0\,\mathrm{V}$. **(b)** STM image at $V_G = 0\,\mathrm{V}$ of the same area after multiple steps of applying a gate voltage of $V_G = 55\,\mathrm{V}$ and imaging at $V_G = 0\,\mathrm{V}$. Many chains have dissociated into isolated monomers. Imaging parameters: $V_S = 2\,\mathrm{V}$, $I_t = 1\,\mathrm{pA}$.

these differences, using qPlus imaging with individual-bond resolution. These images showed that the molecules in chains are offset from each other while in islands they are aligned head on. Additionally we observed the appearance of sharp lines between molecules in islands, which might either indicate intermolecular bonds or an imaging artifact. We could not controllably monitor the evolution of the local density of states for molecules as we applied a gate voltage because of the molecules' instability. Nevertheless, we were able to use the back-gate to achieve remotely actuated molecular motion, likely a combination of charging of the molecules and the electrostatic influence of the biased tip.

#### 4.2.3.2 Controlling the charge state of individual molecules

In the previous section we discussed how it was not possible to controllably use the gate voltage and perform spectroscopy on F4-TCNQ molecules in chain or monomer configuration. Additionally, we found an intriguing difference in the electronic structure of F4-TCNQ in chain and cluster/island configuration. To understand this better, we needed to find a way to study the simplest adsorption configuration, the monomer of F4-TCNQ. Our solution to this problem was to deposit a different molecule, 10,12-pentacosadiynoic acid (PCDA), on graphene/BN to serve as an anchor for F4-TCNQ, which made stable imaging, spectroscopy and gating possible for individual molecules.

We deposited PCDA [288, 289] molecules from a Knudsen cell onto a back-gated graphene/BN device at room temperature, before also depositing F4-TCNQ (Fig. 4.12). The PCDA

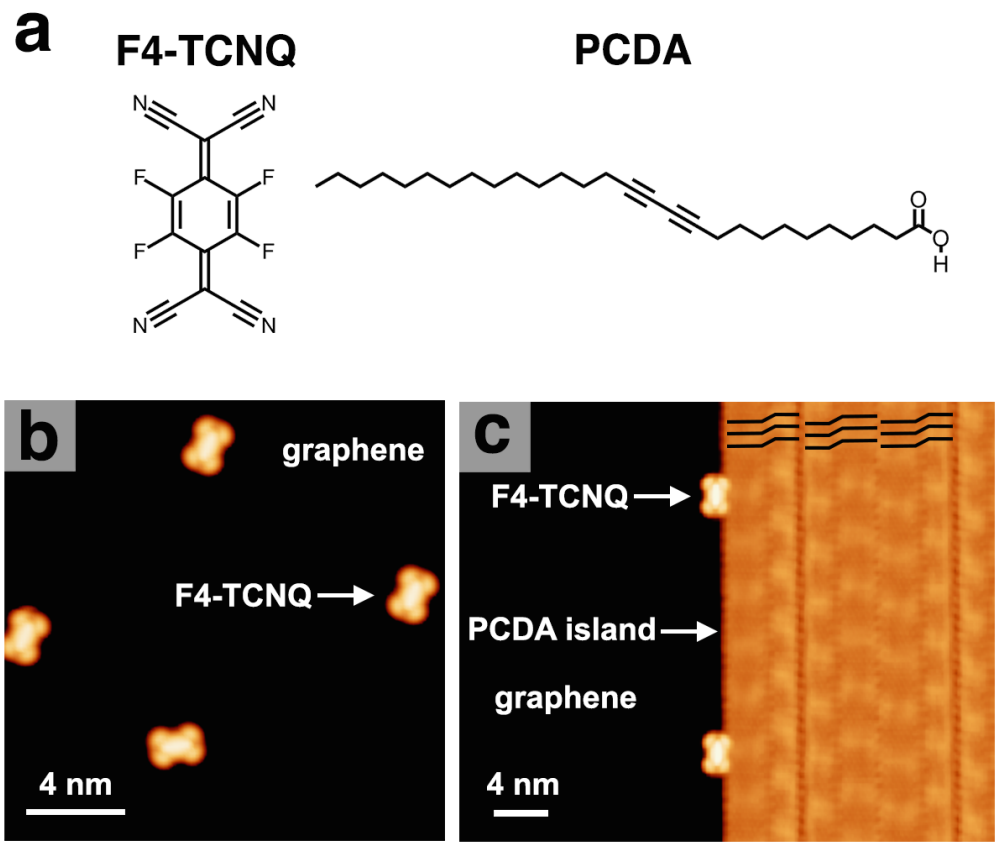


Figure 4.12: Monomers of F4-TCNQ on graphene/BN, stabilized by PCDA. **(a)** Chemical structure of F4-TCNQ and PCDA. **(b)** STM image of F4-TCNQ monomers adsorbed onto graphene/BN. At low coverages the molecules arrange as roughly evenly-spaced monomers. However, they are not stable enough to perform high resolution STS or qPlus measurements. Imaging parameters: $V_S = 2\,\mathrm{V}$, $I_t = 5\,\mathrm{pA}$. **(c)** STM image of F4-TCNQ monomers adsorbed at the edges of PCDA islands on graphene/BN. The molecules within the PCDA island are aligned as indicated by the black lines in the upper right. The F4-TCNQ molecules are strongly bound to the islands, which enables STS and qPlus measurements. Imaging parameters: $V_S = 2\,\mathrm{V}$, $I_t = 10\,\mathrm{pA}$.

adsorbs into well-ordered islands and the F4-TCNQ binds at the PCDA island edge, usually along the F4-TCNQ's long axis (Fig. 4.12c). This sufficiently stabilized F4-TCNQ for further STS and even qPlus measurements.

In an effort to understand the nature of the bonding between PCDA and F4-TCNQ that stabilizes the monomers, we performed qPlus measurements. These measurements give a detailed view of the precise adsorption configuration by showing the graphene honeycomb lattice, the F4-TCNQ molecule, and the PCDA molecules all with individual-bond resolution (Fig. 4.13). Fig. 4.13a also shows a zoom-in STM image of F4-TCNQ adsorbed at a PCDA island edge. The corresponding qPlus AFM image of the same area shows the precise adsorption configuration (Fig. 4.13b). Usually qPlus images with sub-molecular resolution are taken at constant height, but in this case we used a slightly different procedure. In

order to image the graphene, the higher-lying F4-TCNQ, and the even higher-lying PCDA, we had to adjust the tip height at two positions to always achieve high enough contrast in the frequency shift. We, therefore, started the image at a large tip height on the right side (the PCDA side), scanning top to bottom to capture PCDA with sub-molecular resolution. When the tip reached F4-TCNQ, we lowered the tip height and continued scanning at the new constant height to image F4-TCNQ. When the tip was well past the F4-TCNQ, we lowered the tip again to capture the honeycomb lattice of graphene (see Fig. 4.13b, lower panel, the locations where the tip height was changed are indicated with black arrows).

This procedure allowed us to capture the bond structure of all the different elements in one image. This image clearly reveals the honeycomb lattice of the graphene, the hydrogen atoms along the PCDA molecules and the triple bonds within PCDA, which are areas of higher electron density. The chemical bonds within F4-TCNQ are also resolved, including a slight distortion of the central ring of F4-TCNQ where the two vertical C=C bonds on the sides appear shorter than the others. This is consistent with the quinoidal nature of F4-TCNQ, i.e. the outside bonds are double bonds. C=C double bonds have been shown to appear shorter in qPlus AFM images due to the tilting of the CO on the tip [227], which exaggerates the actual difference in bond length between single and double bonds.

A zoom-in qPlus image of the F4-TCNQ molecule shows signs of bonding between F4-TCNQ and PCDA (Fig. 4.13c,d). In the qPlus image (Fig. 4.13d) we can observe faint lines connecting nitrogen and fluorine atoms of F4-TCNQ to hydrogen atoms of PCDA, the suggested locations of which are indicated in Fig. 4.13c. As discussed in section 4.2.3.1 such lines may indicate intermolecular bonds between F4-TCNQ and PCDA or imaging artifacts. In this case our hypothesis is that these lines do represent intermolecular bonds, in particular hydrogen bonds, because they are known to form between nitrogen/fluorine and hydrogen. Another indication that these lines are actual physical features as opposed to measurement artifacts is the fact that they are not completely mirror symmetric around a central horizontal axis through F4-TCNQ, even though the adsorption configuration is. The upper nitrogen shows two bonds while the lower nitrogen only shows one. However, the relative positions of hydrogens and nitrogens for both the top and bottom parts of the molecule are similar. We assume that there is only a slight difference in geometry between top and bottom, e.g. the distance between nitrogen and hydrogen, and that hydrogen bonds only form suddenly at a specific minimum distance while any measurement artifacts are continuously dependent on the distance between atoms. If these assumptions are correct we can conclude that the complete absence of a line between nitrogen and hydrogen at the bottom of the molecule indicates that these lines represent hydrogen bonds [229], and that the distance at the bottom of the molecule is too big for such a bond to be formed.

Gate-dependent scanning tunneling spectroscopy reveals the existence of a molecular state near the Fermi energy ($E_F$), which can be shifted below and above $E_F$, thus controlling its filling and the molecule's resulting charge state (Fig. 4.14). Even though this molecule is bonded to the PCDA island, we found that the $dI/dV$ spectra of F4-TCNQ molecules are not significantly altered compared to the isolated F4-TCNQ monomers on graphene, for which we could take low resolution spectra with large tip height (not shown). Fig. 4.14a

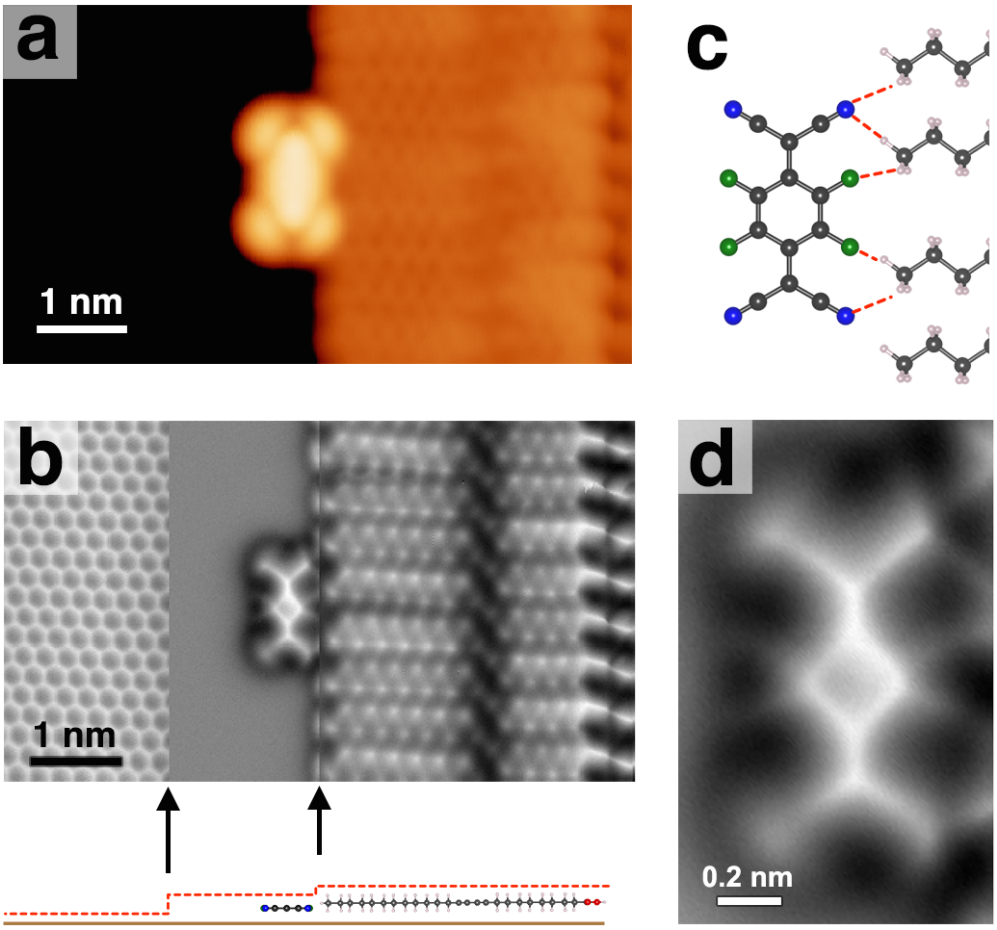


Figure 4.13: Individual-bond resolution images of graphene honeycomb lattice, F4-TCNQ and PCDA. **(a)** STM image of a single F4-TCNQ molecule adsorbed at the edge of a PCDA island. Imaging parameters: $V_S = 2\,\mathrm{V}$, $I_t = 8\,\mathrm{pA}$. **(b)** qPlus image of the same area. The image was taken at three different constant heights, the tip height was adjusted down from PCDA to F4-TCNQ and then to graphene heights at the positions indicated by arrows. The red dashed line indicates the tip height during imaging. The qPlus image shows the honeycomb lattice of graphene, the slightly distorted F4-TCNQ internal bond structure (the C=C bonds on the side are shorter because of their double bond nature), and the PCDA internal structure. For PCDA we observe the upwards pointing hydrogen atoms as well as the triple bond locations between two sections of PCDA which show slightly higher intensity within an area of overall lowered intensity due to the lack of upward pointing hydrogen atoms. **(c)** Ball and stick model of the adsorption configuration with red dashed lines indicating the proposed positions of the faint lines in (d), connecting F4-TCNQ and PCDA. **(d)** Zoom in qPlus image of F4-TCNQ. The slight distortion of the C=C bonds on the side of the central ring is more obvious here (appearing much shorter than the others). Faint lines connecting fluorine and nitrogen atoms of F4-TCNQ to hydrogen atoms of PCDA are visible. There are two lines connected to the top nitrogen but only one to the bottom nitrogen.

shows $\mathrm{d}I/\mathrm{d}V$ spectra taken on the center of an F4-TCNQ monomer adsorbed at the edge of a PCDA island as in (Fig. 4.13). There are a number of different features that the spectra have in common. Each spectrum has at least one broad peak with smaller evenly spaced satellite peaks farther away from the Fermi energy: for a gate voltage of $-50\,\mathrm{V}$ (blue) this peak is at positive sample bias, for a gate voltage of $-30\,\mathrm{V}$ (red) this peak is at negative sample bias, and for a gate voltage between the previous two, $10\,\mathrm{V}$ (green), there are two of these features, one on each side of the Fermi energy. Additionally, there is a very sharp, high-intensity feature for both the blue and red curves ($-50\,\mathrm{V}$ and $30\,\mathrm{V}$, respectively) at sample biases of opposite sign compared to the broad feature. The spectra on these sides have been scaled by the factors indicated, in order to fit both the sharp and broad features on the same plot. The sharp features are labelled "charging" for reasons described below.

In addition to the on-molecule spectroscopy, we performed off-molecule spectroscopy over bare graphene close to the molecules, which gives insight into the charge state of the molecules (Fig. 4.14b,c). As discussed in section 4.2.3.1, it has been shown that charged impurities in graphene create a distance-dependent electron-hole asymmetry in the graphene LDOS and resulting $\mathrm{d}I/\mathrm{d}V$ curves [290–293]. For a negative impurity $\mathrm{d}I/\mathrm{d}V$ below the Dirac point increases and above the Dirac point decreases as one moves closer to the impurity. We observed no such asymmetry in the $\mathrm{d}I/\mathrm{d}V$ of graphene near F4-TCNQ when the gate was $-50\,\mathrm{V}$, which lowers the Fermi level compared to $V_G = 0\,\mathrm{V}$ (Fig. 4.14b). However, when the gate was tuned to $30\,\mathrm{V}$ we did observe such an asymmetry in the $\mathrm{d}I/\mathrm{d}V$, with the same qualitative behavior as predicted for a negatively charged impurity (Fig. 4.14c). Since a gate voltage of $30\,\mathrm{V}$ shifts the Fermi level higher compared to $0\,\mathrm{V}$, this indicates that the LUMO of the F4-TCNQ is filled at this gate voltage and the molecules become negatively charged.

With this new insight that the molecules become charged when the gate is $30\,\mathrm{V}$ and uncharged at $-50\,\mathrm{V}$, we can now better interpret the peaks in Fig. 4.14a. Since the broad peak and its smaller satellites are above the Fermi energy at $V_G = -50\,\mathrm{V}$ and are pulled below the Fermi energy at $V_G = 30\,\mathrm{V}$, we can assign this feature to the free molecule LUMO. We will use the convention of always labeling this orbital as LUMO, even when it is in the singly occupied state (which might otherwise be referred to as a singly occupied molecular orbital (SOMO)). Our convention of using LUMO simplifies communication when we discuss switching of molecular charge states and shifting of the LUMO below and above the Fermi energy (since the name of the state remains constant). To make a distinction between the LUMO of the neutral and the LUMO of the charged molecules we will sometimes refer to them as $\mathrm{LUMO}^0$ and $\mathrm{LUMO}^-$, respectively. Since the satellites are roughly evenly spaced, and show a similar intensity as observed previously for CVB molecules (section 4.1 [175]) we interpret them as vibronic modes of the LUMO. This interpretation is supported by the fact that they always appear on the other side of the LUMO compared to the Fermi energy, which corresponds to higher energy vibronic modes.

We interpret the sharp, high-intensity peaks on opposite sides of the LUMO (relative to $\mathrm{E_F}$) as "charging peaks" that are due to tip-gating of the molecule [107, 108, 296, 297]. From the qPlus AFM measurements shown in Fig. 4.13 we know that F4-TCNQ lies $\sim 3\,\mathrm{Å}$

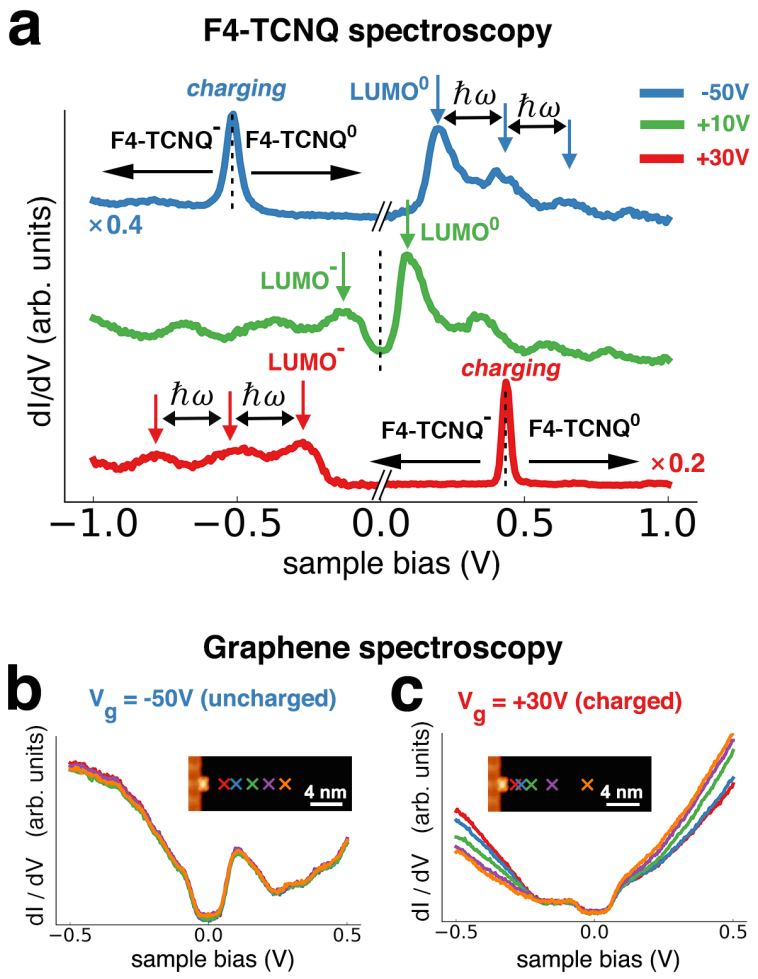


Figure 4.14: Gate-induced charging of F4-TCNQ. **(a)** d$I$/d$V$ spectra taken at the center of the F4-TCNQ molecules adsorbed at the edge of PCDA. The blue curve shows a broad uncharged LUMO$^0$ above the Fermi energy, with smaller vibronic modes at higher energies and a sharp, intense "charging peak" at negative bias (note the scaling of the spectrum at negative bias). Similarly the red curve shows a charged LUMO$^-$ below the Fermi level with smaller vibronic modes at lower energies and a charging peak at positive bias. When the applied bias is below the charging peak the molecule is always negatively charged and above the charging peak it is always neutral. For the green curve no charging peak is visible but instead both, a LUMO$^0$ and LUMO$^-$ peak, are observed. In this case we hypothesize that the charging event happens at very small bias, and the LUMO "jumps" across the Fermi energy, beyond the tip bias, before being sampled again by the sweeping tip bias, as a usual molecular resonance. **(b)** Graphene spectroscopy near an F4-TCNQ monomer while the gate voltage is −50 V shows no dependence on the distance of the tip from the molecule, indicating that the monomer is neutral [293]. **(c)** Graphene spectroscopy near an F4-TCNQ monomer while the gate voltage is 30 V shows a clear asymmetry between filled and empty states, which is dependent on the distance to the molecule. Here the d$I$/d$V$ below and above the Dirac point shifts up and down, respectively. This is consistent with a negatively charged impurity [290–292].

higher than graphene, which generates a double barrier tunnel junction (DBTJ) between the tip, F4-TCNQ, and graphene. This causes a fraction, $\alpha$, of the potential applied to the tip to fall off between F4-TCNQ and graphene, which effectively shifts the energy of the molecular orbitals relative to the graphene. For a given sign of sample bias this leads to a shift of molecular energies of the opposite sign. For example, if the LUMO is slightly above the Fermi energy, as for $V_G = -50\,\mathrm{V}$ (blue) in Fig. 4.14a, then a large negative sample bias would shift the LUMO below the Fermi level and thereby charge the molecule. The charging peak is seen due to the sudden electronic perturbation of having the LUMO be pulled below the Fermi level. This means that for any sample bias below the charging peaks, the molecule is negatively charged, while for any bias above the charging peak it is neutral.

The last feature to explain regarding the spectra in Fig. 4.14a is the simultaneous appearance of both the $\mathrm{LUMO}^0$ and $\mathrm{LUMO}^-$. In this case, we believe that the tip-induced charging event happens at very small bias, with the LUMO being shifted to energies beyond this bias. As the voltage is swept during spectroscopy, the LUMO shifts across the Fermi energy at small bias, and is then sampled as usual when the sample bias reaches the energy position of the shifted LUMO. A necessary condition for this to be true is that the LUMO cannot smoothly shift when crossing the Fermi level, but needs to shift discontinuously, or "jump" across the Fermi level.

To further understand the gate-dependent spectroscopy of F4-TCNQ we took a series of spectra for more finely spaced gate voltages (Fig. 4.15). In Fig. 4.15a we can see the now familiar features of F4-TCNQ spectroscopy with $\mathrm{LUMO}^0$ and $\mathrm{LUMO}^-$ resonances, vibronic modes and charging peaks (see Fig. 4.14 for comparison and introduction to these features). From top to bottom the gate voltage is increased, which shifts the Fermi level to higher energies. We would therefore expect spectroscopic features that resemble the local density of states to shift to the left. This is true for the LUMO feature, and in a certain sense for the vibronic features, although they switch from being above the LUMO to being below the LUMO energy, as expected for vibronic modes (which always lie opposite to the side of $\mathrm{E_F}$). The charging peaks, however, shift opposite to the direction of the LDOS features, which means that the charging peak is not an LDOS feature. We note that for some gate voltages between $6\,\mathrm{V} < V_G < 12\,\mathrm{V}$, the charging peak coincides with the LUMO.

In Fig. 4.15b we present simulated $\mathrm{d}I/\mathrm{d}V$ spectra calculated from a simple model that involves DBTJ-induced "jumping" of the LUMO across the Fermi level, which is in good agreement with the experimental curves in Fig. 4.15a. For this model we assume a Gaussian peak for the state in LDOS, and take the measured $\mathrm{d}I/\mathrm{d}V$ at a certain bias $V_s$ to be the derivative of the current from tunneling through all states between 0 V and $V_s$. Additionally, to simulate the DBTJ we assume that the potential at the molecule is $-\alpha V_s$, relative to the graphene, where $\alpha = 0.2$ is a fitting parameter from an analysis of the relationship of LUMO and charging peak in Fig. 4.15a. As the sample bias is swept in this model the Gaussian state shifts by $\alpha V_s$. When the state gets within $\sim 0.1\,\mathrm{eV}$ of the Fermi level it jumps across suddenly. This results in the sudden, sharp peak at the tip bias at which $\alpha V_s$ shifts the resonance across the Fermi level, because a new state on the same bias side as the charging peak becomes available for tunneling, leading to a step in current and a peak in $\mathrm{d}I/\mathrm{d}V$. If

we do not assume any discontinuous jump, then the charging peak is usually much broader than the original LUMO, which is not experimentally observed (Fig. 4.15a). The simple model, which includes a "jump" of the LUMO across the Fermi level, succeeds in capturing all the essential features of the gate-dependent spectra of Fig. 4.15a: the shift of the charging peak is opposite the shift of the LUMO, the sharp charging peak coincides with the LUMO for some LUMO positions, and the charging peak disappears when the LUMO is close to the Fermi level and both the $\mathrm{LUMO}^0$ and the $\mathrm{LUMO}^-$ are measured in one spectrum.

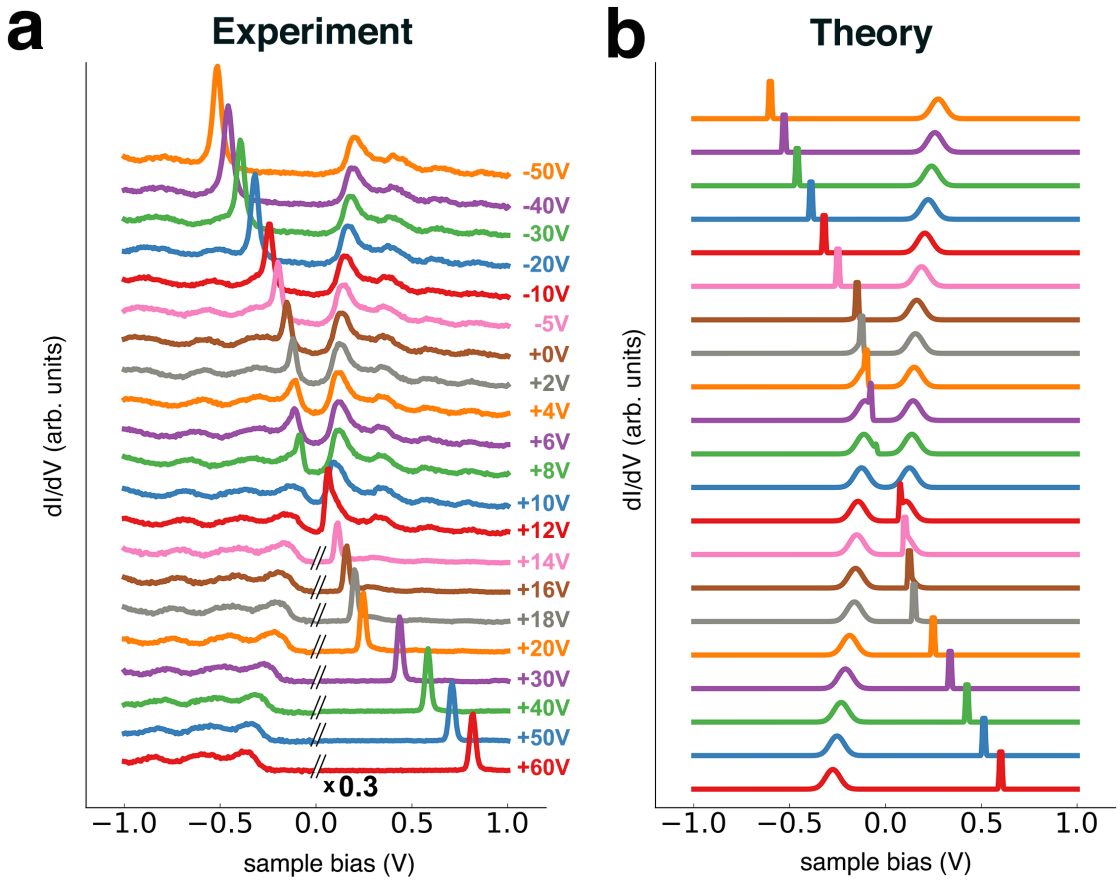


Figure 4.15: Comparison of gate dependent spectra with theoretical model. **(a)** $\mathrm{d}I/\mathrm{d}V$ curves for a single F4-TCNQ molecule adsorbed at the edge of PCDA for a range of different gates. As the gate voltage is increased (from top to bottom) most spectroscopic features like the LUMO and vibronic peaks shift to lower energy, consistent with the Fermi level shifting to higher energy. The sharp peak shifts in the opposite direction, providing further evidence for the "charging peak" interpretation of this spectroscopic feature [296]. **(b)** Simulated $\mathrm{d}I/\mathrm{d}V$ curves from a simple model, which calculates $\mathrm{d}I/\mathrm{d}V$ as the derivative of the total tunnel current generated by tunneling through all states between 0 V and the sample bias voltage. Additionally we assume that the LUMO discontinuously "jumps" across the Fermi level when it gets close to the Fermi level. The experimental features are well reproduced by this simple model.

To further test our hypothesis that the sharp spectroscopic feature is the charging peak we performed bias-dependent qPlus AFM contact potential measurements at large positive

gate voltages, i.e. when the molecule was charged due to the gate (Fig. 4.16). These measurements (for a single F4-TCNQ molecule adsorbed at the edge of a PCDA island (Fig. 4.16a)) revealed the usual parabolic curve for the frequency shift vs. sample bias (see section 2.2.3), the maximum of which indicates the sample bias which nullifies the local contact potential difference between tip and sample (Fig. 4.16b). However, we also observed a dip at large positive bias. These dips have previously been correlated with tip charging events of single quantum dots [181, 298–300]. The appearance of dips can be readily explained by the DBTJ model. When the tip is held at the bias where the dip appears the bias is sufficient to charge the molecule by producing a large enough potential at the molecule's location. This can happen even when the tip is not directly on top of the molecule because the tip also creates a potential laterally. This potential is smaller than directly below it, which explains why the charging peak is at such a large bias when measured off the molecule. During one oscillation cycle at this bias the tip moves farther away and out of the range where it can shift the molecular orbital across the Fermi energy. As a result the molecule's charge state is modulated between negative charge and neutrality asynchronously with the AFM tip oscillation. This modulates the force on the tip, which results in dissipation and a decrease in frequency shift. Frequency shift images at different biases show rings of various sizes (Fig. 4.16c,d) which correspond to the locations where charging dips appear in the $\Delta f$ signal at the corresponding bias. The nearly circular shape of the ring, centered at the molecule, indicates that in order to charge the molecule the potential at the center of the molecule needs to reach a certain value, which varies with gate voltage but it does not depend on the direction of tip location relative to the molecule. Additionally, the increase in ring size as the bias is increased can be understood because at higher bias the charging or discharging event can happen when the tip is farther away because then a smaller fraction of the tip bias falls off between molecule and graphene, leading to the same potential at the molecule.

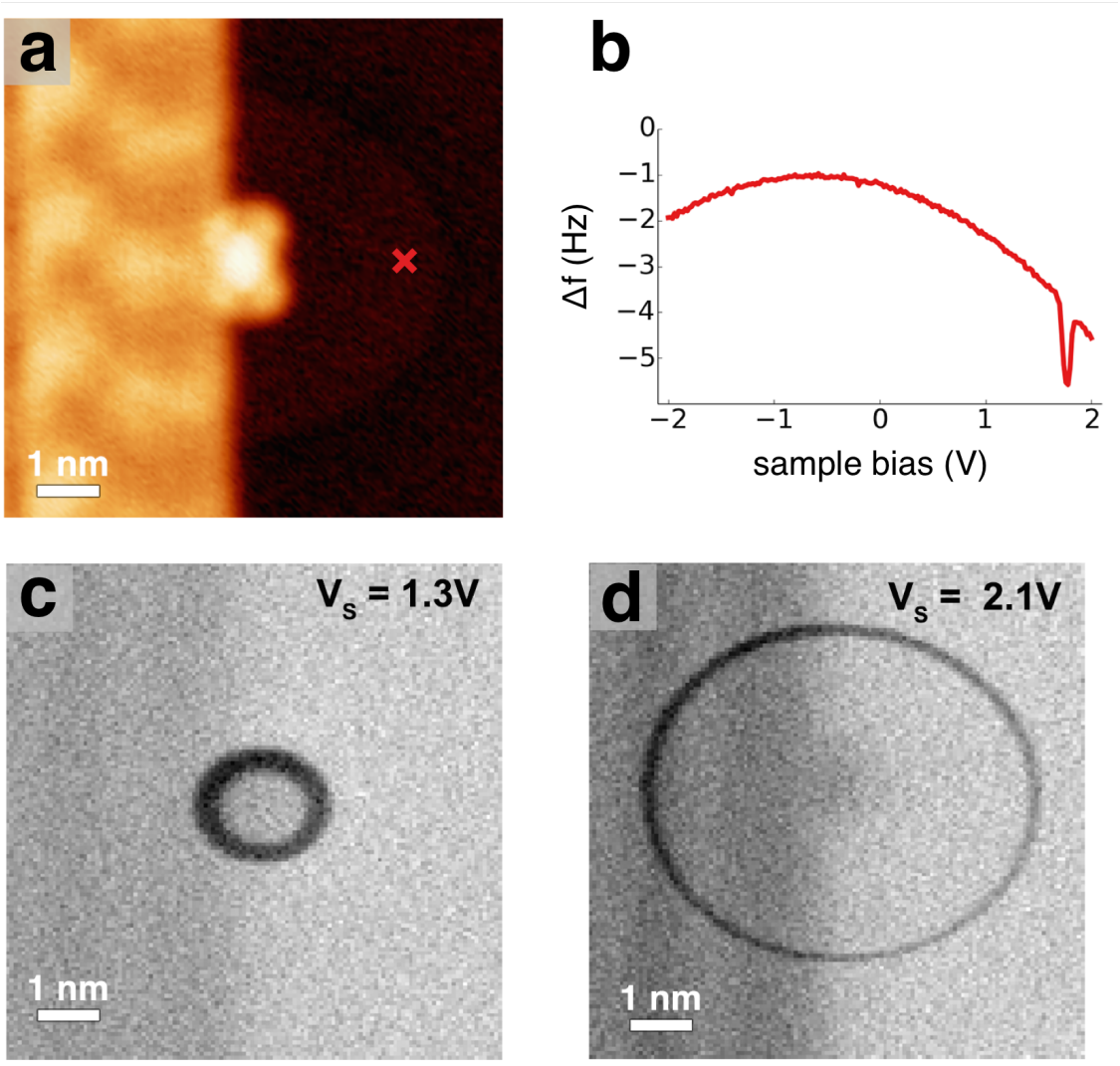


Figure 4.16: Bias-induced charging events measured as rings in frequency shift images. **(a)** STM image of a single F4-TCNQ molecule adsorbed at a PCDA island. The red cross indicates the location of the bias dependent frequency measurement in (b). A faint ring feature can be observed in the image, which is due to tip-induced charging and discharging of the molecule. Imaging parameters: $V_S = 2\,\mathrm{V}$, $I_t = 10\,\mathrm{pA}$. **(b)** Bias-dependent frequency shift curve taken at the location indicated by the red cross in (a). The usual parabolic shape yielding the local contact potential difference is observed, along with a striking dip feature at $\sim 1.9\,\mathrm{V}$. This dip feature can be be explained by tip-induced charging events [181, 298–300]. **(c)** Constant height frequency shift image of the same area at $V_s = 1.3\,\mathrm{V}$ showing a small ring centered at the center of the F4-TCNQ molecule. The ring corresponds to the dip feature in (b), and is nearly circular because the potential at the molecule is independent of the angular position of the tip. This ring is relatively small because the sample bias is small, which requires the tip to be close to the F4-TCNQ in order to reach the critical potential at the molecule to tip-gate it. **(d)** Constant height frequency shift image of the same area at $V_s = 2.1\,\mathrm{V}$. This ring is larger because the sample bias is larger, requiring a bigger distance between F4-TCNQ and tip for tip-gating of the charge state.

## 4.3 Conclusion

We have demonstrated that a back-gated graphene FET device can be used to tune the orbital energies and charge states of adsorbed molecules while local probe techniques are used to provide electronic structure information at the single-molecule level. For CVB molecules on graphene we studied the coupling between electrons and phonons which yielded vibronic modes, which had not been demonstrated on graphene before. Applying a back-gate to graphene allowed remote control of the CVB orbital energies, which we used to switch between tunneling into either LUMO or LUMO+1 states by changing the gate voltage for fixed sample bias. In a significant extension of this approach we deposited a stronger acceptor, F4-TCNQ, onto the same kind of graphene device, which allowed direct control of the molecular charge state. F4-TCNQ causes significant surface reconstruction in combination with charge transfer on Au(111), which we demonstrated with sub-molecular resolution using qPlus AFM imaging. On graphene this molecule also undergoes charge transfer, which results in p-doping of graphene as a function of molecular coverage. We have shown this charge transfer to be highly adsorption configuration dependent, with "chains" of molecules remaining neutral while "clusters" and islands accept negative charge from the graphene. We stabilized monomers of F4-TCNQ through deposition of an "anchor molecule", PCDA, which formed extended islands to which F4-TCNQ adsorbed at the edge. This stabilization made high resolution local probe measurements possible. Such measurements revealed that the application of a back-gate can remotely, controllably, and reversibly switch F4-TCNQ between neutral and negative charge states. This new level of molecular control takes us a significant step closer to the goal of single molecule electronics.

# Bibliography


[1] Richard Feynman. *There's Plenty of Room at the Bottom.* 1960. URL: http://resolver.caltech.edu/CaltechES:23.5.0.

[2] P. W. Anderson. "Localized Magnetic States in Metals". In: *Phys. Rev.* 124 (1 Oct. 1961), pp. 41–53. DOI: 10.1103/PhysRev.124.41. URL: http://link.aps.org/doi/10.1103/PhysRev.124.41.

[3] C. Joachim, J. K. Gimzewski, and A. Aviram. "Electronics using hybrid-molecular and mono-molecular devices". In: *Nature* 408.6812 (Nov. 30, 2000), pp. 541–548. URL: http://dx.doi.org/10.1038/35046000.

[4] Johannes V Barth, Giovanni Costantini, and Klaus Kern. "Engineering atomic and molecular nanostructures at surfaces". In: *Nature* 437.7059 (Sept. 2005), pp. 671–679.

[5] Gregory Franc and Andre Gourdon. "Covalent networks through on-surface chemistry in ultra-high vacuum: state-of-the-art and recent developments". In: *Phys. Chem. Chem. Phys.* 13 (32 2011), pp. 14283–14292. DOI: 10.1039/C1CP20700H. URL: http://dx.doi.org/10.1039/C1CP20700H.

[6] Xuemei Zhang, Qingdao Zeng, and Chen Wang. "On-surface single molecule synthesis chemistry: a promising bottom-up approach towards functional surfaces". In: *Nanoscale* 5 (18 2013), pp. 8269–8287. DOI: 10.1039/C3NR01611K. URL: http://dx.doi.org/10.1039/C3NR01611K.

[7] F. Ullmann. "Ueber eine neue Bildungsweise von Diphenylaminderivaten". In: *Berichte der deutschen chemischen Gesellschaft* 36.2 (1903), pp. 2382–2384. ISSN: 1099-0682. DOI: 10.1002/cber.190303602174. URL: http://dx.doi.org/10.1002/cber.190303602174.

[8] Paul E. Fanta. "The Ullmann Synthesis of Biaryls". In: *Synthesis* 1974.01 (1974), pp. 9–21. DOI: 10.1055/s-1974-23219.

[9] Marco Bieri et al. "Two-Dimensional Polymer Formation on Surfaces: Insight into the Roles of Precursor Mobility and Reactivity". In: *Journal of the American Chemical Society* 132.46 (2010), pp. 16669–16676. DOI: 10.1021/ja107947z. eprint: http://pubs.acs.org/doi/pdf/10.1021/ja107947z. URL: http://pubs.acs.org/doi/abs/10.1021/ja107947z.

[10] Carlos J. Villagómez et al. "Bottom-up Assembly of Molecular Wagons on a Surface". In: *Journal of the American Chemical Society* 132.47 (2010), pp. 16848–16854. DOI: 10.1021/ja105542j. eprint: http://pubs.acs.org/doi/pdf/10.1021/ja105542j. URL: http://pubs.acs.org/doi/abs/10.1021/ja105542j.

[11] Manh-Thuong Nguyen, Carlo A. Pignedoli, and Daniele Passerone. "An ab initio insight into the Cu(111)-mediated Ullmann reaction". In: *Phys. Chem. Chem. Phys.* 13 (1 2011), pp. 154–160. DOI: 10.1039/C0CP00759E. URL: http://dx.doi.org/10.1039/C0CP00759E.

[12] Saw-Wai Hla et al. "Inducing All Steps of a Chemical Reaction with the Scanning Tunneling Microscope Tip: Towards Single Molecule Engineering". In: *Phys. Rev. Lett.* 85 (13 Sept. 2000), pp. 2777–2780. DOI: 10.1103/PhysRevLett.85.2777. URL: http://link.aps.org/doi/10.1103/PhysRevLett.85.2777.

[13] Leonhard Grill et al. "Nano-architectures by covalent assembly of molecular building blocks". In: *Nat Nano* 2.11 (Nov. 2007), pp. 687–691. URL: http://dx.doi.org/10.1038/nnano.2007.346.

[14] LafferentzL. et al. "Controlling on-surface polymerization by hierarchical and substrate-directed growth". In: *Nat Chem* 4.3 (Mar. 2012), pp. 215–220. URL: http://dx.doi.org/10.1038/nchem.1242.

[15] Leif Lafferentz et al. "Conductance of a Single Conjugated Polymer as a Continuous Function of Its Length". In: *Science* 323.5918 (2009), pp. 1193–1197. DOI: 10.1126/science.1168255. eprint: http://www.sciencemag.org/content/323/5918/1193.full.pdf. URL: http://www.sciencemag.org/content/323/5918/1193.abstract.

[16] Christian Bombis et al. "Single Molecular Wires Connecting Metallic and Insulating Surface Areas". In: *Angewandte Chemie International Edition* 48.52 (2009), pp. 9966–9970. ISSN: 1521-3773. DOI: 10.1002/anie.200904645. URL: http://dx.doi.org/10.1002/anie.200904645.

[17] Jinming Cai et al. "Atomically precise bottom-up fabrication of graphene nanoribbons". In: *Nature* 466.7305 (July 22, 2010), pp. 470–473. URL: http://dx.doi.org/10.1038/nature09211.

[18] Yen-Chia Chen et al. "Tuning the Band Gap of Graphene Nanoribbons Synthesized from Molecular Precursors". In: *ACS Nano* 7.7 (2013), pp. 6123–6128. DOI: 10.1021/nn401948e. eprint: http://pubs.acs.org/doi/pdf/10.1021/nn401948e. URL: http://pubs.acs.org/doi/abs/10.1021/nn401948e.

[19] Marco Bieri et al. "Porous graphenes: two-dimensional polymer synthesis with atomic precision". In: *Chem. Commun.* (45 2009), pp. 6919–6921. DOI: 10.1039/B915190G. URL: http://dx.doi.org/10.1039/B915190G.

[20] J. A. Lipton-Duffin et al. "Synthesis of Polyphenylene Molecular Wires by Surface-Confined Polymerization". In: *Small* 5.5 (2009), pp. 592–597. ISSN: 1613-6829. DOI: 10.1002/smll.200801943. URL: http://dx.doi.org/10.1002/smll.200801943.

[21] J. A. Lipton-Duffin et al. "Step-by-step growth of epitaxially aligned polythiophene by surface-confined reaction". In: *Proceedings of the National Academy of Sciences* 107.25 (2010), pp. 11200–11204. DOI: 10.1073/pnas.1000726107. eprint: http://www.pnas.org/content/107/25/11200.full.pdf+html. URL: http://www.pnas.org/content/107/25/11200.abstract.

[22] Hermann Walch et al. "Material- and Orientation-Dependent Reactivity for Heterogeneously Catalyzed Carbon-Bromine Bond Homolysis". In: *The Journal of Physical Chemistry C* 114.29 (2010), pp. 12604–12609. DOI: 10.1021/jp102704q. eprint: http://pubs.acs.org/doi/pdf/10.1021/jp102704q. URL: http://pubs.acs.org/doi/abs/10.1021/jp102704q.

[23] Gregory S. McCarty and Paul S. Weiss. "Formation and Manipulation of Protopolymer Chains". In: *Journal of the American Chemical Society* 126.51 (2004). PMID: 15612715, pp. 16772–16776. DOI: 10.1021/ja038930g. eprint: http://pubs.acs.org/doi/pdf/10.1021/ja038930g. URL: http://pubs.acs.org/doi/abs/10.1021/ja038930g.

[24] Rico Gutzler et al. "Surface mediated synthesis of 2D covalent organic frameworks: 1,3,5-tris(4-bromophenyl)benzene on graphite(001), Cu(111), and Ag(110)". In: *Chem. Commun.* (29 2009), pp. 4456–4458. DOI: 10.1039/B906836H. URL: http://dx.doi.org/10.1039/B906836H.

[25] Matthias Treier et al. "Surface-assisted cyclodehydrogenation provides a synthetic route towards easily processable and chemically tailored nanographenes". In: *Nat Chem* 3.1 (Jan. 2011), pp. 61–67. URL: http://dx.doi.org/10.1038/nchem.891.

[26] Gonzalo Otero et al. "Fullerenes from aromatic precursors by surface-catalysed cyclodehydrogenation". In: *Nature* 454.7206 (Aug. 14, 2008), pp. 865–868. URL: http://dx.doi.org/10.1038/nature07193.

[27] Nadjib Baadji et al. "Controlled sequential dehydrogenation of single molecules by scanning tunneling microscopy". In: *Phys. Rev. B* 82 (11 Sept. 2010), p. 115447. DOI: 10.1103/PhysRevB.82.115447. URL: http://link.aps.org/doi/10.1103/PhysRevB.82.115447.

[28] Konstantin Amsharov et al. "Towards the Isomer-Specific Synthesis of Higher Fullerenes and Buckybowls by the Surface-Catalyzed Cyclodehydrogenation of Aromatic Precursors". In: *Angewandte Chemie International Edition* 49.49 (2010), pp. 9392–9396. ISSN: 1521-3773. DOI: 10.1002/anie.201005000. URL: http://dx.doi.org/10.1002/anie.201005000.

[29] Yuji Okawa and Masakazu Aono. "Materials science: Nanoscale control of chain polymerization". In: *Nature* 409.6821 (Feb. 8, 2001), pp. 683–684. URL: http://dx.doi.org/10.1038/35055625.

[30] Yi-Qi Zhang et al. "Homo-coupling of terminal alkynes on a noble metal surface". In: *Nat Commun* 3 (Dec. 18, 2012), p. 1286. URL: http://dx.doi.org/10.1038/ncomms2291.

[31] Mendel In't Veld et al. "Unique intermolecular reaction of simple porphyrins at a metal surface gives covalent nanostructures". In: *Chem. Commun.* (13 2008), pp. 1536–1538. DOI: 10.1039/B718865J. URL: http://dx.doi.org/10.1039/B718865J.

[32] Sigrid Weigelt et al. "Covalent Interlinking of an Aldehyde and an Amine on a Au(111) Surface in Ultrahigh Vacuum". In: *Angewandte Chemie International Edition* 46.48 (2007), pp. 9227–9230. ISSN: 1521-3773. DOI: 10.1002/anie.200702859. URL: http://dx.doi.org/10.1002/anie.200702859.

[33] Sigrid Weigelt et al. "Molecular Self-Assembly from Building Blocks Synthesized on a Surface in Ultrahigh Vacuum: Kinetic Control and Topo-Chemical Reactions". In: *ACS Nano* 2.4 (2008), pp. 651–660. DOI: 10.1021/nn7004365. eprint: http://pubs.acs.org/doi/pdf/10.1021/nn7004365. URL: http://pubs.acs.org/doi/abs/10.1021/nn7004365.

[34] Matthias Treier, Neville V. Richardson, and Roman Fasel. "Fabrication of Surface-Supported Low-Dimensional Polyimide Networks". In: *Journal of the American Chemical Society* 130.43 (2008), pp. 14054–14055. DOI: 10.1021/ja805342n. eprint: http://pubs.acs.org/doi/pdf/10.1021/ja805342n. URL: http://pubs.acs.org/doi/abs/10.1021/ja805342n.

[35] Matthias Treier et al. "Molecular imaging of polyimide formation". In: *Phys. Chem. Chem. Phys.* 11 (8 2009), pp. 1209–1214. DOI: 10.1039/B815544P. URL: http://dx.doi.org/10.1039/B815544P.

[36] Rémy Pawlak et al. "Supramolecular Assemblies of 1,4-Benzene Diboronic Acid on KCl(001)". In: *The Journal of Physical Chemistry C* 114.20 (2010), pp. 9290–9295. DOI: 10.1021/jp102044u. eprint: http://pubs.acs.org/doi/pdf/10.1021/jp102044u. URL: http://pubs.acs.org/doi/abs/10.1021/jp102044u.

[37] Nikolas A. A. Zwaneveld et al. "Organized Formation of 2D Extended Covalent Organic Frameworks at Surfaces". In: *Journal of the American Chemical Society* 130.21 (2014/01/14 2008), pp. 6678–6679. DOI: 10.1021/ja800906f. URL: http://dx.doi.org/10.1021/ja800906f.

[38] Dingyong Zhong et al. "Linear Alkane Polymerization on a Gold Surface". In: *Science* 334.6053 (2011), pp. 213–216. DOI: 10.1126/science.1211836. eprint: http://www.sciencemag.org/content/334/6053/213.full.pdf. URL: http://www.sciencemag.org/content/334/6053/213.abstract.

[39] Fabian Bebensee et al. "On-Surface Azide–Alkyne Cycloaddition on Cu(111): Does It "Click" in Ultrahigh Vacuum?" In: *Journal of the American Chemical Society* 135.6 (2013), pp. 2136–2139. DOI: 10.1021/ja312303a. eprint: http://pubs.acs.org/doi/pdf/10.1021/ja312303a. URL: http://pubs.acs.org/doi/abs/10.1021/ja312303a.

[40] Qiang Sun et al. "On-Surface Formation of One-Dimensional Polyphenylene through Bergman Cyclization". In: *Journal of the American Chemical Society* 135.23 (2014/01/14 2013), pp. 8448–8451. DOI: 10.1021/ja404039t. URL: http://dx.doi.org/10.1021/ja404039t.

[41] Markus Kittelmann et al. "On-Surface Covalent Linking of Organic Building Blocks on a Bulk Insulator". In: *ACS Nano* 5.10 (2011), pp. 8420–8425. DOI: 10.1021/nn2033192. eprint: http://pubs.acs.org/doi/pdf/10.1021/nn2033192. URL: http://pubs.acs.org/doi/abs/10.1021/nn2033192.

[42] Shelley A. Claridge, Jeffrey J. Schwartz, and Paul S. Weiss. "Electrons, Photons, and Force: Quantitative Single-Molecule Measurements from Physics to Biology". In: *ACS Nano* 5.2 (2011), pp. 693–729. DOI: 10.1021/nn103298x. eprint: http://pubs.acs.org/doi/pdf/10.1021/nn103298x. URL: http://pubs.acs.org/doi/abs/10.1021/nn103298x.

[43] M. A. Reed et al. "Conductance of a Molecular Junction". In: *Science* 278.5336 (1997), pp. 252–254. DOI: 10.1126/science.278.5336.252. eprint: http://www.sciencemag.org/content/278/5336/252.full.pdf. URL: http://www.sciencemag.org/content/278/5336/252.abstract.

[44] Hongkun Park et al. "Nanomechanical oscillations in a single-C60 transistor". In: *Nature* 407.6800 (Sept. 7, 2000), pp. 57–60. URL: http://dx.doi.org/10.1038/35024031.

[45] X. D. Cui et al. "Reproducible Measurement of Single-Molecule Conductivity". In: *Science* 294.5542 (2001), pp. 571–574. DOI: 10.1126/science.1064354. eprint: http://www.sciencemag.org/content/294/5542/571.full.pdf. URL: http://www.sciencemag.org/content/294/5542/571.abstract.

[46] Bingqian Xu and Nongjian J. Tao. "Measurement of Single-Molecule Resistance by Repeated Formation of Molecular Junctions". In: *Science* 301.5637 (2003), pp. 1221–1223. DOI: 10.1126/science.1087481. eprint: http://www.sciencemag.org/content/301/5637/1221.full.pdf. URL: http://www.sciencemag.org/content/301/5637/1221.abstract.

[47] Sung-Yeon Jang et al. "Interpretation of Stochastic Events in Single Molecule Conductance Measurements". In: *Nano Letters* 6.10 (Oct. 2006), pp. 2362–2367.

[48] P Reddy et al. "Thermoelectricity in Molecular Junctions". In: *Science* 315.5818 (Mar. 2007), pp. 1568–1571.

[49] Kanhayalal Baheti et al. "Probing the Chemistry of Molecular Heterojunctions Using Thermoelectricity". In: *Nano Letters* 8.2 (Feb. 2008), pp. 715–719.

[50] Jonathan A Malen et al. "The Nature of Transport Variations in Molecular Heterojunction Electronics". In: *Nano Letters* 9.10 (Oct. 2009), pp. 3406–3412.

[51] Jascha Repp et al. "Controlling the Charge State of Individual Gold Adatoms". In: *Science* 305.5683 (2004), pp. 493–495. DOI: 10.1126/science.1099557. eprint: http://www.sciencemag.org/content/305/5683/493.full.pdf. URL: http://www.sciencemag.org/content/305/5683/493.abstract.

[52] X. H. Qiu, G. V. Nazin, and W. Ho. "Vibronic States in Single Molecule Electron Transport". In: *Phys. Rev. Lett.* 92 (20 May 2004), p. 206102. DOI: 10.1103/PhysRevLett.92.206102. URL: http://link.aps.org/doi/10.1103/PhysRevLett.92.206102.

[53] Jascha Repp et al. "Imaging Bond Formation Between a Gold Atom and Pentacene on an Insulating Surface". In: *Science* 312.5777 (2006), pp. 1196–1199. DOI: 10.1126/science.1126073. eprint: http://www.sciencemag.org/content/312/5777/1196.full.pdf. URL: http://www.sciencemag.org/content/312/5777/1196.abstract.

[54] Xinghua Lu et al. "Charge transfer and screening in individual C60 molecules on metal substrates: A scanning tunneling spectroscopy and theoretical study". In: *Phys. Rev. B* 70 (11 Sept. 2004), p. 115418. DOI: 10.1103/PhysRevB.70.115418. URL: http://link.aps.org/doi/10.1103/PhysRevB.70.115418.

[55] A. Wachowiak et al. "Visualization of the Molecular Jahn-Teller Effect in an Insulating K4C60 Monolayer". In: *Science* 310.5747 (2005), pp. 468–470. DOI: 10.1126/science.1117303. eprint: http://www.sciencemag.org/content/310/5747/468.full.pdf. URL: http://www.sciencemag.org/content/310/5747/468.abstract.

[56] R. Yamachika et al. "Controlled Atomic Doping of a Single C60 Molecule". In: *Science* 304.5668 (2004), pp. 281–284. DOI: 10.1126/science.1095069. eprint: http://www.sciencemag.org/content/304/5668/281.full.pdf. URL: http://www.sciencemag.org/content/304/5668/281.abstract.

[57] C. Joachim and J.K. Gimzewski. "An electromechanical amplifier using a single molecule". In: *Chemical Physics Letters* 265.3–5 (1997), pp. 353–357. ISSN: 0009-2614. DOI: http://dx.doi.org/10.1016/S0009-2614(97)00014-6. URL: http://www.sciencedirect.com/science/article/pii/S0009261497000146.

[58] Sander J. Tans, Alwin R. M. Verschueren, and Cees Dekker. "Room-temperature transistor based on a single carbon nanotube". In: *Nature* 393.6680 (May 7, 1998), pp. 49–52. URL: http://dx.doi.org/10.1038/29954.

[59] R. Martel et al. "Single- and multi-wall carbon nanotube field-effect transistors". In: *Applied Physics Letters* 73.17 (1998), pp. 2447–2449. DOI: http://dx.doi.org/10.1063/1.122477. URL: http://scitation.aip.org/content/aip/journal/apl/73/17/10.1063/1.122477.

[60] J. Hwang et al. "A single-molecule optical transistor". In: *Nature* 460.7251 (July 2, 2009), pp. 76–80. URL: http://dx.doi.org/10.1038/nature08134.

[61] Hyunwook Song et al. "Observation of molecular orbital gating". In: *Nature* 462.7276 (Dec. 24, 2009), pp. 1039–1043. URL: http://dx.doi.org/10.1038/nature08639.

[62] Charles P. Collier et al. "A [2]Catenane-Based Solid State Electronically Reconfigurable Switch". In: *Science* 289.5482 (2000), pp. 1172–1175. DOI: 10.1126/science.289.5482.1172. eprint: http://www.sciencemag.org/content/289/5482/1172.full.pdf. URL: http://www.sciencemag.org/content/289/5482/1172.abstract.

[63] J. S. Foster and J. E. Frommer. "Imaging of liquid crystals using a tunnelling microscope". In: *Nature* 333.6173 (June 9, 1988), pp. 542–545. URL: http://dx.doi.org/10.1038/333542a0.

[64] D. P. E. Smith et al. "Smectic Liquid Crystal Monolayers on Graphite Observed by Scanning Tunneling Microscopy". In: *Science* 245.4913 (1989), pp. 43–45. DOI: 10.1126/science.245.4913.43. eprint: http://www.sciencemag.org/content/245/4913/43.full.pdf. URL: http://www.sciencemag.org/content/245/4913/43.abstract.

[65] Tycho Sleator and Robert Tycko. "Observation of individual organic molecules at a crystal surface with use of a scanning tunneling microscope". In: *Phys. Rev. Lett.* 60 (14 Apr. 1988), pp. 1418–1421. DOI: 10.1103/PhysRevLett.60.1418. URL: http://link.aps.org/doi/10.1103/PhysRevLett.60.1418.

[66] G.A.D. Briggs and Fisher A.J. "STM experiment and atomistic modelling hand in hand: individual molecules on semiconductor surfaces". In: *Surface Science Reports* 33 (May 1999), pp. 1–81.

[67] Peter Grütter, Werner A. Hofer, and Federico Rosei. *Properties of single organic molecules on crystal surfaces*. Imperial College Press, 2006.

[68] Xiaowei Yao et al. "Scanning tunneling microscopy and spectroscopy of individual {C60} molecules on Si(100)-(2 x 1) surfaces". In: *Surface Science* 366.3 (1996), pp. L743–L749. ISSN: 0039-6028. DOI: http://dx.doi.org/10.1016/0039-6028(96)00938-7. URL: http://www.sciencedirect.com/science/article/pii/0039602896009387.

[69] Paul G. Piva et al. "Field regulation of single-molecule conductivity by a charged surface atom". In: *Nature* 435.7042 (June 2, 2005), pp. 658–661. URL: http://dx.doi.org/10.1038/nature03563.

[70] Titash Rakshit et al. "Silicon-based Molecular Electronics". In: *Nano Letters* 4.10 (2004), pp. 1803–1807. DOI: 10.1021/nl049436t. eprint: http://pubs.acs.org/doi/pdf/10.1021/nl049436t. URL: http://pubs.acs.org/doi/abs/10.1021/nl049436t.

[71] Shin-ichi Kamakura et al. "Dispersive Electronic States of the $\pi$-Orbitals Stacking in Single Molecular Lines on the Si(001)-(2x1)-H Surface". In: *The Journal of Physical Chemistry Letters* 4.7 (2013), pp. 1199–1204. DOI: 10.1021/jz400389k. eprint: http://pubs.acs.org/doi/pdf/10.1021/jz400389k. URL: http://pubs.acs.org/doi/abs/10.1021/jz400389k.

[72] Manuel Smeu, Robert A. Wolkow, and Hong Guo. "Conduction Pathway of $\pi$-Stacked Ethylbenzene Molecular Wires on Si(100)". In: *Journal of the American Chemical Society* 131.31 (2009). PMID: 19603787, pp. 11019–11026. DOI: 10.1021/ja902641m. eprint: http://pubs.acs.org/doi/pdf/10.1021/ja902641m. URL: http://pubs.acs.org/doi/abs/10.1021/ja902641m.

[73] Nathan P. Guisinger et al. "Room Temperature Negative Differential Resistance through Individual Organic Molecules on Silicon Surfaces". In: *Nano Letters* 4.1 (2004), pp. 55–59. DOI: 10.1021/nl0348589. eprint: http://pubs.acs.org/doi/pdf/10.1021/nl0348589. URL: http://pubs.acs.org/doi/abs/10.1021/nl0348589.

[74] G. P. Lopinski, D. D. M. Wayner, and R. A. Wolkow. "Self-directed growth of molecular nanostructures on silicon". In: *Nature* 406.6791 (July 6, 2000), pp. 48–51. URL: http://dx.doi.org/10.1038/35017519.

[75] Timothy R. Leftwich and Andrew V. Teplyakov. "Chemical manipulation of multifunctional hydrocarbons on silicon surfaces". In: *Surface Science Reports* 63.1 (2008), pp. 1–71. ISSN: 0167-5729. DOI: http://dx.doi.org/10.1016/j.surfrep.2007.08.001. URL: http://www.sciencedirect.com/science/article/pii/S0167572907000659.

[76] Md. Zakir Hossain, Hiroyuki S. Kato, and Maki Kawai. "Self-Directed Chain Reaction by Small Ketones with the Dangling Bond Site on the Si(100)-(2 x 1)-H Surface: Acetophenone, A Unique Example". In: *Journal of the American Chemical Society* 130.34 (2008), pp. 11518–11523. DOI: 10.1021/ja8033944. eprint: http://pubs.acs.org/doi/pdf/10.1021/ja8033944. URL: http://pubs.acs.org/doi/abs/10.1021/ja8033944.

[77] Xiao Tong, Gino A. DiLabio, and Robert A. Wolkow. "A Self-Directed Growth Process for Creating Covalently Bonded Molecular Assemblies on the H-Si(100)-3x1 Surface". In: *Nano Letters* 4.5 (2004), pp. 979–983. DOI: 10.1021/nl049796g. eprint: http://pubs.acs.org/doi/pdf/10.1021/nl049796g. URL: http://pubs.acs.org/doi/abs/10.1021/nl049796g.

[78] Gino A. DiLabio et al. "Dispersion Interactions Enable the Self-Directed Growth of Linear Alkane Nanostructures Covalently Bound to Silicon". In: *Journal of the American Chemical Society* 126.49 (2004). PMID: 15584738, pp. 16048–16050. DOI: 10.1021/ja0460007. eprint: http://pubs.acs.org/doi/pdf/10.1021/ja0460007. URL: http://pubs.acs.org/doi/abs/10.1021/ja0460007.

[79] T. David et al. "Epitaxial growth of C60 on Ag(110) studied by scanning tunneling microscopy and tunneling spectroscopy". In: *Phys. Rev. B* 50 (8 Aug. 1994), pp. 5810–5813. DOI: 10.1103/PhysRevB.50.5810. URL: http://link.aps.org/doi/10.1103/PhysRevB.50.5810.

[80] M. Grobis, X. Lu, and M. F. Crommie. "Local electronic properties of a molecular monolayer: C60 on Ag(001)". In: *Phys. Rev. B* 66 (16 Oct. 2002), p. 161408. DOI: 10.1103/PhysRevB.66.161408. URL: http://link.aps.org/doi/10.1103/PhysRevB.66.161408.

[81] V. Madhavan et al. "Tunneling into a Single Magnetic Atom: Spectroscopic Evidence of the Kondo Resonance". In: *Science* 280.5363 (1998), pp. 567–569. DOI: 10.1126/science.280.5363.567. eprint: http://www.sciencemag.org/content/280/5363/567.full.pdf. URL: http://www.sciencemag.org/content/280/5363/567.abstract.

[82] R. J. Wilson et al. "Imaging C60 clusters on a surface using a scanning tunnelling microscope". In: *Nature* 348.6302 (Dec. 13, 1990), pp. 621–622. URL: http://dx.doi.org/10.1038/348621a0.

[83] Saw-Wai Hla and Karl-Heinz Rieder. "STM Control of Chemical Reactions: Single-Molecule Synthesis". In: *Annual Review of Physical Chemistry* 54.1 (Oct. 2003), pp. 307–330.

[84] Peter Liljeroth et al. "Single-Molecule Synthesis and Characterization of Metal-Ligand Complexes by Low-Temperature STM". In: *Nano Letters* 10.7 (2010), pp. 2475–2479. DOI: 10.1021/nl100834v. eprint: http://pubs.acs.org/doi/pdf/10.1021/nl100834v. URL: http://pubs.acs.org/doi/abs/10.1021/nl100834v.

[85] T. Jamneala, V. Madhavan, and M. F. Crommie. "Kondo Response of a Single Antiferromagnetic Chromium Trimer". In: *Phys. Rev. Lett.* 87 (25 Nov. 2001), p. 256804. DOI: 10.1103/PhysRevLett.87.256804. URL: http://link.aps.org/doi/10.1103/PhysRevLett.87.256804.

[86] V. Madhavan et al. "Observation of spectral evolution during the formation of a $Ni_2$ Kondo molecule". In: *Phys. Rev. B* 66 (21 Dec. 2002), p. 212411. DOI: 10.1103/PhysRevB.66.212411. URL: http://link.aps.org/doi/10.1103/PhysRevB.66.212411.

[87] V. Madhavan et al. "Local spectroscopy of a Kondo impurity: Co on Au(111)". In: *Phys. Rev. B* 64 (16 Oct. 2001), p. 165412. DOI: 10.1103/PhysRevB.64.165412. URL: http://link.aps.org/doi/10.1103/PhysRevB.64.165412.

[88] I. Fernández-Torrente, K. J. Franke, and J. I. Pascual. "Vibrational Kondo Effect in Pure Organic Charge-Transfer Assemblies". In: *Phys. Rev. Lett.* 101 (21 Nov. 2008), p. 217203. DOI: 10.1103/PhysRevLett.101.217203. URL: http://link.aps.org/doi/10.1103/PhysRevLett.101.217203.

[89] Changgan Zeng et al. "Negative differential-resistance device involving two C60 molecules". In: *Applied Physics Letters* 77.22 (2000), pp. 3595–3597. DOI: http://dx.doi.org/10.1063/1.1328773. URL: http://scitation.aip.org/content/aip/journal/apl/77/22/10.1063/1.1328773.

[90] M. Grobis et al. "Tuning negative differential resistance in a molecular film". In: *Applied Physics Letters* 86.20, 204102 (2005), pages. DOI: http://dx.doi.org/10.1063/1.1931822. URL: http://scitation.aip.org/content/aip/journal/apl/86/20/10.1063/1.1931822.

[91] K Franke et al. "Reducing the Molecule-Substrate Coupling in C60-Based Nanostructures by Molecular Interactions". In: *Physical Review Letters* 100.3 (Jan. 2008), p. 036807.

[92] Daniel Wegner et al. "Single-Molecule Charge Transfer and Bonding at an Organic/Inorganic Interface: Tetracyanoethylene on Noble Metals". In: *Nano Letters* 8.1 (2008), pp. 131–135. DOI: 10.1021/nl072217y. eprint: http://pubs.acs.org/doi/pdf/10.1021/nl072217y. URL: http://pubs.acs.org/doi/abs/10.1021/nl072217y.

[93] I Fernández-Torrente et al. "Long-Range Repulsive Interaction between Molecules on a Metal Surface Induced by Charge Transfer". In: *Physical Review Letters* 99.17 (Oct. 2007), p. 176103.

[94] T R Umbach et al. "Atypical charge redistribution over a charge-transfer monolayer on a metal". In: *New Journal of Physics* 15.8 (Aug. 2013), p. 083048.

[95] Isabel Fernández Torrente, Katharina J Franke, and Jose Ignacio Pascual. "Spectroscopy of C60 single molecules: the role of screening on energy level alignment". In: *Journal of Physics: Condensed Matter* 20.18 (Apr. 2008), p. 184001.

[96] Matthew J. Comstock et al. "Reversible Photomechanical Switching of Individual Engineered Molecules at a Metallic Surface". In: *Phys. Rev. Lett.* 99 (3 July 2007), p. 038301. DOI: 10.1103/PhysRevLett.99.038301. URL: http://link.aps.org/doi/10.1103/PhysRevLett.99.038301.

[97] Sebastian Hagen et al. "Reversible switching of tetra-tert-butyl-azobenzene on a Au(111) surface induced by light and thermal activation". In: *Chemical Physics Letters* 444.1–3 (2007), pp. 85–90. ISSN: 0009-2614. DOI: http://dx.doi.org/10.1016/j.cplett.2007.07.005. URL: http://www.sciencedirect.com/science/article/pii/S0009261407009232.

[98] Ajeet S. Kumar et al. "Reversible Photo-Switching of Single Azobenzene Molecules in Controlled Nanoscale Environments". In: *Nano Letters* 8.6 (2008), pp. 1644–1648. DOI: 10.1021/nl080323+. eprint: http://pubs.acs.org/doi/pdf/10.1021/nl080323%2B. URL: http://pubs.acs.org/doi/abs/10.1021/nl080323+.

[99] László Óvári, Martin Wolf, and Petra Tegeder. "Reversible Changes in the Vibrational Structure of Tetra-tert-butylazobenzene on a Au(111) Surface Induced by Light and Thermal Activation". In: *The Journal of Physical Chemistry C* 111.42 (2007), pp. 15370–15374. DOI: 10.1021/jp075274o. eprint: http://pubs.acs.org/doi/pdf/10.1021/jp075274o. URL: http://pubs.acs.org/doi/abs/10.1021/jp075274o.

[100] Niv Levy et al. "Self-Patterned Molecular Photoswitching in Nanoscale Surface Assemblies". In: *Nano Letters* 9.3 (2009), pp. 935–939. DOI: 10.1021/nl802632g. eprint: http://pubs.acs.org/doi/pdf/10.1021/nl802632g. URL: http://pubs.acs.org/doi/abs/10.1021/nl802632g.

[101] N. Lorente et al. "Symmetry Selection Rules for Vibrationally Inelastic Tunneling". In: *Phys. Rev. Lett.* 86 (12 Mar. 2001), pp. 2593–2596. DOI: 10.1103/PhysRevLett.86.2593. URL: http://link.aps.org/doi/10.1103/PhysRevLett.86.2593.

[102] S Nolen and S.T Ruggiero. "Tunneling spectroscopy of fullerene/Ge multilayer systems". In: *Chemical Physics Letters* 300.5–6 (1999), pp. 656–660. ISSN: 0009-2614. DOI: http://dx.doi.org/10.1016/S0009-2614(98)01442-0. URL: http://www.sciencedirect.com/science/article/pii/S0009261498014420.

[103] J. I. Pascual et al. "Vibrational spectroscopy on single C60 molecules: The role of molecular orientation". In: *The Journal of Chemical Physics* 117.21 (2002), pp. 9531–9534. DOI: http://dx.doi.org/10.1063/1.1524155. URL: http://scitation.aip.org/content/aip/journal/jcp/117/21/10.1063/1.1524155.

[104] M. Grobis et al. "Spatially Dependent Inelastic Tunneling in a Single Metallofullerene". In: *Phys. Rev. Lett.* 94 (13 Apr. 2005), p. 136802. DOI: 10.1103/PhysRevLett.94.136802. URL: http://link.aps.org/doi/10.1103/PhysRevLett.94.136802.

[105] Thomas Frederiksen et al. "Dynamic Jahn-Teller effect in electronic transport through single C60 molecules". In: *Physical Review B* 78.23 (Dec. 2008), p. 233401.

[106] G. V. Nazin, X. H. Qiu, and W. Ho. "Charging and Interaction of Individual Impurities in a Monolayer Organic Crystal". In: *Phys. Rev. Lett.* 95 (16 Oct. 2005), p. 166103. DOI: 10.1103/PhysRevLett.95.166103. URL: http://link.aps.org/doi/10.1103/PhysRevLett.95.166103.

[107] N. A. Pradhan et al. "Atomic Scale Conductance Induced by Single Impurity Charging". In: *Phys. Rev. Lett.* 94 (7 Feb. 2005), p. 076801. DOI: 10.1103/PhysRevLett.94.076801. URL: http://link.aps.org/doi/10.1103/PhysRevLett.94.076801.

[108] I Fernández-Torrente et al. "Gating the Charge State of Single Molecules by Local Electric Fields". In: *Physical Review Letters* 108.3 (Jan. 2012), p. 036801.

[109] J Repp and G Meyer. "Scanning tunneling microscopy of adsorbates on insulating films. From the imaging of individual molecular orbitals to the manipulation of the charge state". In: *Applied Physics A* 85.4 (Sept. 2006), pp. 399–406.

[110] Gerhard Meyer et al. "Scanning Probe Microscopy of Atoms and Molecules on Insulating Films: From Imaging to Molecular Manipulation". In: *CHIMIA International Journal for Chemistry* 66.1 (Feb. 2012), pp. 10–15.

[111] K. Glöckler et al. "Initial growth of insulating overlayers of NaCl on Ge(100) observed by scanning tunneling microscopy with atomic resolution". In: *Phys. Rev. B* 54 (11 Sept. 1996), pp. 7705–7708. DOI: 10.1103/PhysRevB.54.7705. URL: http://link.aps.org/doi/10.1103/PhysRevB.54.7705.

[112] W. Hebenstreit et al. "Atomic resolution by {STM} on ultra-thin films of alkali halides: experiment and local density calculations". In: *Surface Science* 424.2–3 (1999), pp. L321–L328. ISSN: 0039-6028. DOI: http://dx.doi.org/10.1016/S0039-6028(99)00095-3. URL: http://www.sciencedirect.com/science/article/pii/S0039602899000953.

[113] Silvia Schintke et al. "Insulator at the Ultrathin Limit: MgO on Ag(001)". In: *Phys. Rev. Lett.* 87 (27 Dec. 2001), p. 276801. DOI: 10.1103/PhysRevLett.87.276801. URL: http://link.aps.org/doi/10.1103/PhysRevLett.87.276801.

[114] Cyrus F. Hirjibehedin, Christopher P. Lutz, and Andreas J. Heinrich. "Spin Coupling in Engineered Atomic Structures". In: *Science* 312.5776 (2006), pp. 1021–1024. DOI: 10.1126/science.1125398. eprint: http://www.sciencemag.org/content/312/5776/1021.full.pdf. URL: http://www.sciencemag.org/content/312/5776/1021.abstract.

[115] J. Libuda et al. "Structure and defects of an ordered alumina film on NiAl(110)". In: *Surface Science* 318.1–2 (1994), pp. 61–73. ISSN: 0039-6028. DOI: http://dx.doi.org/10.1016/0039-6028(94)90341-7. URL: http://www.sciencedirect.com/science/article/pii/0039602894903417.

[116] Willi Auwärter et al. "Synthesis of One Monolayer of Hexagonal Boron Nitride on Ni(111) from B-Trichloroborazine (ClBNH)3". In: *Chemistry of Materials* 16.2 (2004), pp. 343–345. DOI: 10.1021/cm034805s. eprint: http://pubs.acs.org/doi/pdf/10.1021/cm034805s. URL: http://pubs.acs.org/doi/abs/10.1021/cm034805s.

[117] Jascha Repp et al. "Molecules on Insulating Films: Scanning-Tunneling Microscopy Imaging of Individual Molecular Orbitals". In: *Phys. Rev. Lett.* 94 (2 Jan. 2005), p. 026803. DOI: 10.1103/PhysRevLett.94.026803. URL: http://link.aps.org/doi/10.1103/PhysRevLett.94.026803.

[118] Leo Gross et al. "High-Resolution Molecular Orbital Imaging Using a *p*-Wave STM Tip". In: *Phys. Rev. Lett.* 107 (8 Aug. 2011), p. 086101. DOI: 10.1103/PhysRevLett.107.086101. URL: http://link.aps.org/doi/10.1103/PhysRevLett.107.086101.

[119] L Gross et al. "Measuring the Charge State of an Adatom with Noncontact Atomic Force Microscopy". In: *Science* 324.5933 (June 2009), pp. 1428–1431.

[120] Thomas Leoni et al. "Controlling the Charge State of a Single Redox Molecular Switch". In: *Physical Review Letters* 106.21 (May 2011), p. 216103.

[121] Fabian Mohn et al. "Reversible Bond Formation in a Gold-Atom–Organic-Molecule Complex as a Molecular Switch". In: *Phys. Rev. Lett.* 105 (26 Dec. 2010), p. 266102. DOI: 10.1103/PhysRevLett.105.266102. URL: http://link.aps.org/doi/10.1103/PhysRevLett.105.266102.

[122] P Liljeroth, J Repp, and G Meyer. "Current-Induced Hydrogen Tautomerization and Conductance Switching of Naphthalocyanine Molecules". In: *Science* 317.5842 (Aug. 2007), pp. 1203–1206.

[123] S W Wu et al. "Conductance Hysteresis and Switching in a Single-Molecule Junction". In: *The Journal of Physical Chemistry C* 112.14 (Apr. 2008), pp. 5241–5244.

[124] Toshio Miyamachi et al. "Robust spin crossover and memristance across a single molecule". In: *Nat Commun* 3 (July 3, 2012), p. 938. URL: http://dx.doi.org/10.1038/ncomms1940.

[125] N. Liu, N. A. Pradhan, and W. Ho. "Vibronic states in single molecules: C60 and C70 on ultrathin Al2O3 films". In: *The Journal of Chemical Physics* 120.24 (2004), pp. 11371–11375. DOI: http://dx.doi.org/10.1063/1.1765095. URL: http://scitation.aip.org/content/aip/journal/jcp/120/24/10.1063/1.1765095.

[126] H. J. Lee, J. H. Lee, and W. Ho. "Vibronic Transitions in Single Metalloporphyrins". In: *ChemPhysChem* 6.5 (2005), pp. 971–975. ISSN: 1439-7641. DOI: 10.1002/cphc.200400616. URL: http://dx.doi.org/10.1002/cphc.200400616.

[127] Nilay A Pradhan, Ning Liu, and Wilson Ho. "Vibronic Spectroscopy of Single C60 Molecules and Monolayers with the STM". In: *The Journal of Physical Chemistry B* 109.17 (May 2005), pp. 8513–8518.

[128] N. Ogawa, G. Mikaelian, and W. Ho. "Spatial Variations in Submolecular Vibronic Spectroscopy on a Thin Insulating Film". In: *Phys. Rev. Lett.* 98 (16 Apr. 2007), p. 166103. DOI: 10.1103/PhysRevLett.98.166103. URL: http://link.aps.org/doi/10.1103/PhysRevLett.98.166103.

[129] Q Huan et al. "Spatial imaging of individual vibronic states in the interior of single molecules". In: *The Journal of Chemical Physics* 135.1 (2011), p. 014705.

[130] A. J. Heinrich et al. "Single-Atom Spin-Flip Spectroscopy". In: *Science* 306.5695 (2004), pp. 466–469. DOI: 10.1126/science.1101077. eprint: http://www.sciencemag.org/content/306/5695/466.full.pdf. URL: http://www.sciencemag.org/content/306/5695/466.abstract.

[131] Cyrus F. Hirjibehedin et al. "Large Magnetic Anisotropy of a Single Atomic Spin Embedded in a Surface Molecular Network". In: *Science* 317.5842 (2007), pp. 1199–1203. DOI: 10.1126/science.1146110. eprint: http://www.sciencemag.org/content/317/5842/1199.full.pdf. URL: http://www.sciencemag.org/content/317/5842/1199.abstract.

[132] Sebastian Loth et al. "Measurement of Fast Electron Spin Relaxation Times with Atomic Resolution". In: *Science* 329.5999 (2010), pp. 1628–1630. DOI: 10.1126/science.1191688. eprint: http://www.sciencemag.org/content/329/5999/1628.full.pdf. URL: http://www.sciencemag.org/content/329/5999/1628.abstract.

[133] K. S. Novoselov et al. "Electric Field Effect in Atomically Thin Carbon Films". In: *Science* 306.5696 (2004), pp. 666–669. DOI: 10.1126/science.1102896. eprint: http://www.sciencemag.org/content/306/5696/666.full.pdf. URL: http://www.sciencemag.org/content/306/5696/666.abstract.

[134] K. S. Novoselov et al. "Two-dimensional gas of massless Dirac fermions in graphene". In: *Nature* 438.7065 (Nov. 10, 2005), pp. 197–200. URL: http://dx.doi.org/10.1038/nature04233.

[135] A. K. Geim and K. S. Novoselov. "The rise of graphene". In: *Nat Mater* 6.3 (Mar. 2007), pp. 183–191. URL: http://dx.doi.org/10.1038/nmat1849.

[136] Guo Hong et al. "Recent progress in organic molecule/graphene interfaces". In: *Nano Today* 8.4 (Aug. 2013), pp. 388–402.

[137] Wei Chen et al. "Surface transfer p-type doping of epitaxial graphene." In: *Journal of the American Chemical Society* 129.34 (2007), pp. 10418–10422.

[138] H Pinto et al. "Mechanisms of doping graphene". In: *physica status solidi (a)* 207.9 (Aug. 2010), pp. 2131–2136.

[139] C. Coletti et al. "Charge neutrality and band-gap tuning of epitaxial graphene on SiC by molecular doping". In: *Physical Review B* 81.23 (June 2010), p. 235401. ISSN: 1098-0121. DOI: 10.1103/PhysRevB.81.235401. URL: http://link.aps.org/doi/10.1103/PhysRevB.81.235401.

[140] A. Tadich et al. "Tuning the charge carriers in epitaxial graphene on SiC(0001) from electron to hole via molecular doping with C60F48". In: *Applied Physics Letters* 102.24 (2013), p. 241601. ISSN: 00036951. DOI: 10.1063/1.4811248. URL: http://link.aip.org/link/APPLAB/v102/i24/p241601/s1%5C&Agg=doi.

[141] F Schedin et al. "Detection of individual gas molecules adsorbed on graphene." In: *Nature materials* 6.9 (Sept. 2007), pp. 652–5. ISSN: 1476-1122. DOI: 10.1038/nmat1967. URL: http://www.ncbi.nlm.nih.gov/pubmed/17660825.

[142] Hossein Sojoudi et al. "Creating graphene p-n junctions using self-assembled monolayers." In: *ACS applied materials & interfaces* 4.9 (Sept. 2012), pp. 4781–6. ISSN: 1944-8252. DOI: 10.1021/am301138v. URL: http://www.ncbi.nlm.nih.gov/pubmed/22909428.

[143] Namphung Peimyoo et al. "Photocontrolled Molecular Structural Transition and Doping in Graphene." In: *ACS nano* (Sept. 2012). ISSN: 1936-086X. DOI: 10.1021/nn302876w. URL: http://pubs.acs.org/doi/abs/10.1021/nn302876w.

[144] B Lee et al. "Modification of electronic properties of graphene with self-assembled monolayers." In: *Nano letters* 10.7 (July 2010), pp. 2427–32. ISSN: 1530-6992. DOI: 10.1021/nl100587e. URL: http://www.ncbi.nlm.nih.gov/pubmed/20503977.

[145] Myungwoong Kim et al. "Light-driven reversible modulation of doping in graphene." In: *Nano letters* 12.1 (Jan. 2012), pp. 182–7. ISSN: 1530-6992. DOI: 10.1021/nl2032734. URL: http://www.ncbi.nlm.nih.gov/pubmed/22149166.

[146] Vasilios Georgakilas et al. "Functionalization of graphene: covalent and non-covalent approaches, derivatives and applications." In: *Chemical reviews* 112.11 (Nov. 2012), pp. 6156–214. ISSN: 1520-6890. DOI: 10.1021/cr3000412. URL: http://www.ncbi.nlm.nih.gov/pubmed/23009634.

[147] Zengxing Zhang et al. "Tailoring Electronic Properties of Graphene by $\pi$–$\pi$ Stacking with Aromatic Molecules". In: *The Journal of Physical Chemistry Letters* 2.22 (Nov. 2011), pp. 2897–2905. ISSN: 1948-7185. DOI: 10.1021/jz201273r. URL: http://pubs.acs.org/doi/abs/10.1021/jz201273r.

[148] Peng Wei et al. "Tuning the Dirac point in CVD-grown graphene through solution processed n-type doping with 2-(2-methoxyphenyl)-1,3-dimethyl-2,3-dihydro-1H-benzoimidazole." In: *Nano letters* 13.5 (May 2013), pp. 1890–7. ISSN: 1530-6992. DOI: 10.1021/nl303410g. URL: http://pubs.acs.org/doi/full/10.1021/nl303410g%20http://www.ncbi.nlm.nih.gov/pubmed/23537351.

[149] Xiaomu Wang et al. "Quantitative Analysis of Graphene Doping by Organic Molecular Charge Transfer". In: *The Journal of Physical Chemistry C* 115.15 (Apr. 2011), pp. 7596–7602. ISSN: 1932-7447. DOI: 10.1021/jp200386z. URL: http://pubs.acs.org/doi/abs/10.1021/jp200386z.

[150] Hong Ying Mao et al. "Manipulating the electronic and chemical properties of graphene via molecular functionalization". In: *Progress in Surface Science* 88.2 (May 2013), pp. 132–159. ISSN: 00796816. DOI: 10.1016/j.progsurf.2013.02.001. URL: http://linkinghub.elsevier.com/retrieve/pii/S0079681613000038.

[151] Johannes Jobst et al. "Transport properties of high-quality epitaxial graphene on 6H-SiC(0001)". In: *Solid State Communications* 151.16 (Aug. 2011), pp. 1061–1064. ISSN: 00381098. DOI: 10.1016/j.ssc.2011.05.015. URL: http://linkinghub.elsevier.com/retrieve/pii/S0038109811002493.

[152] Junghun Choi et al. "Chemical Doping of Epitaxial Graphene by Organic Free Radicals". In: *The Journal of Physical Chemistry Letters* 1.2 (Jan. 2010), pp. 505–509. ISSN: 1948-7185. DOI: 10.1021/jz900351w. URL: http://pubs.acs.org/doi/abs/10.1021/jz900351w.

[153] H Yang et al. "STM imaging, spectroscopy and manipulation of a self-assembled PTCDI monolayer on epitaxial graphene." In: *Physical chemistry chemical physics : PCCP* 15.14 (Apr. 2013), pp. 4939–46. ISSN: 1463-9084. DOI: 10.1039/c3cp42591f. URL: http://www.ncbi.nlm.nih.gov/pubmed/23440409.

[154] Kian Ping Loh et al. "The chemistry of graphene". In: *Journal of Materials Chemistry* 20.12 (2010), p. 2277. ISSN: 0959-9428. DOI: 10.1039/b920539j. URL: http://xlink.rsc.org/?DOI=b920539j.

[155] Liang Yan et al. "Chemistry and physics of a single atomic layer: strategies and challenges for functionalization of graphene and graphene-based materials." In: *Chemical Society reviews* 41.1 (Jan. 2012), pp. 97–114. ISSN: 1460-4744. DOI: 10.1039/c1cs15193b. URL: http://www.ncbi.nlm.nih.gov/pubmed/22086617.

[156] Han Huang et al. "Structural and electronic properties of PTCDA thin films on epitaxial graphene." In: *ACS nano* 3.11 (Nov. 2009), pp. 3431–6. ISSN: 1936-086X. DOI: 10.1021/nn9008615. URL: http://www.ncbi.nlm.nih.gov/pubmed/19852489.

[157] Hong Ying Mao et al. "Chemical vapor deposition graphene as structural template to control interfacial molecular orientation of chloroaluminium phthalocyanine". In: *Applied Physics Letters* 99.9 (2011), p. 093301. ISSN: 00036951. DOI: 10.1063/1.3629812. URL: http://link.aip.org/link/APPLAB/v99/i9/p093301/s1%5C&Agg=doi.

[158] S. Zhou et al. "Metal to Insulator Transition in Epitaxial Graphene Induced by Molecular Doping". In: *Physical Review Letters* 101.8 (Aug. 2008), p. 086402. ISSN: 0031-9007. DOI: 10.1103/PhysRevLett.101.086402. URL: http://link.aps.org/doi/10.1103/PhysRevLett.101.086402.

[159] R R Nair et al. "Dual origin of defect magnetism in graphene and its reversible switching by molecular doping." In: *Nature communications* 4.May (Jan. 2013), p. 2010. ISSN: 2041-1723. DOI: 10.1038/ncomms3010. URL: http://www.ncbi.nlm.nih.gov/pubmed/23760522.

[160] Manuela Garnica et al. "Long-range magnetic order in a purely organic 2D layer adsorbed on epitaxial graphene". In: *Nat Phys* 9.6 (June 2013), pp. 368–374. URL: http://dx.doi.org/10.1038/nphys2610.

[161] Xi Ling et al. "Probing the effect of molecular orientation on the intensity of chemical enhancement using graphene-enhanced Raman spectroscopy." In: *Small* 8.9 (May 2012), pp. 1365–72. ISSN: 1613-6829. DOI: 10.1002/smll.201102223. URL: http://www.ncbi.nlm.nih.gov/pubmed/22359411.

[162] Jingquan Liu, Jianguo Tang, and J. Justin Gooding. "Strategies for chemical modification of graphene and applications of chemically modified graphene". In: *Journal of Materials Chemistry* 22.25 (2012), p. 12435. ISSN: 0959-9428. DOI: 10.1039/c2jm31218b. URL: http://xlink.rsc.org/?DOI=c2jm31218b.

[163] Xin Zhao et al. "Nonlinear optical and optical limiting properties of graphene hybrids covalently functionalized by phthalocyanine". In: *Chemical Physics Letters* 577 (July 2013), pp. 62–67. ISSN: 00092614. DOI: 10.1016/j.cplett.2013.04.023. URL: http://linkinghub.elsevier.com/retrieve/pii/S0009261413004909.

[164] Sara Barja et al. "Self-organization of electron acceptor molecules on graphene". In: *Chem. Commun.* 46 (43 2010), pp. 8198–8200. DOI: 10.1039/C0CC02675A. URL: http://dx.doi.org/10.1039/C0CC02675A.

[165] Qing Hua Wang and Mark C Hersam. "Room-temperature molecular-resolution characterization of self-assembled organic monolayers on epitaxial graphene." In: *Nature chemistry* 1.3 (June 2009), pp. 206–11. ISSN: 1755-4349. DOI: 10.1038/nchem.212. URL: http://www.ncbi.nlm.nih.gov/pubmed/21378849.

[166] Md Zakir Hossain, Michael a Walsh, and Mark C Hersam. "Scanning tunneling microscopy, spectroscopy, and nanolithography of epitaxial graphene chemically modified with aryl moieties." In: *Journal of the American Chemical Society* 132.43 (Nov. 2010), pp. 15399–403. ISSN: 1520-5126. DOI: 10.1021/ja107085n. URL: http://www.ncbi.nlm.nih.gov/pubmed/20932052.

[167] Yi-Lin Wang et al. "Selective adsorption and electronic interaction of F16CuPc on epitaxial graphene". In: *Physical Review B* 82.24 (Dec. 2010), p. 245420. ISSN: 1098-0121. DOI: 10.1103/PhysRevB.82.245420. URL: http://link.aps.org/doi/10.1103/PhysRevB.82.245420.

[168] Peter Lauffer et al. "Molecular and electronic structure of PTCDA on bilayer graphene on SiC(0001) studied with scanning tunneling microscopy". In: *Physica Status Solidi (B)* 245.10 (Oct. 2008), pp. 2064–2067. ISSN: 03701972. DOI: 10.1002/pssb.200879615. URL: http://doi.wiley.com/10.1002/pssb.200879615.

[169] Jongweon Cho et al. "Structural and Electronic Decoupling of C60 from Epitaxial Graphene on SiC". In: *Nano Letters* 12.6 (June 2012), pp. 3018–3024.

[170] Päivi Järvinen et al. "Molecular Self-Assembly on Graphene on SiO2 and h-BN Substrates." In: *Nano letters* (June 2013). ISSN: 1530-6992. DOI: 10.1021/nl401265f. URL: http://www.ncbi.nlm.nih.gov/pubmed/23786613.

[171] Franz J. Giessibl. "High-speed force sensor for force microscopy and profilometry utilizing a quartz tuning fork". In: *Applied Physics Letters* 73.26 (1998), pp. 3956–3958. DOI: http://dx.doi.org/10.1063/1.122948. URL: http://scitation.aip.org/content/aip/journal/apl/73/26/10.1063/1.122948.

[172] L Gross et al. "The Chemical Structure of a Molecule Resolved by Atomic Force Microscopy". In: *Science* 325.5944 (Aug. 2009), pp. 1110–1114.

[173] D G de Oteyza et al. "Direct Imaging of Covalent Bond Structure in Single-Molecule Chemical Reactions". In: *Science* 340.6139 (June 2013), pp. 1434–1437. URL: https://www.sciencemag.org/content/340/6139/1434.

[174] Alexander Riss et al. "Local Electronic and Chemical Structure of Oligo-acetylene Derivatives Formed Through Radical Cyclizations at a Surface". In: *Nano Letters* (), null. DOI: 10.1021/nl403791q. eprint: http://pubs.acs.org/doi/pdf/10.1021/nl403791q. URL: http://pubs.acs.org/doi/abs/10.1021/nl403791q.

[175] Alexander Riss et al. "Imaging and Tuning Molecular Levels at the Surface of a Gated Graphene Device". In: *ACS Nano* (), null. DOI: 10.1021/nn501459v. eprint: http://pubs.acs.org/doi/pdf/10.1021/nn501459v. URL: http://pubs.acs.org/doi/abs/10.1021/nn501459v.

[176] Georg Krausch. "Surface induced self assembly in thin polymer films". In: *Materials Science and Engineering: R: Reports* 14.1–2 (1995), pp. v–94. ISSN: 0927-796X. DOI: http://dx.doi.org/10.1016/0927-796X(94)00173-1. URL: http://www.sciencedirect.com/science/article/pii/0927796X94001731.

[177] G. Binnig et al. "Tunneling through a controllable vacuum gap". In: *Applied Physics Letters* 40 (1982), pp. 178–180. DOI: http://dx.doi.org/10.1063/1.92999. URL: http://scitation.aip.org/content/aip/journal/apl/40/2/10.1063/1.92999.

[178] G. Binnig et al. "Surface Studies by Scanning Tunneling Microscopy". In: *Phys. Rev. Lett.* 49 (1 July 1982), pp. 57–61. DOI: 10.1103/PhysRevLett.49.57. URL: http://link.aps.org/doi/10.1103/PhysRevLett.49.57.

[179] G. Binnig et al. "7 x 7 Reconstruction on Si(111) Resolved in Real Space". In: *Phys. Rev. Lett.* 50 (2 Jan. 1983), pp. 120–123. DOI: 10.1103/PhysRevLett.50.120. URL: http://link.aps.org/doi/10.1103/PhysRevLett.50.120.

[180] Sascha Sadewasser and Clemens Barth. "Electrostatic Force Microscopy And Kelvin Probe Force Microscopy". In: *Characterization of Materials*. John Wiley & Sons, Inc., 2002. ISBN: 9780471266969. DOI: 10.1002/0471266965.com152. URL: http://dx.doi.org/10.1002/0471266965.com152.

[181] Sascha Sadewasser and Thilo Glatzel, eds. *Kelvin Probe Force Microscopy*. Springer, 2012.

[182] Thierry Mélin, Mariusz Zdrojek, and David Brunel. "Electrostatic Force Microscopy and Kelvin Force Microscopy as a Probe of the Electrostatic and Electronic Properties of Carbon Nanotubes". In: *Scanning Probe Microscopy in Nanoscience and Nanotechnology*. Ed. by Bharat Bhushan. Springer Berlin Heidelberg, 2010, pp. 89–128. URL: http://dx.doi.org/10.1007/978-3-642-03535-7_4.

[183] J. Bardeen. "Tunnelling from a Many-Particle Point of View". In: *Phys. Rev. Lett.* 6 (2 Jan. 1961), pp. 57–59. DOI: 10.1103/PhysRevLett.6.57. URL: http://link.aps.org/doi/10.1103/PhysRevLett.6.57.

[184] J. Tersoff and D. R. Hamann. "Theory of the scanning tunneling microscope". In: *Phys. Rev. B* 31 (2 Jan. 1985), pp. 805–813. DOI: 10.1103/PhysRevB.31.805. URL: http://link.aps.org/doi/10.1103/PhysRevB.31.805.

[185] C. Julian Chen. *Introduction to Scanning Tunneling Microscopy*. 2nd edition. Oxford University Press, 2008.

[186] Philippe Sautet. "Images of Adsorbates with the Scanning Tunneling Microscope: Theoretical Approaches to the Contrast Mechanism". In: *Chemical Reviews* 97.4 (1997), pp. 1097–1116. DOI: 10.1021/cr9600823. eprint: http://pubs.acs.org/doi/pdf/10.1021/cr9600823. URL: http://pubs.acs.org/doi/abs/10.1021/cr9600823.

[187] William Shockley. "On the Surface States Associated with a Periodic Potential". In: *Phys. Rev.* 56 (4 Aug. 1939), pp. 317–323. DOI: 10.1103/PhysRev.56.317. URL: http://link.aps.org/doi/10.1103/PhysRev.56.317.

[188] W. J. Kaiser and J. A. Stroscio, eds. *Scanning Tunneling Microscopy*. San Diego: Academic Press, Inc., 1993.

[189] W. Chen et al. "Scanning Tunneling Microscopy Observation of an Electronic Superlattice at the Surface of Clean Gold". In: *Phys. Rev. Lett.* 80 (7 Feb. 1998), pp. 1469–1472. DOI: 10.1103/PhysRevLett.80.1469. URL: http://link.aps.org/doi/10.1103/PhysRevLett.80.1469.

[190] P. Mårtensson and R. M. Feenstra. "Geometric and electronic structure of antimony on the GaAs(110) surface studied by scanning tunneling microscopy". In: *Phys. Rev. B* 39 (11 Apr. 1989), pp. 7744–7753. DOI: 10.1103/PhysRevB.39.7744. URL: http://link.aps.org/doi/10.1103/PhysRevB.39.7744.

[191] Franz J. Giessibl et al. "Subatomic Features on the Silicon (111)-(7x7) Surface Observed by Atomic Force Microscopy". In: *Science* 289.5478 (2000), pp. 422–425. DOI: 10.1126/science.289.5478.422. eprint: http://www.sciencemag.org/content/289/5478/422.full.pdf. URL: http://www.sciencemag.org/content/289/5478/422.abstract.

[192] F.J. Giessibl et al. "Imaging of atomic orbitals with the Atomic Force Microscope — experiments and simulations". In: *Annalen der Physik* 10.11-12 (2001), pp. 887–910. ISSN: 1521-3889. DOI: 10.1002/1521-3889(200111)10:11/12<887::AID-ANDP887>3.0.CO;2-B. URL: http://dx.doi.org/10.1002/1521-3889(200111)10:11/12%3C887::AID-ANDP887%3E3.0.CO;2-B.

[193] Franz J Giessibl. "Atomic resolution on Si(111)-(7x7) by noncontact atomic force microscopy with a force sensor based on a quartz tuning fork". In: *Applied Physics Letters* 76.11 (2000), p. 1470.

[194] T. R. Albrecht et al. "Frequency modulation detection using high-Q cantilevers for enhanced force microscope sensitivity". In: *Journal of Applied Physics* 69.2 (1991), pp. 668–673. DOI: http://dx.doi.org/10.1063/1.347347. URL: http://scitation.aip.org/content/aip/journal/jap/69/2/10.1063/1.347347.

[195] U. Dürig, O. Züger, and A. Stalder. "Interaction force detection in scanning probe microscopy: Methods and applications". In: *Journal of Applied Physics* 72.5 (1992), pp. 1778–1798. DOI: http://dx.doi.org/10.1063/1.352348. URL: http://scitation.aip.org/content/aip/journal/jap/72/5/10.1063/1.352348.

[196] G. Binnig, C. F. Quate, and Ch. Gerber. "Atomic Force Microscope". In: *Phys. Rev. Lett.* 56 (9 Mar. 1986), pp. 930–933. DOI: 10.1103/PhysRevLett.56.930. URL: http://link.aps.org/doi/10.1103/PhysRevLett.56.930.

[197] Franz J. Giessibl. "Advances in atomic force microscopy". In: *Rev. Mod. Phys.* 75 (3 July 2003), pp. 949–983. DOI: 10.1103/RevModPhys.75.949. URL: http://link.aps.org/doi/10.1103/RevModPhys.75.949.

[198] Seizo Morita, Franz J. Giessibl, and Roland Wiesendanger, eds. *Noncontact Atomic Force Microscopy*. Vol. 2nd. Springer, 2009.

[199] F. J. Giessibl. "A direct method to calculate tip–sample forces from frequency shifts in frequency-modulation atomic force microscopy". In: *Applied Physics Letters* 78.1 (2001), pp. 123–125. DOI: http://dx.doi.org/10.1063/1.1335546. URL: http://scitation.aip.org/content/aip/journal/apl/78/1/10.1063/1.1335546.

[200] U. Dürig, H. R. Steinauer, and N. Blanc. "Dynamic force microscopy by means of the phase-controlled oscillator method". In: *Journal of Applied Physics* 82.8 (1997), pp. 3641–3651. DOI: http://dx.doi.org/10.1063/1.365726. URL: http://scitation.aip.org/content/aip/journal/jap/82/8/10.1063/1.365726.

[201] L. Bartels, G. Meyer, and K.-H. Rieder. "Controlled vertical manipulation of single CO molecules with the scanning tunneling microscope: A route to chemical contrast". In: *Applied Physics Letters* 71.2 (1997), pp. 213–215. DOI: http://dx.doi.org/10.1063/1.119503. URL: http://scitation.aip.org/content/aip/journal/apl/71/2/10.1063/1.119503.

[202] Nikolaj Moll et al. "A simple model of molecular imaging with noncontact atomic force microscopy". In: *New Journal of Physics* 14.8 (2012), p. 083023. URL: http://stacks.iop.org/1367-2630/14/i=8/a=083023.

[203] Nikolaj Moll et al. "The mechanisms underlying the enhanced resolution of atomic force microscopy with functionalized tips". In: *New Journal of Physics* 12.12 (Dec. 2010), p. 125020.

[204] Naruo Sasaki, Hideaki Aizawa, and Masaru Tsukada. "Theoretical simulation of noncontact {AFM} images of Si(111) $\sqrt{3} \times \sqrt{3}$-Ag surface based on Fourier expansion method". In: *Applied Surface Science* 157.4 (2000), pp. 367–372. ISSN: 0169-4332. DOI: http://dx.doi.org/10.1016/S0169-4332(99)00552-8. URL: http://www.sciencedirect.com/science/article/pii/S0169433299005528.

[205] Naruo Sasaki and Masaru Tsukada. "Theory for the effect of the tip-surface interaction potential on atomic resolution in forced vibration system of noncontact AFM". In: *Applied Surface Science* 140.3–4 (1999), pp. 339–343. ISSN: 0169-4332. DOI: http://dx.doi.org/10.1016/S0169-4332(98)00551-0. URL: http://www.sciencedirect.com/science/article/pii/S0169433298005510.

[206] Werner A. Hofer, Adam S. Foster, and Alexander L. Shluger. "Theories of scanning probe microscopes at the atomic scale". In: *Rev. Mod. Phys.* 75 (4 Oct. 2003), pp. 1287–1331. DOI: 10.1103/RevModPhys.75.1287. URL: http://link.aps.org/doi/10.1103/RevModPhys.75.1287.

[207] N. Atodiresei et al. "Ab initio modeling of noncontact atomic force microscopy imaging of benzene on Cu(110) surface". In: *International Journal of Quantum Chemistry* 108.15 (2008), pp. 2803–2812. ISSN: 1097-461X. DOI: 10.1002/qua.21793. URL: http://dx.doi.org/10.1002/qua.21793.

[208] C. Alan Wright and Santiago D. Solares. "On Mapping Subangstrom Electron Clouds with Force Microscopy". In: *Nano Letters* 11.11 (2011), pp. 5026–5033. DOI: 10.1021/nl2030773. eprint: http://pubs.acs.org/doi/pdf/10.1021/nl2030773. URL: http://pubs.acs.org/doi/abs/10.1021/nl2030773.

[209] Fabien Castanié et al. "Graphite, graphene on SiC, and graphene nanoribbons: Calculated images with a numerical FM-AFM". In: *Beilstein Journal of Nanotechnology* 3 (2012), pp. 301–311. ISSN: 2190-4286. DOI: 10.3762/bjnano.3.34.

[210] Leo Gross et al. "Organic structure determination using atomic-resolution scanning probe microscopy". In: *Nat Chem* 2.10 (Oct. 2010), pp. 821–825. URL: http://dx.doi.org/10.1038/nchem.765.

[211] J. Israelachvili. *Intermolecular and Surface Forces*. Vol. 2nd. Academic, London, 1991.

[212] J. E. Jones. "On the Determination of Molecular Fields. II. From the Equation of State of a Gas". In: *Royal Society of London Proceedings Series A* 106 (Oct. 1924), pp. 463–477. DOI: 10.1098/rspa.1924.0082.

[213] Frank H. Stillinger and Thomas A. Weber. "Computer simulation of local order in condensed phases of silicon". In: *Phys. Rev. B* 31 (8 Apr. 1985), pp. 5262–5271. DOI: 10.1103/PhysRevB.31.5262. URL: http://link.aps.org/doi/10.1103/PhysRevB.31.5262.

[214] W. Pauli. "Über den Zusammenhang des Abschlusses der Elektronengruppen im Atom mit der Komplexstruktur der Spektren". German. In: *Zeitschrift für Physik* 31.1 (1925), pp. 765–783. ISSN: 0044-3328. DOI: 10.1007/BF02980631. URL: http://dx.doi.org/10.1007/BF02980631.

[215] Fabian Mohn et al. "Imaging the charge distribution within a single molecule". In: *Nat Nano* 7.4 (Apr. 2012), pp. 227–231. URL: http://dx.doi.org/10.1038/nnano.2012.20.

[216] Thorsten Wutscher, Alfred J Weymouth, and Franz J Giessibl. "Localization of the phantom force induced by the tunneling current". In: *Physical Review B* 85.19 (May 2012), p. 195426.

[217] Zoya Popovic and Branko D. Popovic. *Introductory Electromagnetics*. Prentice Hall, 1999.

[218] M. F. Crommie, C. P. Lutz, and D. M. Eigler. "Confinement of Electrons to Quantum Corrals on a Metal Surface". In: *Science* 262.5131 (1993), pp. 218–220. DOI: 10.1126/science.262.5131.218. eprint: http://www.sciencemag.org/content/262/5131/218.full.pdf. URL: http://www.sciencemag.org/content/262/5131/218.abstract.

[219] Yuli Xiao and Aiguo Hu. "Bergman Cyclization in Polymer Chemistry and Material Science". In: *Macromolecular Rapid Communications* 32.21 (Aug. 2011), pp. 1688–1698.

[220] Rana K. Mohamed, Paul W. Peterson, and Igor V. Alabugin. "Concerted Reactions That Produce Diradicals and Zwitterions: Electronic, Steric, Conformational, and Kinetic Control of Cycloaromatization Processes". In: *Chemical Reviews* 113.9 (2014/01/14 2013), pp. 7089–7129. DOI: 10.1021/cr4000682. URL: http://dx.doi.org/10.1021/cr4000682.

[221] Gerhard Ertl. "Elementary Steps in Heterogeneous Catalysis". In: *Angewandte Chemie International Edition in English* 29.11 (1990), pp. 1219–1227. ISSN: 1521-3773. DOI: 10.1002/anie.199012191. URL: http://dx.doi.org/10.1002/anie.199012191.

[222] G.A Somorjai. "The surface science of heterogeneous catalysis". In: *Surface Science* 299–300 (1994), pp. 849–866. ISSN: 0039-6028. DOI: http://dx.doi.org/10.1016/0039-6028(94)90702-1. URL: http://www.sciencedirect.com/science/article/pii/0039602894907021.

[223] S. R. Crouch D. A. Skoog; F. J. Holler. *Principles of Instrumental Analysis*. Brooks/Cole, 2006.

[224] R. Wiesendanger. *Scanning Probe Microscopy and Spectroscopy: Methods and Applications*. Cambridge Univ. Press, 1998.

[225] Kine Ø. Hanssen et al. "A Combined Atomic Force Microscopy and Computational Approach for the Structural Elucidation of Breitfussin A and B: Highly Modified Halogenated Dipeptides from Thuiaria breitfussi". In: *Angewandte Chemie International Edition* 51.49 (2012), pp. 12238–12241. ISSN: 1521-3773. DOI: 10.1002/anie.201203960. URL: http://dx.doi.org/10.1002/anie.201203960.

[226] Niko Pavliček et al. "Atomic Force Microscopy Reveals Bistable Configurations of Dibenzo[a,h]thianthrene and their Interconversion Pathway". In: *Physical Review Letters* 108.8 (Feb. 2012), p. 086101.

[227] L Gross et al. "Bond-Order Discrimination by Atomic Force Microscopy". In: *Science* 337.6100 (Sept. 2012), pp. 1326–1329.

[228] Florian Albrecht et al. "Formation and Characterization of a Molecule–Metal–Molecule Bridge in Real Space". In: *Journal of the American Chemical Society* 135.24 (2013), pp. 9200–9203. DOI: 10.1021/ja404084p. eprint: http://pubs.acs.org/doi/pdf/10.1021/ja404084p. URL: http://pubs.acs.org/doi/abs/10.1021/ja404084p.

[229] Jun Zhang et al. "Real-Space Identification of Intermolecular Bonding with Atomic Force Microscopy". In: *Science* 342.6158 (2013), pp. 611–614. DOI: 10.1126/science.1242603. eprint: http://www.sciencemag.org/content/342/6158/611.full.pdf. URL: http://www.sciencemag.org/content/342/6158/611.abstract.

[230] Richard R. Jones and Robert G. Bergman. "p-Benzyne. Generation as an intermediate in a thermal isomerization reaction and trapping evidence for the 1,4-benzenediyl structure". In: *Journal of the American Chemical Society* 94.2 (1972), pp. 660–661. DOI: 10.1021/ja00757a071. eprint: http://pubs.acs.org/doi/pdf/10.1021/ja00757a071. URL: http://pubs.acs.org/doi/abs/10.1021/ja00757a071.

[231] Chandrasekhar Vavilala et al. "Thermal C1-C5 Diradical Cyclization of Enediynes". In: *Journal of the American Chemical Society* 130.41 (2008), pp. 13549–13551. DOI: 10.1021/ja803413f. eprint: http://pubs.acs.org/doi/pdf/10.1021/ja803413f. URL: http://pubs.acs.org/doi/abs/10.1021/ja803413f.

[232] James P. Johnson et al. "Comparison of "Polynaphthalenes" Prepared by Two Mechanistically Distinct Routes". In: *Journal of the American Chemical Society* 125.48 (2003). PMID: 14640637, pp. 14708–14709. DOI: 10.1021/ja035695t. eprint: http://pubs.acs.org/doi/pdf/10.1021/ja035695t. URL: http://pubs.acs.org/doi/abs/10.1021/ja035695t.

[233] J. P. Perdew and Alex Zunger. "Self-interaction correction to density-functional approximations for many-electron systems". In: *Phys. Rev. B* 23 (10 May 1981), pp. 5048–5079. DOI: 10.1103/PhysRevB.23.5048. URL: http://link.aps.org/doi/10.1103/PhysRevB.23.5048.

[234] J. J. Mortensen, L. B. Hansen, and K. W. Jacobsen. "Real-space grid implementation of the projector augmented wave method". In: *Phys. Rev. B* 71 (3 Jan. 2005), p. 035109. DOI: 10.1103/PhysRevB.71.035109. URL: http://link.aps.org/doi/10.1103/PhysRevB.71.035109.

[235] J Enkovaara et al. "Electronic structure calculations with GPAW: a real-space implementation of the projector augmented-wave method". In: *Journal of Physics: Condensed Matter* 22.25 (2010), p. 253202. URL: http://stacks.iop.org/0953-8984/22/i=25/a=253202.

[236] Aidi Zhao et al. "Controlling the Kondo Effect of an Adsorbed Magnetic Ion Through Its Chemical Bonding". In: *Science* 309.5740 (2005), pp. 1542–1544. DOI: 10.1126/science.1113449. eprint: http://www.sciencemag.org/content/309/5740/1542.full.pdf. URL: http://www.sciencemag.org/content/309/5740/1542.abstract.

[237] Matthias Prall, Alexander Wittkopp, and Peter R. Schreiner. "Can Fulvenes Form from Enediynes? A Systematic High-Level Computational Study on Parent and Benzannelated Enediyne and Enyne-Allene Cyclizations". In: *The Journal of Physical Chemistry A* 105.40 (2014/01/14 2001), pp. 9265–9274. DOI: 10.1021/jp0028002. URL: http://dx.doi.org/10.1021/jp0028002.

[238] Kevin D. Lewis and Adam J. Matzger. "Bergman Cyclization of Sterically Hindered Substrates and Observation of Phenyl-Shifted Products". In: *Journal of the American Chemical Society* 127.28 (2014/01/11 2005), pp. 9968–9969. DOI: 10.1021/ja042703c. URL: http://dx.doi.org/10.1021/ja042703c.

[239] Michele A. Brooks and Lawrence T. Scott. "1,2-Shifts of Hydrogen Atoms in Aryl Radicals". In: *Journal of the American Chemical Society* 121.23 (2014/01/11 1999), pp. 5444–5449. DOI: 10.1021/ja984472d. URL: http://dx.doi.org/10.1021/ja984472d.

[240] Matthias Hofmann and Henry F. Schaefer. "Pathways for the Reaction of the Butadiene Radical Cation, [C4H6]*+, with Ethylene". In: *The Journal of Physical Chemistry A* 103.44 (2014/01/11 1999), pp. 8895–8905. DOI: 10.1021/jp9927707. URL: http://dx.doi.org/10.1021/jp9927707.

[241] Chia-Ying Lee and Ming-Jung Wu. "Synthesis of Benzofulvenes by Palladium-Catalyzed Cyclization of 1,2-Dialkynylbenzenes". In: *European Journal of Organic Chemistry* 2007.21 (2007), pp. 3463–3467. ISSN: 1099-0690. DOI: 10.1002/ejoc.200601029. URL: http://dx.doi.org/10.1002/ejoc.200601029.

[242] Igor V. Alabugin and Mariappan Manoharan. "Radical-Anionic Cyclizations of Enediynes: Remarkable Effects of Benzannelation and Remote Substituents on Cyclorearomatization Reactions". In: *Journal of the American Chemical Society* 125.15 (2014/01/11 2003), pp. 4495–4509. DOI: 10.1021/ja029664u. URL: http://dx.doi.org/10.1021/ja029664u.

[243] Igor V. Alabugin and Serguei V. Kovalenko. "C1-C5 Photochemical Cyclization of Enediynes". In: *Journal of the American Chemical Society* 124.31 (2014/01/11 2002), pp. 9052–9053. DOI: 10.1021/ja026630d. URL: http://dx.doi.org/10.1021/ja026630d.

[244] Hideki Shirakawa et al. "Synthesis of electrically conducting organic polymers: halogen derivatives of polyacetylene, (CH)". In: *J. Chem. Soc., Chem. Commun.* (16 1977), pp. 578–580. DOI: 10.1039/C39770000578. URL: http://dx.doi.org/10.1039/C39770000578.

[245] R. H. Friend et al. "Electroluminescence in conjugated polymers". In: *Nature* 397.6715 (Jan. 14, 1999), pp. 121–128. URL: http://dx.doi.org/10.1038/16393.

[246] Veaceslav Coropceanu et al. "Charge Transport in Organic Semiconductors". In: *Chemical Reviews* 107.4 (2014/01/14 2007), pp. 926–952. DOI: 10.1021/cr050140x. URL: http://dx.doi.org/10.1021/cr050140x.

[247] C. J. Brabec, N. S. Sariciftci, and J. C. Hummelen. "Plastic Solar Cells". In: *Advanced Functional Materials* 11.1 (2001), pp. 15–26. ISSN: 1616-3028. DOI: 10.1002/1616-3028(200102)11:1<15::AID-ADFM15>3.0.CO;2-A. URL: http://dx.doi.org/10.1002/1616-3028(200102)11:1%3C15::AID-ADFM15%3E3.0.CO;2-A.

[248] K. Müllen and U. Scherf. *Organic Light Emitting Devices: Synthesis, Properties and Applications*. Wiley-VCH, 2006.

[249] Jana Zaumseil and Henning Sirringhaus. "Electron and Ambipolar Transport in Organic Field-Effect Transistors". In: *Chemical Reviews* 107.4 (2014/01/14 2007), pp. 1296–1323. DOI: 10.1021/cr0501543. URL: http://dx.doi.org/10.1021/cr0501543.

[250] Ludwig Bartels. "Tailoring molecular layers at metal surfaces". In: *Nat Chem* 2.2 (Feb. 2010), pp. 87–95. URL: http://dx.doi.org/10.1038/nchem.517.

[251] Johannes A. A. W. Elemans, Shengbin Lei, and Steven De Feyter. "Molecular and Supramolecular Networks on Surfaces: From Two-Dimensional Crystal Engineering to Reactivity". In: *Angewandte Chemie International Edition* 48.40 (2009), pp. 7298–7332. ISSN: 1521-3773. DOI: 10.1002/anie.200806339. URL: http://dx.doi.org/10.1002/anie.200806339.

[252] Yuji Okawa et al. "Chemical Wiring and Soldering toward All-Molecule Electronic Circuitry". In: *Journal of the American Chemical Society* 133.21 (2014/01/14 2011), pp. 8227–8233. DOI: 10.1021/ja111673x. URL: http://dx.doi.org/10.1021/ja111673x.

[253] Antonio Facchetti. "$\pi$-Conjugated Polymers for Organic Electronics and Photovoltaic Cell Applications". In: *Chemistry of Materials* 23.3 (2014/01/14 2010), pp. 733–758. DOI: 10.1021/cm102419z. URL: http://dx.doi.org/10.1021/cm102419z.

[254] Sanjio S. Zade, Natalia Zamoshchik, and Michael Bendikov. "From Short Conjugated Oligomers to Conjugated Polymers. Lessons from Studies on Long Conjugated Oligomers". In: *Accounts of Chemical Research* 44.1 (2014/01/14 2010), pp. 14–24. DOI: 10.1021/ar1000555. URL: http://dx.doi.org/10.1021/ar1000555.

[255] Jascha Repp, Peter Liljeroth, and Gerhard Meyer. "Coherent electron–nuclear coupling in oligothiophene molecular wires". In: *Nature Physics* 6.12 (Oct. 2010), pp. 975–979.

[256] Olof Wennerstroem. "Qualitative evaluation of the band gap in polymers with extended .pi. systems". In: *Macromolecules* 18.10 (2014/01/14 1985), pp. 1977–1980. DOI: 10.1021/ma00152a029. URL: http://dx.doi.org/10.1021/ma00152a029.

[257] Joost van der Lit et al. "Suppression of electron-vibron coupling in graphene nanoribbons contacted via a single atom". In: *Nat Commun* 4 (June 12, 2013). URL: http://dx.doi.org/10.1038/ncomms3023.

[258] Mark S Hybertsen and Steven G Louie. "First-Principles Theory of Quasiparticles: Calculation of Band Gaps in Semiconductors and Insulators". In: *Physical Review Letters* 55.13 (Sept. 1985), pp. 1418–1421. URL: http://link.aps.org/doi/10.1103/PhysRevLett.55.1418.

[259] Jack Deslippe et al. "BerkeleyGW: A massively parallel computer package for the calculation of the quasiparticle and optical properties of materials and nanostructures". In: *Computer Physics Communications* 183.6 (June 2012), pp. 1269–1289. ISSN: 0010-4655. DOI: http://dx.doi.org/10.1016/j.cpc.2011.12.006. URL: http://www.sciencedirect.com/science/article/pii/S0010465511003912.

[260] S.K.M. Henze et al. "Vertical bonding distances of PTCDA on Au(111) and Ag(111): Relation to the bonding type". In: *Surface Science* 601.6 (2007), pp. 1566–1573. ISSN: 0039-6028. DOI: http://dx.doi.org/10.1016/j.susc.2007.01.020. URL: http://www.sciencedirect.com/science/article/pii/S003960280700043X.

[261] J. B. Neaton, Mark S. Hybertsen, and Steven G. Louie. "Renormalization of Molecular Electronic Levels at Metal-Molecule Interfaces". In: *Phys. Rev. Lett.* 97 (21 Nov. 2006), p. 216405. DOI: 10.1103/PhysRevLett.97.216405. URL: http://link.aps.org/doi/10.1103/PhysRevLett.97.216405.

[262] Zhixiang Sun et al. "Quantitative Atomic Force Microscopy with Carbon Monoxide Terminated Tips". In: *Phys. Rev. Lett.* 106 (4 Jan. 2011), p. 046104. DOI: 10.1103/PhysRevLett.106.046104. URL: http://link.aps.org/doi/10.1103/PhysRevLett.106.046104.

[263] Jian-Hao Chen et al. "Tunable Kondo effect in graphene with defects". In: *Nat Phys* 7.7 (July 2011), pp. 535–538. URL: http://dx.doi.org/10.1038/nphys1962.

[264] Yang Wang et al. "Observing Atomic Collapse Resonances in Artificial Nuclei on Graphene". In: *Science* 340.6133 (2013), pp. 734–737. DOI: 10.1126/science.1234320. eprint: http://www.sciencemag.org/content/340/6133/734.full.pdf. URL: http://www.sciencemag.org/content/340/6133/734.abstract.

[265] Teng Xue et al. "Graphene-supported hemin as a highly active biomimetic oxidation catalyst." In: *Angewandte Chemie (International ed. in English)* 51.16 (Apr. 2012), pp. 3822–5. ISSN: 1521-3773. DOI: 10.1002/anie.201108400. URL: http://www.ncbi.nlm.nih.gov/pubmed/22368046.

[266] Qing Hua Wang et al. "Understanding and controlling the substrate effect on graphene electron-transfer chemistry via reactivity imprint lithography." In: *Nature chemistry* 4.9 (Sept. 2012), pp. 724–32. ISSN: 1755-4349. DOI: 10.1038/nchem.1421. URL: http://www.ncbi.nlm.nih.gov/pubmed/22914193.

[267] Kai Xiao et al. "Surface-induced orientation control of CuPc molecules for the epitaxial growth of highly ordered organic crystals on graphene." In: *Journal of the American Chemical Society* 135.9 (Mar. 2013), pp. 3680–7. ISSN: 1520-5126. DOI: 10.1021/ja3125096. URL: http://www.ncbi.nlm.nih.gov/pubmed/23368998.

[268] Yuanbo Zhang et al. "Giant phonon-induced conductance in scanning tunnelling spectroscopy of gate-tunable graphene". In: *Nature Physics* 4.8 (July 2008), p. 627. ISSN: 1745-2473. DOI: 10.1038/nphys1022. URL: http://www.nature.com/doifinder/10.1038/nphys1022.

[269] Régis Decker et al. "Local Electronic Properties of Graphene on a BN Substrate via Scanning Tunneling Microscopy". In: *Nano Letters* 11.6 (2011), pp. 2291–2295. DOI: 10.1021/nl2005115. eprint: http://pubs.acs.org/doi/pdf/10.1021/nl2005115. URL: http://pubs.acs.org/doi/abs/10.1021/nl2005115.

[270] Xuesong Li et al. "Large-Area Synthesis of High-Quality and Uniform Graphene Films on Copper Foils". In: *Science* 324.5932 (2009), pp. 1312–1314. DOI: 10.1126/science.1171245. eprint: http://www.sciencemag.org/content/324/5932/1312.full.pdf. URL: http://www.sciencemag.org/content/324/5932/1312.abstract.

[271] Katsuyuki Naito, Masatoshi Sakurai, and Syun Egusa. "Molecular Design, Syntheses, and Physical Properties of Nonpolymeric Amorphous Dyes for Electron Transport". In: *The Journal of Physical Chemistry A* 101.12 (Mar. 1997), pp. 2350–2357. ISSN: 1089-5639. DOI: 10.1021/jp963233e. URL: http://dx.doi.org/10.1021/jp963233e.

[272] Thomas L. Andresen et al. "Crystal Structure of Three Compounds Related to Triphenylene and Tetracyanoquinodimethane." In: *Acta Chemica Scandinavica* 53 (1999), pp. 410–416. ISSN: 0904-213X. DOI: 10.3891/acta.chem.scand.53-0410. URL: http://actachemscand.org/doi/10.3891/acta.chem.scand.53-0410.

[273] Stefan Grimme. "Semiempirical GGA-type density functional constructed with a long-range dispersion correction." In: *Journal of computational chemistry* 27.15 (Nov. 2006), pp. 1787–99. ISSN: 0192-8651. DOI: 10.1002/jcc.20495. URL: http://www.ncbi.nlm.nih.gov/pubmed/16955487.

[274] Vincenzo Barone et al. "Role and effective treatment of dispersive forces in materials: Polyethylene and graphite crystals as test cases." In: *Journal of computational chemistry* 30.6 (Apr. 2009), pp. 934–9. ISSN: 1096-987X. DOI: 10.1002/jcc.21112. URL: http://www.ncbi.nlm.nih.gov/pubmed/18785153.

[275] Stefano Baroni et al. "Phonons and related crystal properties from density-functional perturbation theory". In: *Reviews of Modern Physics* 73.2 (July 2001), pp. 515–562. ISSN: 0034-6861. DOI: 10.1103/RevModPhys.73.515. URL: http://link.aps.org/doi/10.1103/RevModPhys.73.515.

[276] Paolo Giannozzi et al. "QUANTUM ESPRESSO: a modular and open-source software project for quantum simulations of materials". In: *Journal of Physics: Condensed Matter* 21.39 (2009), p. 395502. URL: http://stacks.iop.org/0953-8984/21/i=39/a=395502.

[277] Mark S Hybertsen and Steven G Louie. "Electron correlation in semiconductors and insulators: Band gaps and quasiparticle energies". In: *Physical Review B* 34.8 (Oct. 1986), pp. 5390–5413. URL: http://link.aps.org/doi/10.1103/PhysRevB.34.5390.

[278] Victor W. Brar et al. "Observation of Carrier-Density-Dependent Many-Body Effects in Graphene via Tunneling Spectroscopy". In: *Physical Review Letters* 104.3 (Jan. 2010), p. 036805. ISSN: 0031-9007. DOI: 10.1103/PhysRevLett.104.036805. URL: http://link.aps.org/doi/10.1103/PhysRevLett.104.036805.

[279] Niko Pavliček et al. "Symmetry Dependence of Vibration-Assisted Tunneling". In: *Physical Review Letters* 110.13 (Mar. 2013), p. 136101. ISSN: 0031-9007. DOI: 10.1103/PhysRevLett.110.136101. URL: http://link.aps.org/doi/10.1103/PhysRevLett.110.136101.

[280] Shiyong Wang et al. "Vibronic state assisted resonant transport in molecules strongly anchored at an electrode". In: *Physical Review B* 83.11 (Mar. 2011), p. 115431. ISSN: 1098-0121. DOI: 10.1103/PhysRevB.83.115431. URL: http://link.aps.org/doi/10.1103/PhysRevB.83.115431.

[281] F Jäckel et al. "Investigating Molecular Charge Transfer Complexes with a Low Temperature Scanning Tunneling Microscope". In: *Physical Review Letters* 100.12 (Mar. 2008), p. 126102.

[282] Marisa N Faraggi et al. "Bonding and Charge Transfer in Metal–Organic Coordination Networks on Au(111) with Strong Acceptor Molecules". In: *The Journal of Physical Chemistry C* 116.46 (Nov. 2012), pp. 24558–24565.

[283] Gerold M. Rangger et al. "F4TCNQ on Cu, Ag, and Au as prototypical example for a strong organic acceptor on coinage metals". In: *Phys. Rev. B* 79 (16 Apr. 2009), p. 165306. DOI: 10.1103/PhysRevB.79.165306. URL: http://link.aps.org/doi/10.1103/PhysRevB.79.165306.

[284] Zoltán G. Soos and Benjamin J. Topham. "Surface dipole of {F4TCNQ} films: Collective charge transfer and dipole–dipole repulsion in submonolayers". In: *Organic Electronics* 12.1 (2011), pp. 39–44. ISSN: 1566-1199. DOI: http://dx.doi.org/10.1016/j.orgel.2010.09.022. URL: http://www.sciencedirect.com/science/article/pii/S1566119910003289.

[285] Slawomir Braun and William R Salaneck. "Fermi level pinning at interfaces with tetrafluorotetracyanoquinodimethane (F4-TCNQ): The role of integer charge transfer states". In: *Chemical Physics Letters* 438.4-6 (Apr. 2007), pp. 259–262.

[286] Tzu-Chun Tseng et al. "Charge-transfer-induced structural rearrangements at both sides of organic/metal interfaces". In: *Nature Chemistry* 2.5 (Mar. 2010), pp. 374–379.

[287] Tetsuo Katayama et al. "Reactive rearrangements of step atoms by adsorption and asymmetric electronic states of tetrafluoro-tetracyanoquinodimethane on Cu(100)". In: *Phys. Rev. B* 83 (15 Apr. 2011), p. 153403. DOI: 10.1103/PhysRevB.83.153403. URL: http://link.aps.org/doi/10.1103/PhysRevB.83.153403.

[288] Aparna Deshpande et al. "Self-Assembly and Photopolymerization of Sub-2 nm One-Dimensional Organic Nanostructures on Graphene". In: *Journal of the American Chemical Society* 134.40 (Oct. 2012), pp. 16759–16764.

[289] Justice M P Alaboson et al. "Templating Sub-10 nm Atomic Layer Deposited Oxide Nanostructures on Graphene via One-Dimensional Organic Self-Assembled Monolayers". In: *Nano Letters* (Mar. 2013), p. 130311155641002.

[290] A. V. Shytov, M. I. Katsnelson, and L. S. Levitov. "Atomic Collapse and Quasi–Rydberg States in Graphene". In: *Phys. Rev. Lett.* 99 (24 Dec. 2007), p. 246802. DOI: 10.1103/PhysRevLett.99.246802. URL: http://link.aps.org/doi/10.1103/PhysRevLett.99.246802.

[291] Vitor M. Pereira, Johan Nilsson, and A. H. Castro Neto. "Coulomb Impurity Problem in Graphene". In: *Phys. Rev. Lett.* 99 (16 Oct. 2007), p. 166802. DOI: 10.1103/PhysRevLett.99.166802. URL: http://link.aps.org/doi/10.1103/PhysRevLett.99.166802.

[292] Rudro R. Biswas, Subir Sachdev, and Dam T. Son. "Coulomb impurity in graphene". In: *Phys. Rev. B* 76 (20 Nov. 2007), p. 205122. DOI: 10.1103/PhysRevB.76.205122. URL: http://link.aps.org/doi/10.1103/PhysRevB.76.205122.

[293] Yang Wang et al. "Mapping Dirac quasiparticles near a single Coulomb impurity on graphene". In: *Nat Phys* 8.9 (Sept. 2012), pp. 653–657. URL: http://dx.doi.org/10.1038/nphys2379.

[294] Matthias Batzill et al. "Variations of the local electronic surface properties of $TiO_2$(110) induced by intrinsic and extrinsic defects". In: *Phys. Rev. B* 66 (23 Dec. 2002), p. 235401. DOI: 10.1103/PhysRevB.66.235401. URL: http://link.aps.org/doi/10.1103/PhysRevB.66.235401.

[295] R. J. Hamers. "Characterization of localized atomic surface defects by tunneling microscopy and spectroscopy". In: *Journal of Vacuum Science & Technology B* 6.4 (1988), pp. 1462–1467. DOI: http://dx.doi.org/10.1116/1.584241. URL: http://scitation.aip.org/content/avs/journal/jvstb/6/4/10.1116/1.584241.

[296] Victor W Brar et al. "Gate-controlled ionization and screening of cobalt adatoms on a graphene surface". In: *Nature Physics* 7.1 (Oct. 2010), pp. 43–47.

[297] S. W. Wu et al. "Control of Relative Tunneling Rates in Single Molecule Bipolar Electron Transport". In: *Phys. Rev. Lett.* 93 (23 Dec. 2004), p. 236802. DOI: 10.1103/PhysRevLett.93.236802. URL: http://link.aps.org/doi/10.1103/PhysRevLett.93.236802.

[298] Romain Stomp et al. "Detection of Single-Electron Charging in an Individual InAs Quantum Dot by Noncontact Atomic-Force Microscopy". In: *Physical Review Letters* 94.5 (Feb. 2005), p. 056802.

[299] Antoni Tekiel et al. "Room-Temperature Single-Electron Charging Detected by Electrostatic Force Microscopy". In: *ACS Nano* (May 2013), p. 130508082157006.

[300] Lynda Cockins et al. "Energy levels of few-electron quantum dots imaged and characterized by atomic force microscopy". In: *Proceedings of the National Academy of Sciences* (2010). DOI: 10.1073/pnas.0912716107. eprint: http://www.pnas.org/content/early/2010/05/06/0912716107.full.pdf+html. URL: http://www.pnas.org/content/early/2010/05/06/0912716107.abstract.

[301] John E. Sader and Suzanne P. Jarvis. "Accurate formulas for interaction force and energy in frequency modulation force spectroscopy". In: *Applied Physics Letters* 84.10 (2004), pp. 1801–1803. DOI: http://dx.doi.org/10.1063/1.1667267. URL: http://scitation.aip.org/content/aip/journal/apl/84/10/10.1063/1.1667267.

[302] Franz J. Giessibl. "Forces and frequency shifts in atomic-resolution dynamic-force microscopy". In: *Phys. Rev. B* 56 (24 Dec. 1997), pp. 16010–16015. DOI: 10.1103/PhysRevB.56.16010. URL: http://link.aps.org/doi/10.1103/PhysRevB.56.16010.

[303] U. Dürig. "Relations between interaction force and frequency shift in large-amplitude dynamic force microscopy". In: *Applied Physics Letters* 75.3 (1999), pp. 433–435. DOI: http://dx.doi.org/10.1063/1.124399. URL: http://scitation.aip.org/content/aip/journal/apl/75/3/10.1063/1.124399.

[304] H. Hölscher, U.D. Schwarz, and R. Wiesendanger. "Calculation of the frequency shift in dynamic force microscopy". In: *Applied Surface Science* 140.3–4 (1999), pp. 344–351. ISSN: 0169-4332. DOI: http://dx.doi.org/10.1016/S0169-4332(98)00552-2. URL: http://www.sciencedirect.com/science/article/pii/S0169433298005522.

[305] U Dürig. "Interaction sensing in dynamic force microscopy". In: *New Journal of Physics* 2.1 (2000), p. 5. URL: http://stacks.iop.org/1367-2630/2/i=1/a=005.

[306] Joachim Welker, Esther Illek, and Franz J. Giessibl. "Analysis of force-deconvolution methods in frequency-modulation atomic force microscopy". In: *Beilstein Journal of Nanotechnology* 3 (2012), pp. 238–248. ISSN: 2190-4286. DOI: 10.3762/bjnano.3.27.

[307] Zsolt Majzik et al. "Simultaneous current, force and dissipation measurements on the Si(111) 7x7 surface with an optimized qPlus AFM/STM technique". In: *Beilstein Journal of Nanotechnology* 3 (2012), pp. 249–259.

# Appendix A

# Experimental qPlus procedures

## A.1 Amplitude calibration

Having an accurate calibration for the oscillation amplitude is very important for taking precise measurements, especially when extracting a value of the force from the measurement of the frequency shift (e.g. by the Sader-Jarvis method [301] among many other methods [199, 302–306]). The calculation of the force requires precise knowledge of the oscillation amplitude. Additionally, even when not calculating the force, an accurate calibration of the amplitude is necessary for smooth operation in the small amplitude regime.

There are several methods for calibrating the amplitude [193]. For our calibration, we make use of the exponential relationship between tunnel current and tip height, which is modulated by the oscillation, resulting in a modulated tunnel current. For the high oscillation frequencies used in qPlus ($\sim 30\,\mathrm{kHz}$) this current modulation is too fast for the bandwidth of the STM. The STM therefore detects a time average of the modulated tunnel current, but this time average depends on the oscillation amplitude because of the non-linear current vs. $z$ dependence. By measuring the tunnel current as a function of amplitude we can extract an amplitude calibration.

Let us develop an analytical expression for the tunnel current as a function of oscillation amplitude. The tunnel current as a function of tip height (2.2) is given by

$$I(z) \propto \exp(-2\kappa z), \tag{A.1}$$

where $\kappa$ is a constant related to the work function and $z$ is the tip height. If the tip height is modulated around a central height $z_0$ in simple harmonic motion, then the time averaged current $\langle I \rangle_t$ is

$$\langle I \rangle_t = \frac{1}{2\pi} \int_0^{2\pi} I_{eq} \exp(-2\kappa A \sin(\theta)) d\theta, \tag{A.2}$$

where $I_{eq}$ is the current at the equilibrium position, i.e. when the oscillation is off, and $A$ is the amplitude. The solution for this integral is the modified Bessel function of the first

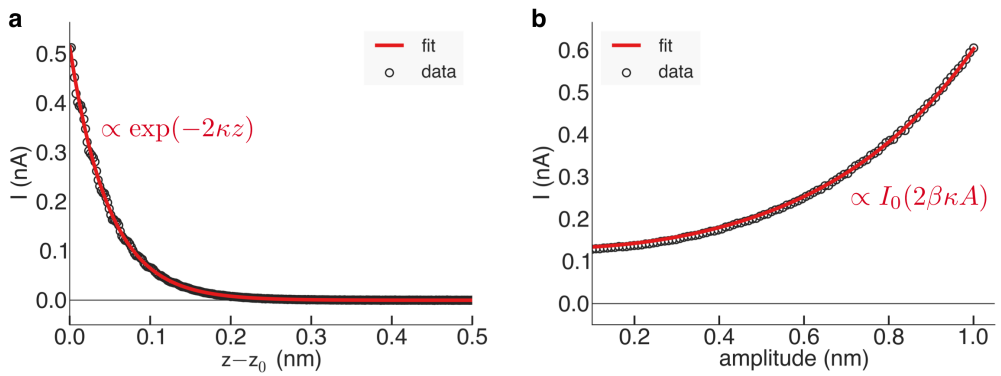


Figure A.1: Amplitude calibration. **(a)** Experimental $I - z$ curve with fit to an exponentially decaying function. The fit yields values for $I_{eq}$ (the current at the equilibrium tip height $z_0$) and the exponential constant $\kappa$. **(b)** Experimental $I - A$ curve and fit to a modified Bessel function of the first kind. Input parameters for the fit are $I_{eq}$ and $\kappa$ taken from (a) and the only new fitting parameter is $\beta$ which yields the amplitude calibration factor.

kind, $I_0(x)$, so we have:

$$\langle I \rangle_t = I_{eq}\, I_0(2\kappa A). \tag{A.3}$$

Our calibration procedure is two-fold. We first take $I - z$ spectroscopy with oscillation off, from which we determine the exponential factor $\kappa$ and the current at our equilibrium position $I_{eq}$. Then we position the tip at the chosen equilibrium tip height and record the tunnel current as a function of amplitude. We then fit this function with $I_{eq}\, I_0(2\beta\kappa A)$, where $\beta$ is the only fitting parameter. This $\beta$ yields the factor by which we need to change our previous amplitude calibration to achieve a correct measure of the amplitude. An example of this fitting procedure is given in Fig. A.1. For better accuracy one could take slew-rate and bandwidth limitations of the STM amplification into account [197].

## A.2 qPlus electronics and operational details

The electronic signals coming from the qPlus sensor are tunnel current and piezo current (due to deflection of the cantilever). In the standard design in our instrument (second generation qPlus [198]), the tunnel current is measured from one of the qPlus electrodes and the deflection signal is measured from the other one. The two electrodes, however, are connected through a parasitic capacitance [307]. This, due to the creation of a virtual ground by the STM preamp, can lead to cross-talk between current and $\Delta f$ signals. This can have the effect of creating similar signals in both current and $\Delta f$ (especially for high currents) and problems with $\Delta f$ feedback [307]. Therefore, to solve this problem the qPlus and STM preamp need to be better insulated from each other.

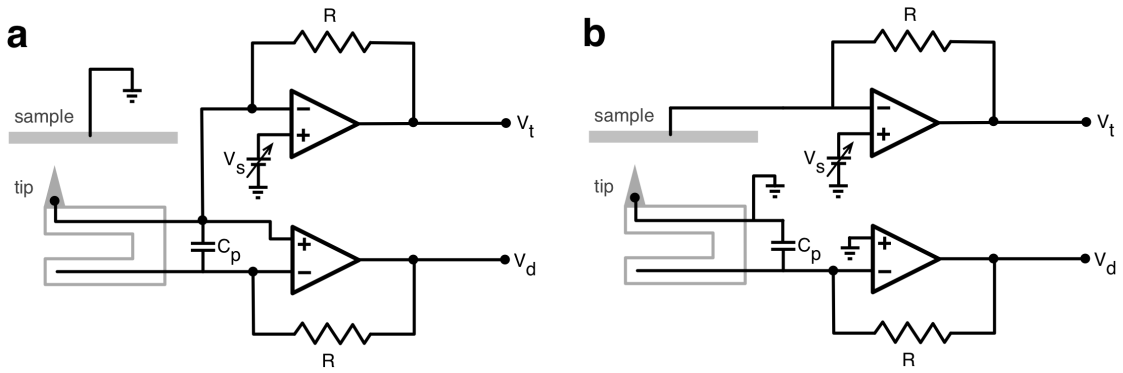


Figure A.2: Comparison of two amplifier circuits. **(a)** Measuring tunnel current from the tip. In this setup one of the two electrodes on the qPlus sensor collects the current from the sample, which is amplified by the STM $I-V$ converter (top). At the same time the deflection signal from the other electrode is measured by the deflection $I-V$ converter (bottom). The electrodes are coupled by a parasitic capacitance $C_p$, which can generate cross-talk between the measurement signals. This is due to the STM amplifiers generally having smaller bandwidth than necessary to keep the virtual ground on their input constant, which generates current through $C_p$ on the input of the detection amplifier [307]. **(b)** Measuring tunnel current from the sample. The tunnel current $I-V$ converter is connected to the sample, while the electrode to the tip is grounded. This ensures a constant voltage at this electrode and avoids spurious signals on the input of the detection $I-V$ converter. This is the setup we use for AFM operation.

There are two main solutions to this: measuring the tunnel current from the sample side or isolate the tip from the qPlus electrodes. We implemented the first solution by connecting the STM preamp to the sample side and grounding the connection to the tip, which usually measures the tunnel current (Fig. A.2). To enable this we needed to install a coaxial cable at the sample. The second method would be to change the sensor design in order to isolate the tip and connect a separate wire leading from the tip to the STM preamp. A possible disadvantage of this method could be that the extra wire causes new resonances in the oscillation and reduce the Q-value.

qPlus operation requires two feedback loops, one for amplitude and one for phase. The amplitude feedback controls the oscillation amplitude by adjusting the excitation of the shaker piezo. Normal operation of qPlus is in constant amplitude mode with a typical amplitude set point of $50\,\mathrm{pm} \leq A \leq 100\,\mathrm{pm}$. The phase feedback (using a PLL) controls the phase for on-resonance excitation [197] by changing the excitation frequency. This, in effect, measures the frequency shift (the measurement signal from the qPlus) as the difference between the new excitation frequency and the original resonance frequency. This original resonance frequency represents the natural frequency of the sensor without interaction from the surface, so it should be be set to the frequency when the sensor is withdrawn far from the surface (a number of coarse steps) until the frequency doesn't change with distance and there is no longer an influence of the sample bias on the frequency.

The following points are necessary to achieve high-quality images with sub-molecular resolution using qPlus:

1. Understanding of the natural frequency and Q-factor of the sensor (see above)
2. A low bandwidth for the PLL ($10\,\mathrm{Hz} - 20\,\mathrm{Hz}$)
3. Low piezo drift, compensated by drift correction, if necessary
4. Small tip oscillation amplitudes ($50\,\mathrm{pm} - 300\,\mathrm{pm}$)
5. Slow scan speeds ($\sim 0.3\,\mathrm{s\,pixel^{-1}}$, i.e. several times the inverse bandwidth)
6. Constant height imaging
7. CO-modified tip